THE EFFECT OF PREDICTED CLIMATE CHANGE ON WESTERN AUSTRALIAN REGIONAL OCEANOGRAPHY

by

Paul J. Durack

A thesis submitted in fulfilment of the
requirements for the degree of B.Sc.(Hons)
in the School of Environmental Science
Murdoch University

November 2002

I declare that this thesis is my own account of research, unless otherwise stated. It contains as its main content, work which has not been previously submitted for a degree at any tertiary institution.

Paul J. Durack

ABSTRACT

The CSIRO Mark 3 coupled Atmosphere-Ocean Global Climate Model was analysed to determine changes to the regional oceanography of Western Australia, attributable to anthropogenic climate change under the (IPCC) A2 (greenhouse gas worst-case) scenario.

Changes to atmospheric and oceanographic circulation indicate a significant increase in heat content of the ocean, decreased salinity and increased atmosphere-ocean fluxes linked to global atmospheric heat content.

These changes agree with the findings of the IPCC resolving changes to terrestrial temperature and precipitation patterns, with mean global surface temperatures predicted to increase 1.4 - 5.8^oC by 2100.

The 5 key regional currents, Leeuwin Current, West Australian Current, Indian Ocean Central Water intrusion, Leeuwin Undercurrent and the South Equatorial Current, are resolved by this model, which indicates significant changes to the oceanography of the region.

Inferred from the regional dataset, and in accordance with recent work on the topic, possible changing global ocean circulation is indicated by the model. This is expressed through the reproduction of the Indonesian throughflow, the only equatorial link between the 3 major global oceans. The model predicts a decrease to transport of this flow, inferring change to the global thermohaline circulation.

Changing patterns have been acknowledged, due to CO_2 forced high-latitude freshening, leading to decreased salinity values. These, when coupled to increased heat content, lead to a more stratified ocean, reducing the density gradient driving the geostrophic thermohaline circulation.

Increased atmospheric temperature corresponds with greater fluxes into the ocean. These lead to a marked increase in heat content of the 'surface' (top ~500 m), also linked to a more stratified global ocean, reducing the density gradient driving thermohaline circulation. Advection of heat through the Indonesian throughflow, was not a significant cause of increased heat content

for regional oceanography.

The dominance of Indian Ocean Central Water, a feature not previously acknowledged, appears responsible for a considerable increase in salinity values. Model output also indicates heat transport increases due to this source, suggesting this feature may be responsible for a considerable proportion of change in the region.

Changes to the currents replicate the patterns expressed in the temperature and salinity profiles for the regional ocean. These indicate decreased transport for the Indonesian throughflow and South Equatorial Currents. This flow too is the feeder flow driving the Leeuwin Current. Geopotential anomaly indicates a marginal increase in this gradient, supporting the concept of a more pronounced Leeuwin flow.

ACKNOWLEDGEMENTS

I would like to acknowledge the support of many people who assisted me during this study - providing both a great deal of background assistance with research and encouragement during the extent of the project.

I would firstly like to thank Prof. Tom Lyons for hours of often tedious conversations about the oceans, atmosphere (in that order!) and Matlab, and for putting up with my constant queries. He has provided an incredible insight into the world of modelling and science in general - thanks so much for your continued assistance!

I would also like to thank Prof. Chari Pattiaratchi for assisting me with oceanographic understanding and also for providing some routines for data visualisation within Matlab. Chari has provided me with a wide source of oceanographic information and ensured that my visualisations and outputs adhere to current scientific conventions.

I would like to thank Tony Hirst (Division of Atmospheric Research [DAR] - CSIRO) for providing the model output utilised within this study; without this data, the present study would not have been undertaken. I would also like to thank Tony for answering all of my early (and late!) questions in relation to the CSIRO Mark 3 model and its intricacies, as well as background information on the conventions and methods of data organisation for this model.

I would also like to acknowledge the use of some Matlab packages that assisted with visualisation and calculation of the figures. Firstly Chuck Denhams - Netcdf toolbox, a collection of routines that allows Matlab to read the Netcdf file format. Phil Morgan for his Seawater package (CSIRO), enabling the user to compute seawater properties from raw data - and assisted me in calculating density, geopotential anomaly and specific heat

values for this study. I would also like to acknowledge the use of Rich Pawlowicz's M_map toolbox. This toolbox enables the user to plot images using fine-grid coastline databases, and also allows easy conversion of latitude-longitude coordinates into meaningful Earth surface distance values.

I would like to thank the following people for their assistance obtaining article reprints, images and for providing opinions, guidance and background information about the topic. In no particular order: Dr Ian Smith, Dr Wenju Cai, Assoc Prof. Ian Simmonds, Dr Mark Lukas, Dr David Stephens, Dr John McGregor, Prof. Ian James, Dr Ross Taplin, Dr Ashok Luhar, Prof. Friedrich Schott, Alan Pearce, Prof. Matthias Tomczak, Prof. Geof Lennon, Dr Greg Laughlin, Dr Swadhin Behera, Dr Warren White, Prof. Wallace Broecker, Dr Peter McIntosh, Dr Steven Charles, Dr Bryson Bates, Dr Bill Kessler, Dr J. Stuart Godfrey, Dr Barrie Hunt, Dr Andreas Schiller, Dr Gary Meyers, Dr Tara Ansell, Jenny Smith, Dr Lynnath Beckley, Dr Ray Steedman, Dr Phil O'Brien, Dr Peter Harris and Curtis Covey.

I would like to thank the guys down the hall - Dave, Shano, Henkles and Spanna for providing an abundant source of entertainment, making some of the longer and more tedious days seem easier, and specifically the 'lunch-club' for providing a constant source of entertainment on a day to day basis! I would also like to thank Meeks, Shano, Cris, Weeza and Chooks for giving me lifts to and from uni, saving me hours of travel time over the year.

I would also like to thank the divisional staff (especially the computing guys - thanks Rod and Ken!) for answering any and all of my questions with lightning speed and incredible accuracy and for assisting me with any simple or complex problems that I faced throughout the year.

Last but not least I would like to thank my family for supporting me through this

year and making the time to listen to me whatever the time of day or night.

Thanks to all who assisted me with this study - I apologise if I have missed anyone!

TABLE OF CONTENTS

Page

LIST OF TABLES x

LIST OF FIGURES xii

CHAPTER

1 INTRODUCTION 1

2 WESTERN AUSTRALIAN REGIONAL OCEANOGRAPHY 4

2.1 Introduction 4
2.2 Climate - Atmosphere and Oceans 6
2.2.1 Western Australian Atmospheric characteristics 6
2.2.2 Western Australian Ocean characteristics 8
2.3 Forcing mechanisms for regional oceanography 11
2.3.1 The Indian Ocean - Sub-tropical Gyre 11
2.3.2 The Indonesian Throughflow 13
2.3.3 The South Equatorial Current 14
2.3.4 The Antarctic Circumpolar Current 15
2.3.5 Deep Ocean Circulation 16
2.4 Summary of Regional Currents 16
2.4.1 The West Australian Current 17
2.4.2 Indian Ocean Central Water - Geostrophic Current 19
2.4.3 The Leeuwin Current 19
2.4.4 The Leeuwin Undercurrent 22
2.4.5 Inner-shelf Currents 23
2.5 Climatological Factors 29
2.5.1 El Niño and the Southern Oscillation Index 29
2.5.2 The Indian Ocean Dipole 33
2.5.3 Madden-Julian Oscillation 34
2.6 Global Climate Modelling 35
2.6.1 Greenhouse Gases 36
2.6.2 CSIRO - Global Climate Models 37

3 METHODOLOGY 41

3.1 Output Variables 41
3.1.1 Scalar Quantities 42
3.1.2 Vectoral Quantities 42
3.2 Assumptions 42
3.2.1 Temperature 43
3.2.2 Density 44
3.2.3 Geopotential Anomaly 44

3.2.4 Transports . . . 45
3.3 Data . . . 48
3.3.1 Currents . . . 49
3.3.2 Temperature . . . 51
3.3.3 Salinity . . . 56
3.3.4 Density . . . 58
3.3.5 Geopotential Anomaly . . . 60
3.4 Regional replication . . . 62

4 RESULTS . . . 65

4.1 Atmospheric Circulation . . . 65
4.1.1 Regional Circulation Patterns . . . 65
4.1.2 Windstress . . . 69
4.2 Ocean Circulation . . . 76
4.2.1 Sea Surface (and subsurface) Temperature . . . 76
4.2.2 Salinity . . . 82
4.2.3 Density . . . 88
4.2.4 Geopotential Anomaly . . . 92
4.2.5 Currents . . . 93
4.2.6 Volume Transports . . . 99
4.2.7 Surface Fluxes . . . 102

5 DISCUSSION . . . 111

5.1 Caveat . . . 112
5.2 Key variables reflecting changing patterns to climate . . . 113
5.2.1 Temperature . . . 113
5.2.2 Salinity . . . 115
5.2.3 Density . . . 116
5.2.4 Geopotential Anomaly . . . 117
5.3 Changes to ocean circulation affecting current and heat-transport systems 118
5.3.1 Currents . . . 118
5.3.2 Transports . . . 119
5.3.3 Heat Transport . . . 120
5.3.4 The Leeuwin Current . . . 121
5.3.5 IOCW . . . 122
5.3.6 Inner-shelf Currents . . . 123
5.4 Modelled change to oceanography - effects to climate for Western Australia . . . 123
5.4.1 Climate . . . 123
5.5 Model Agreement . . . 127
5.5.1 Levitus Dataset . . . 127
5.6 Synergy . . . 128

6 CONCLUSION . . . 130

6.1 Research gaps . . . 130
6.2 Future Studies . . . 131

A ACRONYMS AND CONVENTIONS 134

B CAPES CURRENT EXTENSION STUDY 137

REFERENCES 140

LIST OF TABLES

Table Page

2.1 Southern Oscillation Index - Calculated values from 1951 - 2002 *(from Bureau of Meteorology, 2002)* and corresponding Authors 32

4.1 Modelled MSLP values and locations for each of the datasets (All values represent hPa) 66

4.2 Modelled windstress values and locations for each of the datasets taken along 99^oE (All values represent $dyne\ cm^{-2}$) 72

4.3 Equilibrium times for key climate subsystems *(from McGuffie and Henderson-Sellers, 1999)* 77

4.4 Modelled temperature values for each of the datasets relating to the top ∼285 m (All values represent ^oC) 80

4.5 Modelled heat transport inputs for each of the datasets relating to the IT (top ∼400 m) and IOCW (top ∼160 m) (All values represent PW) 80

4.6 Modelled changes to temperature for each of the datasets relating to the top ∼285 m (All values represent ^oC) 82

4.7 Modelled salinity values for each of the datasets relating to the top ∼285 m (All values represent ppt) 85

4.8 Modelled changes to salinity for each of the datasets relating to the top ∼285 m (All values represent ppt) 85

4.9 Modelled density values for each of the datasets relating to the top ∼285 m (All values represent σ_Θ) 92

4.10 Modelled changes to density for each of the datasets relating to the top ∼285 m (All values represent σ_Θ) 92

4.11 Modelled current transports for each of the datasets 101

4.12 Modelled surface heat flux for each of the datasets (All values represent $W\ m^{-2}$) 105

4.13 Modelled changes to surface heat flux for each of the datasets (All values represent $W\ m^{-2}$) 105

4.14 Modelled surface freshwater flux for each of the datasets (All values represent $mm\ day^{-1}$) 109

4.15 Modelled changes to surface freshwater flux for each of the datasets (All values represent $mm\ day^{-1}$) 109

LIST OF FIGURES

Figure Page

2.1 Regional map of the study area *(From Laughlin, 1997)* 10

2.2 Indian Ocean winter circulation *(from Schott and McCreary, 2001)* 12

2.3 Indian Ocean summer circulation *(from Schott and McCreary, 2001)* 12

2.4 Leeuwin Current and Capes Current flows represented *(WASTAC image)* . . . 27

3.1 Vectoral grid with transport locations annotated. Current acronyms are included in Appendix A 47

3.2 Schematic diagram of regional Western Australian oceanography. 50

3.3 Modelled 10-yr mean currents for A2000 at 15 m depth (Scale arrows represent 10 cm s^{-1}) 52

3.4 Modelled 10-yr mean currents for A2000 at 60 m depth 52

3.5 Modelled 10-yr mean currents for A2000 at 406 m depth 53

3.6 Modelled 10-yr mean temperature for A2000 at 5 m depth 54

3.7 Observed mean surface temperature *(from Levitus94 Annual, 2002)* 55

3.8 Modelled 10-yr mean temperature profile along 113^oE for A2000 55

3.9 Observed mean temperature profile along 113^oE *(from Levitus94 Annual, 2002)* 55

3.10 Modelled 10-yr mean salinity for A2000 at 5 m depth 58

3.11 Observed mean surface salinity *(from Levitus94 Annual, 2002)* 59

3.12 Modelled 10-yr mean salinity profile along 113^oE for A2000 59

3.13 Observed mean salinity profile along 113^oE *(from Levitus94 Annual, 2002)* . . 59

3.14 Modelled 10-yr mean density for A2000 at 5 m depth 60

3.15 Observed mean surface density *(from Levitus94 Annual, 2002)* 61

3.16 Modelled 10-yr mean density profile along 113^oE for A2000 61

3.17 Observed mean density profile along 113^oE *(from Levitus94 Annual, 2002)* . . 61

3.18 Modelled 10-yr mean geopotential anomaly for A2000 at 285 m reference depth 63

3.19 Observed mean geopotential anomaly at 300 m reference depth *(from Levitus94 Annual, 2002)* 63

4.1 Modelled 10-yr mean MSLP for A2000 67

4.2 Modelled 10-yr mean MSLP for A2070 67

4.3 Modelled 10-yr mean MSLP change for A2070 compared to A2000 68

4.4 Modelled 10-yr mean MSLP change for A2100 compared to A2000 68

4.5 Modelled 10-yr mean MSLP for C2000 70

4.6 Modelled 10-yr mean MSLP for C2070 70

4.7 Modelled 10-yr mean MSLP for C2070 compared to C2000 71

4.8 Modelled 10-yr mean MSLP for C2100 compared to C2000 71

4.9 Modelled 10-yr mean wind stress for A2000 (Scale arrows represent 0.5 $dyne\ cm^{-2}$) 73

4.10 Modelled 10-yr mean wind stress for A2070 74

4.11 Modelled 10-yr mean wind stress for A2100 compared to A2000 75

4.12 Modelled 10-yr mean SST change for A2070 compared to A2000 78

4.13 Modelled 10-yr mean SST change for A2100 compared to A2000 78

4.14 Modelled 10-yr mean temperature change for A2070 compared to A2000 along 113^oS 79

4.15 Modelled 10-yr mean temperature change for A2100 compared to A2000 along 113^oS 79

4.16 Modelled 10-yr mean temperature change for A2100 compared to A2000 along 113^oS 80

4.17 Modelled 10-yr mean SST change for C2070 compared to C2000 83

4.18 Modelled 10-yr mean temperature change for C2070 compared to C2000 along 113^oS 83

4.19 Modelled 10-yr mean surface salinity change for A2070 compared to A2000 . . 86

4.20 Modelled 10-yr mean salinity change for A2070 compared to A2000 along 113^oS 87

4.21 Modelled 10-yr mean salinity change for A2100 compared to A2000 along 113^oS 87

4.22 Modelled 10-yr mean salinity change for C2070 compared to C2000 88

4.23 Modelled 10-yr mean salinity change for A2070 compared to A2000 along 113^oS 89

4.24 Modelled 10-yr mean surface density change for A2100 compared to A2000 . . 90

4.25 Modelled 10-yr mean density change for A2070 compared to A2000 along 113^oS 91

4.26 Modelled 10-yr mean density change for A2100 compared to A2000 along 113^oS 91

4.27 Modelled 10-yr mean SST change for A2100 compared to A2000 93

4.28 Modelled 10-yr mean geopotential anomaly for A2000 for reference depth 285 m 94

4.29 Modelled 10-yr mean geopotential anomaly for A2100 for reference depth 285 m 94

4.30 Modelled 10-yr mean surface currents change for A2100 compared to A2000 . 96

4.31 Modelled 10-yr mean currents change for A2100 compared to A2000 at 60 m depth 97

4.32 Modelled 10-yr mean currents change for A2100 compared to A2000 at 406 m depth 98

4.33 Modelled 10-yr mean surface currents change for C2070 compared to C2000 . 99

4.34 Modelled 10-yr mean transport for A2000 101

4.35 Modelled 10-yr mean surface heat flux for A2000 (All values represent $W\ m^{-2}$) 103

4.36 Modelled 10-yr mean surface heat flux change for A2070 compared to A2000 (All values represent $W\ m^{-2}$) 104

4.37 Modelled 10-yr mean surface heat flux change for A2100 compared to A2000 (All values represent $W\ m^{-2}$) 105

4.38 Modelled 10-yr mean surface heat flux change for C2070 compared to C2000 (All values represent $W\ m^{-2}$) 106

4.39 Modelled 10-yr mean freshwater flux for A2000 (Values indicate $mm\ day^{-1}$) . 107

4.40 Modelled 10-yr mean freshwater flux change for A2070 compared to A2000 (Values indicate $mm\ day^{-1}$) 108

4.41 Modelled 10-yr mean freshwater flux change for A2100 compared to A2000 (Values indicate $mm\ day^{-1}$) 108

4.42 Modelled 10-yr mean surface freshwater flux change for C2070 compared to C2000 (Values indicate $mm\ day^{-1}$) 110

5.1 Zonal sum of the number of observations in the Levitus Database 1941 - 1998 *(From Banks and Wood, 2002)* 128

B.1 Cruise track for RV Franklin 1/96 (11 - 28/12/1996) 138

B.2 Cruise track for RV Franklin 4/96 (22 - 29/3/1996) 139

CHAPTER 1
INTRODUCTION

A knowledge of the role played by the oceans in balancing the global heat budget is fundamental to an understanding of climate and its evolution. Many studies have uncovered the role of the Indonesian throughflow ([IT] and the continuation of this flow to form the South Equatorial Current [SEC]) in both heat and salt transfer from the North Pacific Ocean into the Indian Ocean. This transfer is one of the global choke-points in the thermohaline cirulation (THC), the only equatorial link allowing transfer of high-energy tropical water (Broecker, 1991; Gordon, 1986). The THC distribution of heat (energy) around the earth, moderates daily, seasonal and interannual temperature fluctuations, leading the seasonal patterns (Clark *et al.*, 2002). This system, while governing global circulation, also dominates Western Australian Regional Oceanography, feeding the anomalous Leeuwin Current (LC) flow and being responsible for the major meridional heat transport across the Indian Ocean basin.

The intrinsically coupled nature of the ocean and the atmosphere is undisputed; however, the complex processes driving these systems (both separately and in their coupled form) are one of the greatest areas of confusion in the climate sciences. It is the interaction of these systems (collectively termed climate) that needs to be better understood. Developing a thorough understanding of the global climatic system will improve predictive models, allowing for resolution of anthropogenic and cyclical changes to climate.

The topic of climate change has developed into one of the 21st century's most significant scientific questions. How have anthropogenic changes to the Earth effected the way climate operates? How has humanity altered the atmosphere and the environment to lead

to changes in climate globally?

The ocean dominates climate through its high heat capacity, a sink for global energy, soaking up at least one half of the incoming solar radiation in the surface layers of the tropical oceans. Some of this stored energy then provides the driving force for atmospheric circulation, the remainder being distributed around the globe through geostrophic and wind-induced currents (Hamon and Godfrey, 1978).

This project attempts to answer some of the questions relating to the changing regional-scale oceanography of Western Australia, and as a consequence, changes to global climate attributable to changing oceanic circulation.

Western Australian regional oceanography is an anomalous condition when compared to other eastern (ocean) boundary climates. This oceanography is dominated by the poleward flowing LC, a narrow (< 100 km), shallow (< 250 m) stream of low salinity, low nutrient water that has its origin in the tropics and flows at relatively high speeds (up to 1.8 m s^{-1}) against the climatological mean equatorward winds (Church *et al.*, 1989; Cresswell and Golding, 1980).

In order to develop an understanding of the changing climate, and to better predict expected ranges of climate into the future, analysis of empirical model output in collaboration with continued field-based assessment is required.

Global Climate Models (GCM's) have been developed since the early 1980's. These models have been developed to attempt to allow a general understanding of climate and its operation, by utilising the equations of motion to simulate climate progression and development. Exponential growth in computing power has allowed these models to incorporate a large portion of the components of the climate system, with current models incorporating, atmosphere, land surface, ocean and sea-ice, sulphate and non-sulphate aerosol, carbon cycling, dynamic vegetation and atmospheric chemistry components (Houghton *et*

al., 2001). These are then combined to attempt to simulate the processes occurring in our dynamic climate system, providing predictions for climate of the future.

Due to the growing interest in the changing climate regime, and the belief that anthropogenic causes are the main driving force for this change, many international studies have been commissioned since the late 1980's, attempting to further our understanding of the role of humankind in this process.

Key questions to be investigated in this study are: What are the key variables that reflect changing patterns to climate? How do changes to ocean circulation affect current and heat-transport systems? What is the modelled change to oceanography, for the corresponding 70 and 100-year predictions, and how is this likely to affect Western Australian climate? and, how well does the model output agree with recent work - do these results conflict, or support, other studies of climate change?

This thesis is organised as follows. Chapter 2 describes the regional oceanography of Western Australia, summarises some key studies for this region and the Indian Ocean and reviews the model reproduction of regional oceanography. Chapter 3 introduces the datasets, assumptions and methodology utilised within the study. Chapter 4 explains the results that this study has uncovered. Chapter 5 discusses the relevance of these results to other studies and the likely changes to climate that have been predicted by the IPCC studies (Houghton *et al.*, 2001). Chapter 6 examines the success of this study and looks to the future to see what lies ahead of oceanographic research in this region.

Appendix A lists the complete set of acronyms and abbreviations utilised in this study.

CHAPTER 2
WESTERN AUSTRALIAN REGIONAL OCEANOGRAPHY

2.1 Introduction

Over the last 25 years Western Australia has experienced a significant decrease in rainfall (Allan and Haylock, 1993; Allan and Hunt, 1999; Indian Ocean Climate Initiative [IOCI], 2001, 2002; Nicholls, 1989; Nicholls *et al.* ,1999; Smith *et al.*, 2000; Suppiah *et al.*, 2001). Recent work by the IOCI (2001, 2002) indicates that the marked change to rainfall since the mid-1970's, was not a gradual decline, but more a switching to an alternate state, with a corresponding 15 - 20% decrease since the early 1900's. Concurrent with the changing rainfall, Australia's continental-average temperature has risen by a value of 0.7^oC since 1910 (Commonwealth Science and Industrial Research Organisation [CSIRO], 2001). Corresponding global average surface temperature (the average of near surface air temperatures over land and SST) values have indicated a changing pattern, with observed increases since 1861. The 20th century has been the most marked by this change, with increases of 0.6 ± 0.2^oC (Houghton *et al.*, 2001).

Climate change models incorporating increased CO_2 forcing suggest that Western Australia will continue to experience increases to atmospheric temperatures between 0.2 - 0.4^oC per decade for south Western Australia (Houghton *et al.*, 2001).

Averaged global warming of 1.4 - 5.8^oC by 2100 has been predicted by coupled atmosphere-ocean models (relative to 1990). When this is related to recent observations; 1998 was the warmest year in global instrumental records (since 1861) and the 1990's the warmest decade of the 20th century, global climate change may be indicated. Similarly

oceanic temperatures have increased, with SST increasing by 0.4 - 0.8^oC since the late 19th century, and global ocean temperature (for the top 300 m) increasing by 0.4^oC per decade since the 1950's (Houghton *et al.*, 2001).

The climate system consists of many smaller intrinsically linked components. These include; the atmosphere, oceans, land surface, cryosphere (ice sheets) and the biosphere. Current science acknowledges the linkages between these systems, with comprehensive climate models incorporating each of these systems in sub-models along with the processes that go along within and between them. These models then utilise the physical laws of nature, represented by mathematical equations, solved using a three-dimensional grid over the globe.

The intrinsically coupled nature of the atmosphere-ocean interaction has been highlighted by climate scientists, attempting to link changing SST and ocean circulation to atmospheric circulation patterns. Studies such as; Ansell *et al*, 2000; Drosdowsky, 1993; Frederiksen *et al.*, 1999; Nicholls, 1989; Simmonds, 1990; Simmonds and Rocha, 1991; Simmonds *et al.*, 1992; Smith, 1994; Smith *et al.*, 2000 and Streton, 1981, have uncovered a highly correlated relationship between Indian Ocean state and Australian precipitation.

Although observed and predicted changes to rainfall are documented, the physical mechanisms that express these changes are not well understood. Simmonds (1990) and Simmonds and Rocha (1991) have positively linked the role of warmer ocean temperatures (Indonesian-central Indian Ocean SST gradient) off Northwest Western Australia to the development of increased winter rainfall across Australia (when comparison is made to other eastern [ocean] boundary climates). Similarly Wright (1997) has linked the tropical source region off the NWS to the development of tropical-extratropical cloudbands (and their interaction with frontal systems to the south), these features being responsible for 20 - 25% of south Western Australia's (early season) April to October rainfall (Telcik and

Pattiaratchi, 2001; Wright, 1997).

2.2 Climate - Atmosphere and Oceans

The southern hemisphere has suffered from a comparatively sparse network of land-based meteorological stations. Only about 20% of the southern hemisphere is covered by land or ice, compared to nearly 40% for the northern hemisphere. Major gaps in coverage by surface based weather stations over the oceans, in deserts, large areas that have not been urbanised (such as jungles and high mountains) and the poles (Antarctica and the Arctic circle) ensure that our understanding of the global climate system is inconsistent.

It has been noted that almost half of solar radiation entering the earth-atmosphere is absorbed by the surface layers of the tropical oceans. Some of this energy provides the driving force for atmospheric circulation, with the rest distributed around the globe by wind and density-driven ocean currents (Hamon and Godfrey, 1978). Recent climate work has recognised the intrinsic link between these separate climate system components, with specific interest in the atmosphere-ocean interaction, and therefore it has become necessary to view the global climate system as a whole (Hobbs *et al.*, 1998).

2.2.1 Western Australian Atmospheric characteristics

Australia is the smallest, flattest and most southerly situated continent, extending over only 35° of latitude. Apart from Antarctica, it is the driest continent, but includes a wide range of climates from the tropical north, through the arid interior to the temperate south. At least 4 major factors determine the characteristics of Australia's climate, these include; its size and shape, location surrounded by vast oceans, location under the sub-tropical high pressure belt of global circulation and subdued relief (Hobbs, 1998).

Western Australia extends from 15 - 35^oS, 111 - 129^oE, stretching across latitudes

that (almost) encompass the whole of Australia. This extension ensures that the state experiences a wide range of atmospheric phenomena, stretching across the temperate cool climate of the south, to the warm tropical climate of the extreme north. Perth is Australia's windiest city, exposed to westerly gales in winter and strong seabreezes in summer. The annual mean windspeed of 4.3 m s^{-1} is about 30% above that of most other Australian capitals, principally southerly in origin (Hobbs *et al.*, 1998; Linacre and Hobbs, 1977). The most dominant atmospheric feature for this region, the sub-tropical high pressure belt, is responsible for these conditions. Similarly, this system dominates Western Australian climate, with winter rains linked to the equatorward migration of these systems during the months April to October, and the dry summer patterns due to the dominance of these systems over the sub-tropical and mid-latitudes November to March.

The dominant nature of the sub-tropical high pressure belt (over Southwest Western Australia [SWWA]) has been indicated by Gentilli (1972a); '. . . The sub-tropical belt of high pressure extends across this region during the summer months, reaching its southernmost extension in January or February. During the autumn it gradually moves towards the north and lies almost wholly outside the region during the winter months. In the spring a gradual southward shift occurs . . . '.

Rainfall for this region is chiefly due to the mid-latitude cold frontal systems that develop in the Southern Ocean, with 80% of SWWA rainfall falling between May and October (Wright, 1997). Telcik and Pattiaratchi (2001) and Wright (1997) have extended this to include the northwest cloudband phenomena. Combination of these with frontal systems, responsible for a considerable portion of rainfall over southwest, central and eastern Australia, most of these occurring in the early months of the (winter) season.

2.2.2 Western Australian Ocean characteristics

The western coast of Australia has been studied infrequently since the earliest studies of CSIRO Division of Fisheries and Oceanography by Rochford in 1969. A summary detailing physical oceanography studies extending from the Northwest Cape ($21^o47'S$) to Cape Leeuwin ($34^o22'S$), from the surf zone to deep oceanic water, and including studies from 1930 through to 1983, was published by Pearce (1983). The most relevant study of this area is the LeeUwin Current Interdisciplinary Experiment (LUCIE), undertaken in two parts - through September 1986 to January 1987 and February to August 1987. This study concentrated mainly on the dominance of the LC and its effect on the oceanography of the area. Studies of the inner-shelf region and its associated flows where not undertaken, as these occurred in much shallower water depths, whereas the LC was centred over the 200 metre isobath extending seaward (Cresswell, 1996).

The region off Western Australia is geographically and topographically the analogue of the other regions where eastern boundary currents occur. Similarly, the winds off Western Australia blow predominantly equatorward, just like those of corresponding regions (Gentilli, 1952, 1991; Masselink, 1996; Pattiaratchi *et al.* 1995; Smith, 1989) and are strongest in the summer months and weakest in winter (Gentilli, 1991). The behaviour of the oceanic system off the coast, however, is anomalous to these other eastern boundary systems. Although local wind conditions are ideal for the development of coastal upwellings, these are somewhat suppressed by the dominance of the strong poleward flow of the LC (Church *et al.*, 1989; Pearce, 1991, 1997; Cresswell and Golding, 1980; Smith *et al.*, 1991). Godfrey and Golding (1981) also indicate that the presence of this condition is responsible for the anomalous warmer water off Western Australia (when compared to other eastern boundary regions), with these waters $\sim 3^oC$ warmer in the upper 300 m, a response to LC flow. This condition, anomalous to other eastern boundary flows, domi-

nates the region, extending west to 1000 metres (in large offshoot eddies) from the coast of Western Australia, and hindering continuous equatorward flows (Andrews, 1977). This phenomenon has been noted by several prominent studies of the area such as Godfrey and Ridgway (1985), Holloway (1995) and Smith *et al.* (1991). Recent studies by Gersbach *et al.* (1999), Pearce and Pattiaratchi (1999) and Taylor and Pearce (1999) have disputed this conclusion, determining inner-shelf (< 50 m depth) upwelling and the equatorward flows of the Capes Current (CC) and the Ningaloo Current (NC) respectively. These flows appear during periods of decreased LC flow (November to March) moving off the shelf-break seaward, and strong equatorward windstress resulting in Ekman-driven transport offshore. These flows occur during the summer periods of high equatorward windstress and low LC flow, flowing along the inner-shelf inside the LC.

Figure 2.1 indicates the location of key surface currents within the study area, corresponding SST's and coastal locations. From this figure, the dynamic current system off the Western Australian coast is apparent. On close inspection of the inner-shelf region, it appears that there is an equatorward current present off Perth, possibly linking the equatorward CC flow to the NC in the extreme north. Church *et al.* (1989) summarised the annual flow regime off Western Australia through the findings of the LUCIE study, and concluded that there were defined seasonal patterns from spring/summer and autumn/winter. They concluded that the greatest variability occurred in the spring/summer period, when both poleward and equatorward flows were recorded. The first four months of the winter study (February to August 1987) indicated a strong poleward flow (LC), with a weakening of this flow occurring only in the last two months of the study. The weakening is possibly due to decreased IT flow corresponding with a strong El Niño event, strongly linked with the Pacific windstresses, a forcing feature for regional oceanography (Clarke and Liu, 1994; Meyers, 1996).

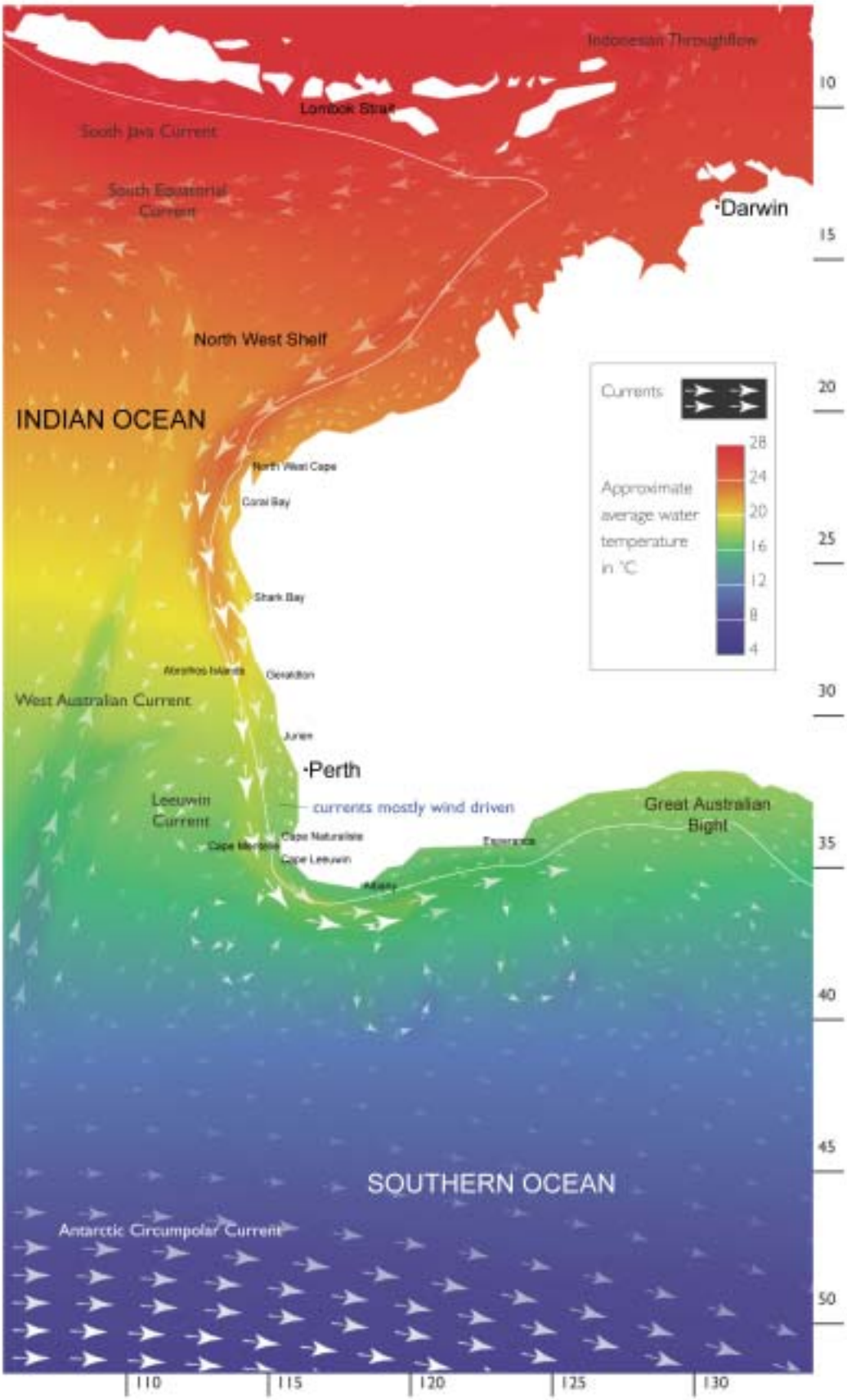

Figure 2.1: Regional map of the study area *(From Laughlin, 1997)*

2.3 Forcing mechanisms for regional oceanography

The Indian Ocean basin incorporates a wide range of ocean climates. The smallest of all oceans (including the Southern Ocean), the Indian Ocean extends from the high southern latitudes (45^oS) bordered by the Antarctic water of the Southern Ocean, to the equatorial regions, and up to 20^oN in the Arabian Sea (a north-south extent of 9600 km - Antarctica to the inner Bay of Bengal, and 7800 km east-west - southern Africa to Western Australia). The dominance of the Asian landmass in the northern latitudes limits the extent of this ocean. A monsoonal climate dominates the northern component of the Indian Ocean, the effects of this felt far into the subtropics of the southern hemisphere (Tomczak and Godfrey, 1994).

Figure 2.2 summarises the summer monsoon (West Australian winter - July/Aug) circulation pattern of the entire Indian Ocean. Transport values were derived from ship-drift climatologies and drifters, indicating flow in Sverdrups ($Sv = 10^6$ m^3 s^{-1}). Figure 2.3 summarises the winter monsoon (West Australian summer - Jan/Feb) circulation pattern (Current acronyms are included in Appendix A).

The southern hemisphere component is dominated by the sub-tropical high pressure belt, whose axis is located around 36 - 38^oS (Hobbs, 1998). The pressure gradient between this system and the tropical low pressure belt (located at 10^oS) drives the south-easterly trade winds in this region (Gentilli, 1972a; Tomczak and Godfrey, 1994).

2.3.1 The Indian Ocean - Sub-tropical Gyre

A basin-wide anticyclonic flow, the Indian Ocean sub-tropical gyre is an analogue of the South Atlantic Gyre and the South Pacific Gyre, bordered by the SEC in the north, the East Madagascar Current (EMC) and Agulhas Current (AC) in the west, Antarctic Circumpolar Current (ACC) in the south and interacting with regional oceanography as

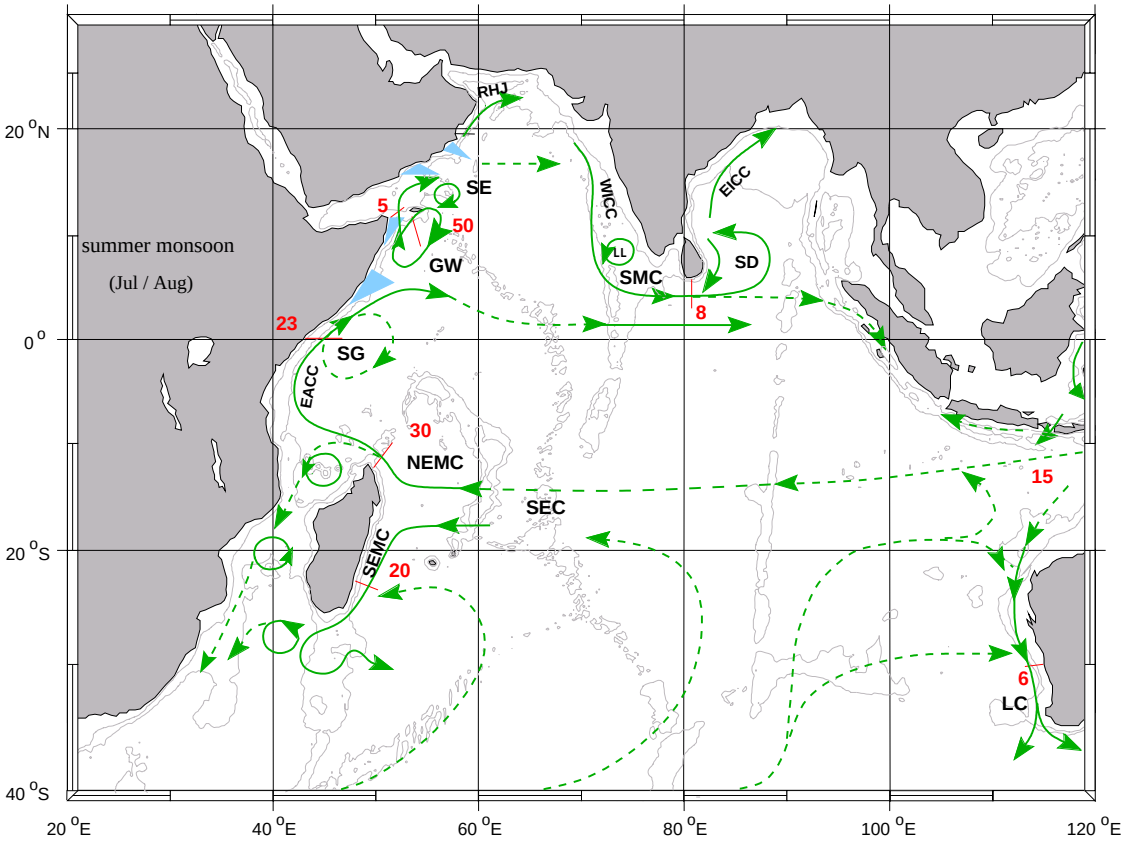

Figure 2.2: Indian Ocean winter circulation *(from Schott and McCreary, 2001)*

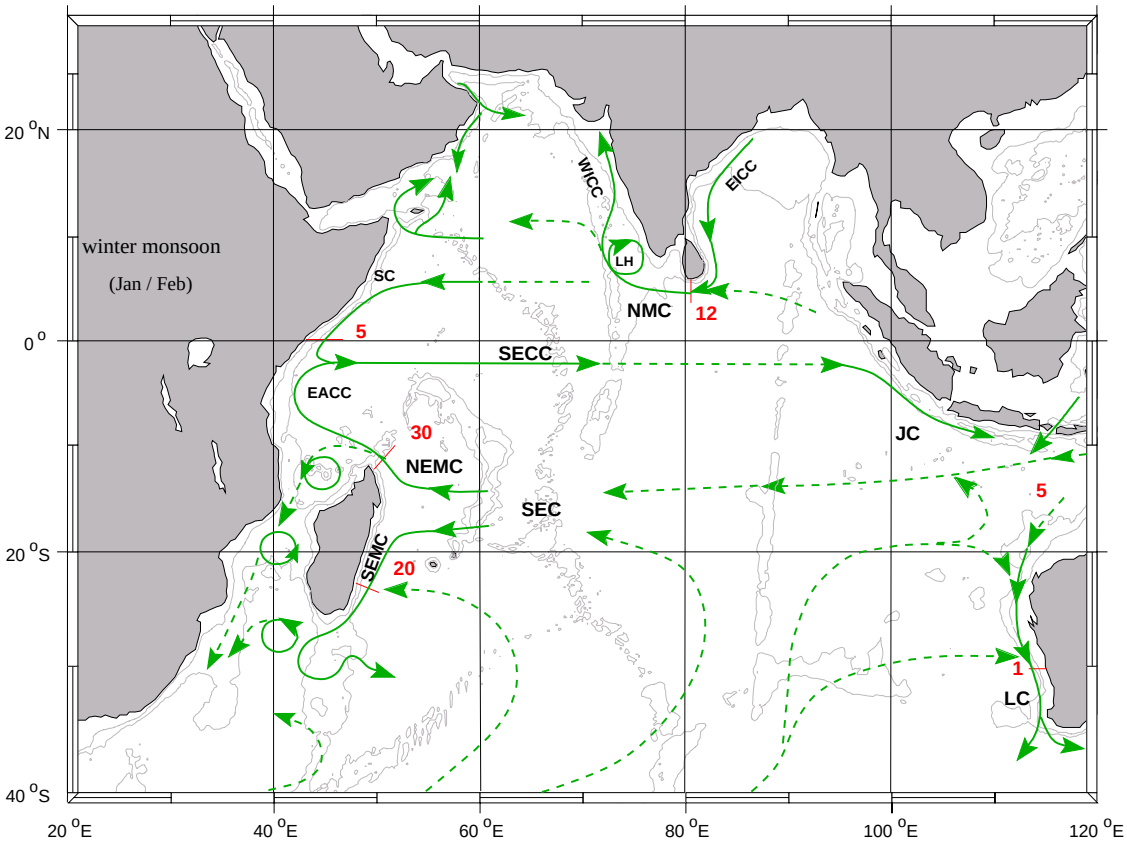

Figure 2.3: Indian Ocean summer circulation *(from Schott and McCreary, 2001)*

the WAC.

This flow is chiefly driven by windstress (roaring forties - south, and the south-easterly trades in the low-latitude and equatorial region - north) and feeder flows such as the SEC and ACC, expressed in nearshore oceanography as boundary flows (EMC and AC in the east - western boundary, and West Australian Current (WAC) in the west - eastern boundary). Shenoi *et al.* (1999) indicate that the southern gyre is more defined compared to its northern (hemisphere) counterpart, the northern Indian Ocean gyre, due to the strong defined boundary currents driving this anticlockwise flow and the lack of these in the northern hemisphere.

2.3.2 The Indonesian Throughflow

The IT has long been a focus of considerable local and international research. Globally it is considered one of the choke points of the oceans' THC system, linking the equatorial flows of the Pacific Ocean, to the Indian (through the SEC and complimentary flows) and Atlantic Oceans. Its variability is believed to affect climate on interannual and longer time scales, limiting meridional transport in ocean systems (Broecker, 1991; Gordon, 1986; Gordon and Fine, 1996; Meyers, 1996; Schneider, 1998; Schott, 2001).

The annual mean IT is directed from the North Pacific, via the Mindanao Current, through the northern Indonesian archipelago, chiefly through the Makassar Strait, into the Banda Sea and finally past Timor into the Timor Sea, flowing then into the north eastern Indian Ocean (Godfrey, 1996; Schott, 2001). Considerable flows through the southern Indonesian archipelago, such as the Lombok Strait and Sunda Strait have also been observed and represented in model output (Arief and Murray, 1996; Coatanoan *et al.*, 1999; Gentilli, 1972b; Lukas *et al.*, 1996; Qui *et al.*, 1999; Schiller *et al.*, 1998; Tomczak and Godfrey, 1994). The IT passes westward with the SEC, a component of this, directed south and

feeding the Leewuin Current Source region (LCS), driving the LC flow.

Numerous expendable bathythermography (XBT) and model studies have attempted to categorise and quantify this flow. A review of the IT by Godfrey (1996) indicated that the best known estimates of IT flux was by Fieux *et al.* (1996), indicating August (winter) flows of 18.6 $\pm$ 7 Sv, and February (summer) flows of -2.6 $\pm$ 7 Sv (the Eastern Gyral Current [EGC] Meyers, 1996). Work by Meyers, with 10-yr XBT data, indicated that the top 400 m flow was very strong and seasonal, with Fieux's values occurring near Meyers' highest and lowest values respectively. Meyers indicated that mean values of $\sim$7 Sv are representative of this flow.

2.3.3 The South Equatorial Current

The Indian Ocean SEC is supplied by the IT, with the south easterly trade winds nourishing this flow across the equatorial Indian Ocean. Shenoi *et al.* (1999) describe this as a broad westward flow occurring between 8 - 16^oS, acting as the boundary to the northern (clockwise) tropical gyre, and the southern (anticlockwise) subtropical gyre south of the equator. This flow extends the width of the Indian Ocean, reaching Madagascar and dividing to form the East African Coastal Current (EACC), the EMC and the AC further south.

The SEC has a clear seasonal signal, with peak flows in April, linking well with peak IT flow (Shenoi *et al.*, 1999). Interaction between the seasonal south-easterly trades around this region leads to the development of westward propagating Rossby waves, which in turn manifest an annual cycle in the SEC (Shenoi *et al.*, 1999). Recent work by Baquero-Bernal *et al.* (2002), Rao (2002), White (2000b, 2001) and Xie *et al.* (2002) indicate that the Rossby wave propagation has a key role in the development of the observed Indian Ocean Dipole (IOD) mode, with teleconnections to the Pacific Ocean and El Niño Southern

Oscillation (ENSO) (Clarke and Liu, 1994: Meyers, 1996).

Fine (1985) indicated that the SEC has a mass flux of between 30 - 40 Sv and is strongly seasonal. Schott *et al.* (1988) indicate the SEC transport above 1100 m to be 39 Sv (across 54^oE of longitude), this flow extending from 11 - 23^oS, with Levitus82 density and salinity fields indicating 39.4 Sv with the maximum value obtained in July and minimum in February. Meyers (1996) suggests that the SEC flow (taken from XBT data extending from Fremantle to the Sunda Strait) is of the range 5 - 18 Sv with a mean flow regime of $\sim$10 Sv. This transport is due to the feeder flows of the IT and the input from the WAC to the south, agreeing well with transport values.

2.3.4 The Antarctic Circumpolar Current

Driven by the strong westerly windstress around the Antarctic Pole, the ACC exists in the Southern Ocean from 40 - 60^oS, the only continuous ocean encircling the globe. With the largest volume transport of any current system, ACC flow is the unifying link between ocean heat and salt exchange at all depths globally (Blanke *et al.*, 2001; Broecker, 1991; Doos, 1995; Gordon, 1986; Hamon and Godfrey, 1978). Due to these exchanges having a strong influence on mean global climate, it is likely that the Southern Ocean plays an important role in transmitting climate anomalies around the globe (White and Peterson, 1996). Recent work by Sloyan and Rintoul (2001) with conductivity temperature depth (CTD) sections across the Southern Ocean has indicated transports of 135 Sv at Drake Passage (60^oW) and South Africa (0^oE), increasing to 146 Sv south of Australia (150^oS), with the net transport dominated by Subantarctic and Polar fronts.

White and Peterson (1996) indicated the presence of the Antarctic Circumpolar Wave (ACW) a dominant feature incorporated in the Southern Ocean ACC, affecting global climate on an 8-year cycle. The ACW is observed by patterns of mean sea level pressure

(MSLP) and corresponding windstress, SST and sea-ice extent in the high-latitude Southern Ocean encircling easterly, around the Antarctic pole. These anomalies have been hypothesised to drive observed climate, with linkages to the El Niño cycle apparent from historical data (Dr David Stephens *Pers. Comm.* Agriculture WA, 12-09-02; Peterson and White, 1998), patterns of Australian precipitation (White, 2000a) and direct communications to the sub-tropical gyres of each ocean (White and Peterson, 1996).

2.3.5 Deep Ocean Circulation

Motion of water in the deep (2 - 5 km) oceans is not well known or understood. Such flows are interlinked with the global conveyor belt of oceanic circulation, a global warm (surface) and cool (deep ocean) water circulation that encompasses each of the global oceans. This circulation is believed to be responsible for the large flow of upper ocean water from the tropical north Pacific Ocean, through the Indonesian archipelago (forming the IT) and into the Indian Ocean (Broecker, 1991; Gordon, 1986). Deep water formations such as North Atlantic Deep Water Formation (NADWF) and Antarctic Bottom Water Formation (AABWF) are an intrinsic components of the THC. Predicted changes to this circulation, modelled by Global Climate Models (GCM) and attributable to increasing CO_2 forcing, suggest THC will break down (Cai and Gordon, 1998), leading to considerable decreases in European temperatures (the presence of the Gulf Stream being the reason higher temperatures are experienced).

2.4 Summary of Regional Currents

5 currents have been observed. These currents dominate the regional oceanography of Western Australia, with the LC being the most dominant of all the currents in the region. Each of these individual currents is intrinsically connected to flows of other currents within

this regime. For example a strong LC flow may ensure that equatorward counter-currents are suppressed, and conditions of weak LC flow may have the opposite effect.

2.4.1 The West Australian Current

This WAC is an analogue of the Benguela Current (South Africa/South Atlantic) and the Humbolt/Peru Current (South America/South Pacific). A strong equatorward flow to the west of the LC identifies the WAC (see Figure 2.1). It completes the south-eastern arm of the subtropical Indian Ocean Gyre, an oscillation that follows a large-scale anticlockwise motion and is replicated in all southern hemisphere ocean basins (Pernetta, 1995; Thompson and Veronis, 1983; Tomczak and Godfrey, 1994).

Andrews (1977) indicated that the WAC provides an eastern inflow to the LC at the approximate latitude 30 - 34^oS, turning south near the coast between 29 - 31^oS. More recent studies have supported this finding, suggesting it enters further south at 30 - 33^oS, possibly being entrained in the poleward LC flow (Church *et al.*, 1989). Gersbach (2000) also indicated that the WAC may provide a southern border to the LC at $\sim$37^oS. It is possible that the current intensity increases as it rounds Cape Leeuwin and proceeds into the Great Australian Bight (Cresswell and Peterson, 1993; Gersbach, 2000; Smith *et al.*, 1991). Alternatively, these flows may combine, increasing in volume and velocity as they move poleward (Church *et al.*, 1989).

It must be noted also, that the study by Andrews (1977) named the eastern inflow (29 - 31^oS) and continued poleward flow the WAC. It was not until Cresswell and Golding (1980), that this poleward flow was renamed the LC after the Batavia-bound Dutch ship the first to explore southern Australia.

Andrews (1977, 1983) and Cresswell and Peterson (1993) have indicated that studies of the WAC have chiefly been undertaken in summer months (Andrews' principle study

was undertaken over the periods; midsummer of 1972 and early and late summer in 1973). The absence of observations throughout the winter months does not provide a conclusive understanding of this current flow. This may indicate that the WAC and LC are mutually exclusive. If this is the case, it is possible that the summer pattern that was discovered by Andrews (1977) was in fact an expression of the WAC, flowing eastward and then poleward (possibly entrained by the LC) when it neared the coast between 29 - 31^oS. Andrews (1983) indicated that an inflow entered the LC flow between 30 - 34^oS, varying in direction from east to north-east and with a width from 100 - 200 km, very narrow when compared to other eastern boundary currents. This current flow was noted to leave eastward into the Great Australian Bight when it rounded Cape Leeuwin, mimicking the flow of the LC.

Andrews (1983) indicated that, as is expected from an eastern boundary current, the WAC is shallow, with 66% of the total mass transport (surface to 1300 m), contained in the surface to 400 m depths. Similarly, he summarised that the WAC transports marginally less volume than a typical eastern boundary current system, with a representative flow of 10 Sv, compared to values of 18 Sv and 15 Sv for the Humboldt and Benguela currents respectively. Andrews (1977) also indicated that the eastward transport of the WAC (30 - 34^oS) into the LC flow is quite near to the averages of the eastern boundary currents; California, Humboldt and Benguela, at the depth of 370 m.

Satellite imagery from summer months (November to March) indicates that warm water (the LC) still flows (however it is heavily moderated, with increased equatorward windstress and decreased IT feeder flows) and for this reason it is fair to assume that the WAC supplements LC flows (Gersbach, 2000). Church *et al.* (1989) concluded that the WAC, indicated by the north-eastward inflow of high salinity water, dominates the summer situation, and combines with the LC to flow eastward into the Great Australian Bight.

It is interesting to note that an early study by Hamon (1972) indicated there was no

sign of the regular equatorward WAC that has been documented on many current charts. This conclusion was drawn from data collected over a total of 6 cruises to a maximum depth of 1500 m. A possible explanation for this anomaly may be attributable to the season or localised conditions under which measurements were taken. If there was a strong LC and associated eddies flowing at this time, there may have been no remnant equatorward flows of the WAC (this is unusual however as 1965 and 1969 (the study period) have been indicated El Niño years - as a result decreased LC flow would be expected [Clarke and Liu, 1994; Meyers, 1996]). The LC is most apparent at the western extent of the continental shelf, a depth of 200 m, with large-scale associated eddies extending into the Indian Ocean hundreds of kilometres (Cresswell and Peterson, 1993; Pearce, 1991).

2.4.2 Indian Ocean Central Water - Geostrophic Current

Indian Ocean Central Water (IOCW) is a major feeder mechanism for regional oceanography, and combined with the surface WAC, is one of the controlling mechanisms for the LC and SWWA ocean climate. Geostrophic in origin, Seidov and Haupt (1997) indicate (from a modelled Ocean Global Climate Model [OGCM] experiment) that this flow begins in the deep ($>$ 1500 m) western Indian Ocean between 0 - 10^oS, and travels south-easterly to reach Western Australia and interact with regional oceanography as the IOCW/WAC intrusion. The intrusion, entrained in the LC flow, brings higher salinity central Indian Ocean water south and around Cape Leeuwin, travelling into the Great Australian Bight and the Southern Ocean (Cresswell and Peterson, 1993). This is the least documented component of the oceanography of the region.

2.4.3 The Leeuwin Current

The LC is the most dominant current of Western Australian oceanography. It is a narrow ($<$ 100 km), shallow ($<$ 250 m) stream of low-salinity, low-nutrient water that has

its origin in the tropics and flows at relatively high-speed against the climatological mean equatorward winds. Maximum-recorded speeds of 1.8 m s^{-1} have been documented south of Cape Leeuwin (Church *et al.*, 1989).

First documented by Gentilli (1972b), who indicated that the Pacific through-flow, flowing in autumn and winter reverses during the spring, when the IT weakens, this 'stationary' water then warms over the following spring-summer, reaching thermal homogeneity of 27^oC above 20^oS by February. The following March-April this water then extends south westward, fed by the renewed IT, becoming the LC and extending south beyond Cape Leeuwin.

It is now known that this current flows strongly in the autumn and winter months, with flow moderated throughout summer and spring (Cresswell *et al.*, 1989; Cresswell and Peterson, 1993; Gersbach *et al.*, 1999; Godfrey and Ridgway, 1985; Smith *et al.*, 1991). An early study by Hamon (1972) also indicated the presence of this current during the autumn/winter, with poleward flows recorded. Rochford (1969) strongly supported the concept of the winter LC flow, with salinity profiles indicating the seasonal variation. He indicated a surface salinity change from 35.8 *ppt* to 35.2 *ppt* from summer (December to February) and winter (July to September) respectively at a fixed station off Rottnest Island, and found that the salinity gradient diminished westward, replicating the pattern of the LC as presently known.

Andrews (1983) indicates that the LC was only identified during the winter months, and also observed that both the WAC and LC are similar south of 29^oS (these both leave to the east across the Great Australian Bight), so much so that it may be impossible to differentiate between them. This poleward flow (south of 29^oS) has historically been considered the LC.

Studies by Andrews (1983) and Smith *et al.* (1991) indicated that the LC originated

along the North West Shelf at the latitude of $\sim 22^oS$ and was sourced by the IT of the Pacific Ocean. Thompson (1984) and Godfrey and Ridgway (1985) summarised the LC origin as a result of the large along-shore steric height pressure gradient. This pressure gradient exists between the warm (low-density) equatorial waters and the cool (high-density) Southern Ocean. Pearce (1991) extended this to indicate that '...the meridional gradient that is setup by this density difference, is far stronger than the equivalent eastern boundary regions. This pressure gradient then induces a net eastwards geostrophic flow from the Indian Ocean towards Australia. This flow is then directed southwards by the continent to form the Leeuwin Current ...'.

Work by Godfrey (1996) reviewed literature relating to Indian Ocean studies, with specific interest in the IT. He concluded that '...when the Indonesian passages are open, coastally trapped waves can propagate rapidly from the equatorial Pacific to the northwest Australian coast. These waves act strongly to bring temperatures at each depth along the northwest Australian coast toward the very high values found in the western equatorial Pacific. Consequently, mean steric heights off northwestern Australia are also quite similar to those found in the western Pacific making them higher than those off any other eastern boundary of the world by some 0.3 - 0.6 m (from Levitus Ocean Atlas [1982]). Water temperatures at 50 m off northwestern Australia are about 7 - 10^oC warmer than at similar latitudes of western Africa and America. South of 20^oS, the overlying atmosphere is colder, so such high temperatures must result in heat loss to the atmosphere. This reduces the temperatures progressively with distance southward in the top 100 - 200 m near the coast, which also lowers the steric height substantially. A 'density current' system develops throughout the southern Indian Ocean to maintain geostrophic balance, this is known as the Leeuwin Current extension ...'.

It is likely that this pressure gradient is also the cause of the IOCW/WAC intru-

sion further south (29 - 34^oS), the pressure gradient driving a westward geostrophic flow, supplementing the IOCW intrusion.

Benny and Mizuno (2000) have categorised the steric height in the Indian Ocean. Calculated steric height values from 11,000 temperature-salinity plots relative to 400 db (400 m depth) supported the conclusions of previous authors. They indicated that a mean gradient (IT [10^oS] to Jurien [30°]) of 0.04m was present in the sample, with similar values for January-February, increasing to values > 0.05 m for March-October and returning to the lower values during November. The steric gradient signature was clearly effected by the IT and SEC flows of the mid-year, with these gradients extending across the Indian Ocean (80 - 90^oE) during the July-October period, peak periods of IT/SEC flow. It is likely that work south of 30^oS would have indicated a more marked gradient, due to higher salinities, lower temperatures and corresponding increased densities of the ACC and the Southern Ocean.

The LC is most apparent at the western extent of the continental shelf (at a depth of 200 m) and extends seaward during the summer months. Large-scale associated eddies extending hundreds of kilometres into the Indian Ocean have been observed through satellite images during peak LC flow.

The WAC eastward inflow has been little studied in winter, and the LC little studied in summer. Presently it is not known whether these currents co-exist or are mutually exclusive (Andrews, 1983), however, any combination of these flows have historically been considered the LC.

2.4.4 The Leeuwin Undercurrent

The Leeuwin Undercurrent (LUC) is one of the least known regional currents. Studies by Thompson (1984, 1987) indicated that there was indeed an equatorward undercurrent

flowing along the upper continental shelf at a depth of 300 metres off Shark Bay. Additional studies by Cresswell and Peterson (1993) have also noted the presence of this current, indicating values of 0.3 m s^{-1} peaking at 400 m depth and extending to 750 m at Cape Mentelle (CM - 34^oS). The LUC was observed carrying higher salinity subtropical water in both an equatorward and westward direction.

Current meter data from the LUCIE experiment (Smith *et al.*, 1991) followed the observations of Thompson (1987) and indicated that the equatorward undercurrent was narrow and situated between 250 and 450 m in depth on the upslope of the continental shelf. The speed of the undercurrent has been measured at 0.3 m s^{-1} between depths of 250 - 350 m (Smith *et al.*, 1991).

The seasonal variation of the LUC is unknown at present, however it has been suggested that the current is driven by an equatorward pressure gradient located at the depth of flow (Thompson, 1984). It is possible that this flow attempts to balance the flow of the LC and IOCW, flowing from the Southern Ocean (Great Australian Bight) equatorward along the Western Australian coast, extending seaward beneath the IOCW.

2.4.5 Inner-shelf Currents

The inner-shelf region is a sub-grid scale feature of the Mark 3 model output. Currents included in this section exist on the inner continental shelf ($<$ 200 m depth) with corresponding flow widths of $<$ 50 km. Current Ocean Global Climate Models (OGCM's) have no way of resolving such features. However, output from the Mark 3 model, indicating upwelling and Ekman transport, may be inferred to drive sub-grid flows.

The inner-shelf region is subject to strong seasonal variation, with current flows altering over the seasons 180°, from poleward in winter (due to the persistence of the LC) to an equatorward drift in the summer months attributable to the strong southerly winds

of this season (Cresswell *et al.*, 1989). This extreme variability has been documented by several studies. Rochford (1969) indicated the seasonally reversible nature of the region (LC during April to October [winter] and equatorward flows during November to March [summer]), and Hamon (1972) indicating that circulation is variable, similar in character to the east coast, however maximum currents are less (LC compared to the East Australian Current [EAC]).

The presence of inner-shelf, wind driven equatorward counter-currents to the LC have been noted by Cresswell *et al.*, 1989 and Pearce, 1997, as well as the specific studies of Gersbach *et al.*, 1999, Pearce and Pattiaratchi (1999) and Taylor and Pearce (1999), locating and identifying regional currents such as the CC and NC respectively. These currents are a response to local wind (seabreeze) conditions providing the drive for upwelling and the effect of the Coriolis force (directing flow to the left and away from the shore in the southern hemisphere) on the flow of inner-shelf water affected by the strong equatorward windstress.

2.4.5.1 The Ningaloo Current

Studies by Taylor and Pearce (1999) have indicated that there is an equatorward inner-shelf flow that they have traced through direct observation, aerial surveys, current drogues and analysis of satellite SST images. These images indicate that the equatorward flow is the dominant inner-shelf flow from September to mid-April each year. Previous studies have concluded that the lower temperature on the narrow inner-shelf is probably due to upwelling associated with internal wave activity.

Inner-shelf current data was collected somewhat haphazardly from a platform transmitter terminal (a satellite tag that was attached to a whale shark and became detached on 11th April 1991). The unit, which had a keel extending 30 cm into the surface water,

effectively became a current drogue, providing current data for a period of 29 days, indicating the nature of eddies running off the LC west of North West Cape. This 'drogue' indicated the reef front equatorward current to be flowing along both the North West Cape and Coral Bay, opposing the flow of the LC and supported by strong southerly winds.

Discovered by Taylor and Pearce (1999) the NC is the predominant equatorward current that flows along the reef front in the summer months. Aerial observations undertaken during daily Manta and Whaleshark spots, often indicated the concurrent flow of the equatorward shelf current (NC) and the poleward flowing LC a distance of 2 km from the shore, indicated by the comparatively calm nature of inner-shelf waters. The poleward flowing LC was pushing against the northerly winds creating a 'wind-versus-current' phenomenon.

Taylor and Pearce (1999) indicate that the NC flows when there is a strong summer southerly wind stress. Southerly wind stress has a weakening effect on the LC and it becomes less defined, moving offshore. An inner-shelf equatorward current fills this void, with an origin (from at least) the southern end of the Ningaloo Tract towards Point Cloates, and continues along the reef front. This current may be narrow and restricted, or (in periods of extreme equatorward wind stress) may extend well across the shelf and upper slope.

The NC has been observed flowing over a continuous period of 8 months and Taylor and Pearce (1999) suggest this to be the predominant flow of the inner-shelf region. Generalised patterns indicate that the equatorward counter-current to the LC flow is well established in the summer months with the strong southerly winds. April tends to be the month of transition into the winter pattern, when the LC dominates.

2.4.5.2 The Capes Current

Pearce and Pattiaratchi (1999) have discovered an equatorward inner-shelf current that flows strongly in summer and is attributable to upwellings along the upper continental shelf, the length of the Cape-to-Cape region (Gersbach *et al.*, 1999). This current is a '...cool, seasonal, inner-shelf current, which flows northwards against the along-shore steric height gradient in summer months when the equatorward wind stress is at maximum strength...'(Gersbach *et al.*, 1999). The current occupies the width of the continental shelf (20 km) between the southern Capes, Leeuwin and Naturaliste, then broadens northwards as it extends beyond Perth.

Previous studies by Cresswell and Golding (1980) confirmed this equatorward flow using drifter tracks over the summer of 1975 - 76. They concluded that the normal summer circulation of wind-driven equatorward flow over the shelf region is apparent, coincident with the poleward flow of the LC, seaward, over the shelf break. Figure 2.4 indicates the condition of the LC and CC flowing simultaneously, with equatorward windstress limiting the LC flow south.

Studies by Pearce and Pattiaratchi (1999) and Gersbach *et al.* (1999) have identified this current and its associated upwellings. Similar to the NC, the flow of the CC tends to be occur in the summer months, when southerly wind stress is driving the equatorward currents and providing a source for upwelling.

This CC is a seasonal, cool, inner shelf current moving equatorward from the Capes region of southern Western Australia. It is hypothesised to flow from Cape Leeuwin extending north of Perth, with Pearce and Pattiaratchi (1999) indicating flows may continue north to the Abrolhos Islands off Geraldton.

Upwelling has been observed occurring at Cape Mentelle, with conclusive studies by Gersbach *et al.* (1999) indicating this to be both lower in temperature then oceanic water

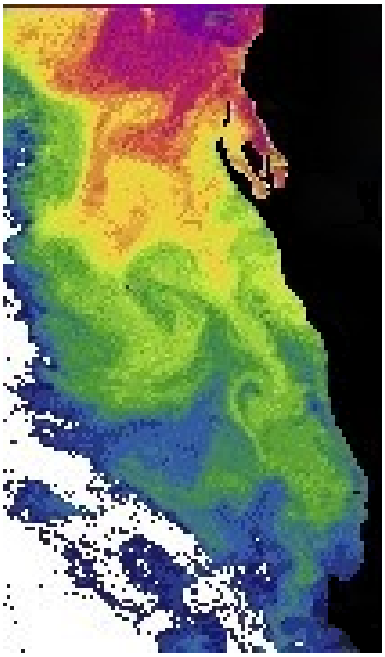

Figure 2.4: Leeuwin Current and Capes Current flows represented *(WASTAC image)*

from further south at Point D'Entrecasteaux and similar in temperature to ocean water off Albany, and, to have a salinity signature higher than that of Southern Ocean water, with a value of 35.8 *ppt*, compared to the value of 35.5 *ppt* for the Southern Ocean water.

SST images analysed by Cresswell and Peterson (1993) showing the presence of cool water moving equatorward, were reviewed by Pearce and Pattiaratchi (1999) who concluded that this anomalous poleward and parallel coastal flow is possibly the presence of the CC, inhibiting Southern Ocean water intrusion.

Further analysis of the temperature and salinity (T-S) signature of this upwelling indicates the similarity between this and the signature found at the base of the LC (at a depth of ∼50 m along the lower (200 m) terrace). This implies that the source of the upwelling is from the base of the LC flow, a conclusion supported by nutrient data, indicating low concentrations of nitrogen and phosphorous, similar to the LC flow (Gersbach *et al.*, 1999).

Acoustic Doppler Current Profiler (ADCP) data from the 15th - 18th December 1994

was analysed by Gersbach *et al.* (1999), indicating the presence of the equatorward CC inshore of the 50 m isobath flowing at ~0.15 m s^{-1}, reflecting the driving force of the mean equatorward winds. Simultaneously the LC was recorded flowing over the shelf break poleward at a speed of 0.4 - 0.5 m s^{-1}, indicating that the CC flow is chiefly confined to the upper terrace.

2.4.5.3 Capes Current Extension

Revision of *RV Franklin* cruise data allowed an analysis of the inner-shelf currents flowing along the coast between Cape Naturaliste and the Abrolhos Islands (off Geraldton) in the north. This current is effectively an extension of the CC flow and supports the hypothesis of Pearce and Pattiaratchi (1999) that the CC extends north of Perth. Franklin cruises 1/96 (11 - 28 January 1996) and 4/96 (22 - 29 March 1996) are the only data sets relating to inner-shelf oceanography for the region Perth to Geraldton. Cruise tracks are represented in Appendix B.

1/96 cruise data indicated highly variable results, however, an equatorward inner-shelf current and interaction with LC flow was present in the dataset. Of the 25 transects analysed, 7 indicated a strong equatorward surface flow. 3 transects also indicated upwelling taking place, nourishing surface flows. Peak current speeds of ~0.5 m s^{-1} were recorded at depths of between 20 - 40 m. The equatorward flows were strongest just below the surface (20 - 40 m), these flows extending to depths in excess of 120 m. Recorded current speeds tended to peak above the 50 m isobath.

The most positive signs were represented in the 4/96 cruise data. 14 transects were analysed, with 3 of these indicating strong surface flow. Peak current speeds exceeding 0.55 m s^{-1} were recorded, again peaking above the 50 m isobath. Following the pattern represented in the 1/96 cruise data, the flows were the strongest just below the surface

(20 - 40 m). There was only one transect that recorded an equatorward flow below 60 m, extending to 120 m.

2.5 Climatological Factors

2.5.1 El Niño and the Southern Oscillation Index

The ENSO phenomenon was discovered in the early 1960s. The Spanish term El Niño ('the Christ child') was used for centuries by South American mariners and fishermen to define the annual occurrence of warm, poleward flowing oceanic waters off Peru around Christmas each year (Carillo, 1892 - after Allan *et al.*, 1996). According to Hisard (1992 - after Allan *et al.*, 1996) the earliest documented scientific acknowledgement of anomalous ocean-current conditions, indicative of El Niño, occurred in the years 1791 and 1804.

The Southern Oscillation, named by Sir Gilbert Walker in 1924, summarised the pressure difference between the Indian (Cairo, north-west India, Darwin, Mauritius and South Africa - now Darwin) and Pacific (San Francisco, Tokyo, Honolulu, Samoa and South America - now Tahiti) regions (Allan *et al.*, 1996). Rasmusson and Carpenter (1982) were the first to link the El Niño oceanic cycle with the negative phase of the Southern Oscillation, calling this El Niño Southern Oscillation (ENSO) however, much of the basis of the understanding of the now-ENSO system is due to the work of Berlage, Troup, Bjerknes and Wyrtki, pioneers of the climate sciences (after Allan *et al.*, 1996).

The Southern Oscillation Index (SOI) is a variable that indicates the strength and state of the ENSO cycle. The ENSO phenomenon is an intermittent disruption of the climate system centred in the equatorial Pacific Ocean. El Niño, referring specifically to the warm phase of a large oscillation affecting SST, with increases to the central/eastern Pacific Ocean of up to 4^oC (from cooler mean 22 - 24^oC temperatures) and associated changes to the trade winds and rainfall patterns (Kessler, 2000). The corresponding cool negative

phase is termed La Niña with an intermittent or steady-state condition also occurring between El Niño and La Niña events. These changes greatly affect IT flow. Meyers (1996) indicates that La Niña conditions are associated with high IT flow, El Niño associated with low IT flow, with a 5 Sv difference peak to trough. It is clear then that this system greatly affects Western Australian regional oceanography.

The onset of El Niño is marked with a prolonged series of westerly wind bursts that release energy (stored in the western [central] Pacific Ocean as heat) to the eastern Pacific Ocean. Persisting for one to three weeks, this event overrides weak easterly trade winds (Webster and Palmer, 1997). The phase normally lasts from 8 - 10 months, with the entire ENSO cycle repeating itself within a 3 - 7 year cycle (Kessler, 2000; Webster and Palmer, 1997). El Niño is often accompanied by severe drought over Australia and Indonesia, and weakened summer monsoon rainfall over southern Asia. Across the Pacific Ocean, flooding often occurs along the Pacific coastline. Fish stocks (an indication of the nutrient balance) disappear as ocean upwelling (driven by trade winds containing cold sub-surface, high nutrient water) diminishes. The tendency for tropical cyclones in the Pacific is also heightened by this effect (Webster and Palmer, 1997). This corresponds with a decrease in the IT, SEC and possibly the LC during the period (Clarke and Liu, 1994; Meyers, 1996).

The La Niña situation is associated with stronger than usual rainfall in Indonesia and Australia, and coincidental severe drought conditions in equatorial Peru, returning to the upwelling situation and corresponding abundant fish stocks (Kessler, 2000). Heightened IT, SEC and corresponding LC flows occur during such an event (Clarke and Liu, 1996; Meyers, 1996).

Torrence and Webster (1999) have linked (atmospheric) Indian monsoon circulation to ENSO, illustrating an intrinsic link between these 'separated' atmospheric and oceanographic systems. The ENSO phenomenon therefore is linked to Indian Ocean circulation

and vice versa.

Studies by Gentilli (1972b), Godfrey and Ridgway (1985), Hirst and Godfrey (1993) and Thompson (1984) have suggested that the LC may be sourced from the IT, driven by the meridional gradient, set up by the tropical Pacific waters. The warm, low density IT and SEC water set up an alongshore gradient, with higher steric height at 22^oS (North West Shelf) compared to the cooler, higher density Southern Ocean water 35^oS (Cape Leeuwin). It is for this reason when analysing Indian Ocean data, that the global climate state must be taken into account.

Currently there is no conclusive link between LC and ENSO patterns, however linkages between the IT and ENSO, and the IT and LC ensure this is likely. Linkages between ENSO and LC flow may be simple, with El Niño years indicating weaker LC flows and La Niña years indicating extended periods of strengthened LC flow (Cresswell *et al.*, 1989; Phillips *et al.*, 1991). The effect of this link, indicated by the flow of warm water across to western borders of the Pacific Ocean, is attributable to changing windstress patterns. A strong link between years of strong LC flow and a corresponding La Niña situation may be likely, with the western flow (responding to strengthened south-easterly trades) contributing to the IT, feeding the LCS area (off the North West Shelf), intensifying the pressure gradient driving LC flow (Pearce, 1991). These links may extend to inner-shelf flows, years of extended or intense LC flow (La Niña) suppressing upwellings, the LC extending onto the inner-shelf region, reducing equatorward currents.

Table 2.1 indicates the ENSO situation during the key periods of current analysis.

When reflecting on the history of studies of Western Australian regional oceanography, with specific interest to the key studies indicated, it becomes clear that the global climate pattern may have greatly affected results of studies in the region. With a possible underestimation of LC flows during El Niño events, and weaker inner-shelf flows observed

Year	State	SOI (±)	Year Max	Year Min	Author
1951	El Niño	3/9	January, 16.5	July, -8.2	Rochford
1952		5/7	June, 7.4	December, -12.6	Rochford
1953		1/11	January, 2.2	May, -31.9	Rochford
1954	La Niña	9/3	December, 12.8	February, -3.6	Rochford
1955	La Niña	10/2	July, 19.2	January, -5.4	Rochford
1956	La Niña	12/0	October, 18.3	September, 0.2	Rochford
1957	El Niño	3/9	January, 5.6	May, -12.2	Rochford
1958		4/8	August, 7.8	January, -16.8	
1959		7/5	March, 8.4	February, -14.0	
1960		9/3	April, 7.8	June, -2.3	
1961		8/4	December, 13.8	March, -20.9	
1962		10/2	January, 17.0	March, -1.4	
1963	El Niño	5/7	January, 9.4	October, -12.9	
1964	La Niña	9/3	August, 14.3	January, -4.0	
1965	El Niño	3/9	March, 2.9	July, -22.6	Hamon
1966		2/10	August, 4.0	March, -13.9	Hamon
1967	La Niña	7/5	January, 14.6	December, -5.5	Hamon
1968		7/5	May, 14.7	November, -3.4	Hamon
1969	El Niño	2/10	December, 3.7	January, -13.5	Hamon
1970	La Niña	4/8	November, 19.7	January, -10.1	
1971	La Niña	12/0	April, 22.6	July, 1.6	
1972	El Niño	3/9	March, 8.2	July, -18.6	
1973	La Niña	9/3	November, 31.6	February, -13.5	
1974		10/2	January, 20.8	November, -1.4	
1975	La Niña	11/1	September, 22.5	January, -4.9	
1976	El Niño	8/4	February, 12.9	July, 12.8	
1977		1/11	February, 7.7	June, -17.7	
1978		5/7	May, 16.3	February, -24.4	
1979		4/8	February, 6.7	July, -8.2	
1980		3/9	January, 3.2	April, -12.9	
1981		8/4	June, 11.5	March, -16.6	
1982	El Niño	3/9	January, 9.4	November, -31.1	Thompson
1983		5/7	September, 9.9	February, -33.3	
1984		7/5	February, 5.8	June, -8.7	
1985		6/6	April, 14.4	June, -9.6	
1986	El Niño	5/7	June, 10.7	November, -13.9	LUCIE
1987	El Niño	0/12	November, -1.4	April, -24.4	LUCIE, Capes Current
1988	La Niña	8/4	November, 21.0	February, -5.0	
1989		9/3	April, 21.0	August, -6.3	
1990		4/8	May, 13.1	February, -17.3	
1991	El Niño	2/10	January, 5.1	May, -19.3	
1992		3/9	August, 1.4	January, -25.4	Capes Current
1993		2/10	December, 1.6	April, -21.1	Capes Current
1994		1/11	February, 0.6	April, -22.8	Capes Current
1995		5/7	July, 4.2	April, -16.2	
1996		11/1	June, 13.9	November, -0.1	Inner-Shelf
1997	El Niño	2/10	February, 13.3	June, -24.1	
1998	La Niña	8/4	July, 14.6	March, -28.5	
1999	La Niña	11/1	April, 18.5	September, -0.4	
2000		10/2	November, 22.4	June, -5.5	
2001		7/5	February, 11.9	December, -9.1	
2002		2/7 (9 values)	February, 7.7	August, -14.6	

Table 2.1: Southern Oscillation Index - Calculated values from 1951 - 2002 *(from Bureau of Meteorology, 2002)* and corresponding Authors

during La Niña conditions.

Data obtained during the LUCIE study was representative of an El Niño cycle, and for this reason may have indicated reduced LC flows. Alternatively, data obtained from *RV Franklin* 1996 cruises, was collected during a La Niña cycle, possibly indicating weaker than usual equatorward inner-shelf flows. It is possible then that present knowledge of LC and inner-shelf flows (based on the key LUCIE and corresponding datasets) is greatly underestimated, with significantly higher transports, duration of flow and persistence a distinct possibility.

2.5.2 The Indian Ocean Dipole

The Indian Ocean dipole (IOD) is an effect not unlike the ENSO situation in the tropical Pacific Ocean. The atmosphere-ocean interaction accounts for about 12% of SST variability in the Indian Ocean (Saji *et al.*, 1999), replicating the rainfall variation that ENSO affects. A positive event, causing severe drought in Indonesia and corresponding rainfall in eastern Africa during active years, with associated cool (Sumatra) and warm water pools (Africa) is associated with this atmospheric phenomenon.

The active condition is dependent on SST's off the western (central) basin (Africa - south of Madagascar) and the area south of Sumatra (Australia), with corresponding warmer than usual SST's over the western basin and cooler SST's off Sumatra. Equatorial surface winds (trade winds) normally blowing from the east, weaken and reverse direction during an active phase. The positive phase produces above-normal rainfall in regions of south-central Africa. The cooling SST is caused by increased evaporation drawing latent heat from the eastern Indian Ocean, and is associated with stronger winds along the eastern boundary of the sub-tropical high, which strengthens and shifts to the south during a positive event. The opposite occurs in the western waters (Behera and Yamagata, 2001).

An inactive condition is expressed through 'normal' conditions, with warmer SST's off Sumatra (Australia), and cooler SST's experienced in the western basin.

The IOD and the circulation patterns that are present within the Indian Ocean appear to operate independently to the ENSO state of the Pacific (Anderson, 1999; Saji *et al.*, 1999; Tourre and White, 1997; Webster *et al.*, 1999), supported by the SST analysis of Behera and Yamagata (2001) and Behera *et al.* (2000) linking with the austral summer. Allan *et al.* (2001) undertook a reassessment of this work and the earlier work of Nicholls (1989), indicating the apparent ENSO independence disappeared when seasonally stratified data was used. The most recent work by Yamagata *et al.* (2002) indicated that the IOD influences the SOI, consequently forcing ENSO. Such a result suggests the IOD is a more dominant component of global climate.

It is uncertain what effect the IOD has on Western Australian regional oceanography. This mode is intrinsically coupled to rainfall and atmospheric circulation, and has been linked to the subsurface 'memory' of the Indian Ocean. It is likely Indian Ocean THC controls the development of IOD events, with a study by Rao *et al.* (2002) indicating that a subsurface mode corresponds closely with the surface IOD.

2.5.3 Madden-Julian Oscillation

Madden and Julian (1971) discovered an equatorial atmospheric oscillation over the Indian Ocean, extending to the eastern Pacific, linked with the predictability of the tropical Asian monsoons and encompassing the entire troposphere. They indicated that the oscillation is most likely a manifestation of a large (1000's km width) circulation cell oriented in a zonal plane along the Equator.

The Madden-Julian Oscillation (MJO) affects the entire tropical troposphere but is most evident in the Indian and western Pacific Oceans. It refers to the equivalent ENSO

situation in the Indian Ocean with monsoonal oscillations based around a 30 - 60 or 40 - 50 day period, the most prominent circulation governing climate over the tropics (Geerts and Wheeler, 2001) The MJO involves variations in wind, SST, cloudiness, and rainfall. Associated with the propagation of convective anomalies, the MJO involves variations in the global circulation. The MJO affects the intensity and break periods of the Asian and Australian monsoons and interacts with El Niño, possibly effecting this cycle, forcing the IT, and as a consequence Western Australian regional oceanography.

Madden and Julian (1994) undertook a review of work related to the MJO and concluded that there was a significant link between this atmospheric oscillation and windstress, altering surface currents. Work highlighted in their 1994 review indicated that this effect was experienced on 30 - 60 and 40 - 55 day timescales, stretching from Madagascar (47^oE - Western Indian Ocean) to Callao, Peru (90^oW - Eastern Pacific Ocean).

2.6 Global Climate Modelling

Any climate model is an attempt to simulate the many dynamic processes that combine to produce climate. When creating a model, it is important to understand these separate processes, and then, using basic physical, chemical and biological principles, attempt to recreate these linkages. The outcome is a simulation that can predict changes and interactions, a simplification of the real world (McGuffie and Henderson-Sellers, 1999).

Atmosphere-Ocean General Climate Models (AOGCM's) were developed throughout the early 1990's, with dramatic increases in resolution and increased component modelling due to the exponential growth of computing power (Houghton *et al.*, 2001; McGuffie and Henderson-Sellers, 1999). AOGCM's have been developed to provide an insight into the dynamic and non-linear processes that occur within the atmosphere and oceans. The intrinsically linked nature of these systems ensures that a myriad of complex processes are

occurring simultaneously, with each change altering atmosphere and oceanic states and leading to dramatic changes in global climate.

Many studies have reviewed the accuracy of AOGCM outputs in relation to SST's, MSLP and precipitation. Frederiksen *et al.* (1999) indicated even early AGCM's (Bureau of Meteorology Research Centre [BMRC] Climate model [Version 2.1, first released in the early 1990's] and the first version of the Hadley Centre climate model [HADAM1]), confirmed linkages between Pacific SST's and Australian rainfall, however, with varying success. These models ran at resolutions far coarser when compared to current AOGCM's, however were still providing reasonably good representation of observed conditions.

The latest IPCC report (the Third Assessment Report [TAR] Houghton *et al.*, 2001) indicate AOGCM's are predicting small decreases in precipitation, with an inconsistent magnitude of warming compared to the calculated global mean for southern Australia and corresponding greater than average summer warming for northern Australia. No model predicts a cooling scenario, when compared to current values. Globally averaged surface temperatures are projected to increase by 1.4 - 5.8^oC 1990 to 2100. The convincing nature of these results, when related to recent observations (indicating significant increases to global-mean temperatures), supports the concept of a changing climate; most models agreeing well with decreased rainfall, and all projecting increased surface temperature (Houghton *et al.*, 2001).

2.6.1 Greenhouse Gases

Greenhouse gases (GHG), such as water vapour and carbon dioxide act to increase atmospheric temperatures. A positive feedback loop is apparent with water vapour, with outgoing longwave radiation (OLR) absorbed by this species, increasing atmospheric temperatures, leading to greater evaporation of water, continuing this cycle.

Carbon dioxide is the second most prolific GHG species after water vapour. This species is produced chiefly by industrialised processes and fossil fuel burning. This gas acts in conjunction with water vapour, trapping OLR and increasing global temperatures. A study of CO_2 concentrations by Enting (1999) indicates that since at least 1955 there has been an exponential increase in atmospheric CO_2 concentration (taken from Mauna Loa, Hawaii). This agrees well with the current mean value for 2001 (370.9 *ppmv* - CDIAC, 2002).

Carbon dioxide is readily absorbed by global oceans, however, increased warming of the global atmosphere and oceans reduces CO_2 solubility, leading to a positive feedback loop, driving increased temperatures. Similarly, reduction (or total collapse) of the global THC, predicted by some climate models, is a response to increased CO_2 forcing resulting in a more stratified global ocean. This is predicted to lead to decreasing transport of sequestered CO_2 transported and stored in the deep ocean, again a positive feedback leading to increased atmospheric and ocean heating (Matear and Hirst, 1999). Cai and Gordon (1998) indicated that enhanced high-latitude ocean freshening also acts to decrease the THC transport, with a decrease in the intensity of both the northern hemisphere NADWF and the southern hemisphere AABWF. Bi *et al.* (2001) support this conclusion, indicating that by the time CO_2 forcing reaches triple current values, the AABWF essentially ceases, with corresponding substantial declines in the NADWF.

2.6.2 CSIRO - Global Climate Models

The Commonwealth Scientific and Industrial Research Organisation (CSIRO) Division of Atmospheric Research (DAR) has been involved in the development of AOGCM's for over 20 years. The CSIRO Mark 3 AOGCM was developed to remove the element of climate drift from the Mark 2 model. This climate drift was corrected by the use of flux

adjustments, however these corrections are un-physical and it is undesirable for a coupled AOGCM to utilise such corrections. Improvements to the physical parameterisations have been undertaken to correct this climate drift and a marked increase in model resolution has also been achieved.

This model consists of two components, the Oceanographic General Circulation Model (OGCM) and the Atmospheric General Circulation Model (AGCM). The components run together as the coupled model (AOGCM).

The AGCM is primarily an extensively upgraded version of the Mark 2 model. Mark 3 has the option of being run in two horizontal resolutions (spectral R21 (5.625^oEW x 3.1^oNS) and spectral T63 (1.875^oEW x 1.875^oNS)). Vertical resolution for the Mark 3 has been set at 18 vertical levels (T63). The spectral model now also contains a Semi-Lagarangian Transport (SLT) method for the moisture components (Gordon *et al.*, 2002).

The OGCM is based on the GFDL MOM version 2.2 code by Pacanowski and Griffies (2000). It has been specifically designed to complement and match (with an identical horizontal land-sea grid) the Mark 3 AGCM (incorporating 1.875^oEW resolution). An enhancement to the meridional resolution was developed to incorporate adequate representation of El Niño features, achieved by increasing resolution to double that of the AGCM (1.875^oEW x 0.9375^oNS). Resolution is termed spectral T63_2, indicating there are 2 horizontal ocean grid points for each of the atmospheric points in the coupled configuration. The (T62_2) OGCM has 31 vertical levels, extending from 5 m below the sea surface to 4800 m at maximum depth (Gordon *et al.*, 2002). The coupled Mark 3 version of the model can only then be run at the T63 resolution (T63 - AGCM and T63_2 - OGCM). A 'slab' ocean model can alternatively be incorporated.

2.6.2.1 Performance of CSIRO AOGCM's

Houghton *et al.* (2001) indicate through the TAR that the CSIRO Mark 2 model expressed median values when compared to other models in the IPCC summary. The Mark 2 model utilised heat, freshwater and momentum flux adjustments. The use of these adjustments lead to a very good replication of ocean climatologies when compared to other models incorporated in the TAR.

The Mark 2 model faired well when comparison was made to diagnostics of ocean circulation between the 27 control runs of corresponding models. When relating to heat transport for the Indo-Pacific region, the Mark 2 model was the closest to observed values of 1.34 PW with 1.31 PW. Similarly, a value of 103 Sv was expressed for ACC transport, the Mark 2 model providing the second best replication of 123 Sv observed. Mark 2 modelled precipitation values also indicated the closest replication to the mean of 18 models analysed, indicating that this model is a good single-model mean representation for the TAR (Houghton *et al.*, 2001). It is expected that the Mark 3 model will then express similar replication to its predecessor, and that values contained in this review, indicate representative values for future IPCC reports.

The source code, from which the ocean model is chiefly comprised, is based on the GFDL MOM version 2.2 (Gordon *et al.*, 2002). The MOM code is the basis of the bulk of the prominent IPCC OGCM component models. Models utilising this code include; CSIRO, HadCM3, GFDL, CCC, NCAR and PCM and for this reason, it is fair to assume that these models (aside from differences to resolution and the boundary-layer interface) would replicate oceanography almost identically. The ECHAM4 (Germany) and IPSL (Institut Pierre-Simon Laplace) models do not utilise MOM code, instead using the OPYC3 (isopyncal model - Max-Planck-Institute for Meteorology, Germany) and OPA (Laboratoire d'Oceanographie Dynamique et Climatologie) models respectively. It appears that

language has been the significant factor in the selection of the coupled OGCM code (Dr Tony Hirst *Pers. Comm.* CSIRO - DAR, 21-10-02)

CHAPTER 3
METHODOLOGY

Output from the CSIRO Mark 3 Coupled Atmosphere-Ocean General Climate Model (AOGCM) was analysed and visualised using Matlab. 10-year mean model outputs were reviewed for datasets simulating the IPCC A2 scenario, the worst-case GHG scenario, with prediction for a doubling of the world population and corresponding doubling of atmospheric carbon dioxide by the year 2100 (Houghton *et al.*, 2001). Corresponding control scenarios modelling a world with constant carbon dioxide forcing (no change when related to current values) were also analysed.

5 datasets were available for analysis in this project. 3 outputs simulating the A2 scenario; 1991-2000, 2061-2070 and 2091-2100 (hereafter A2000, A2070 and A2100 respectively), and control scenario outputs for the years 1991-2000 and 2061-2070 (hereafter C2000 and C2070) with atmospheric output only for 2091-2100 (C2100).

3.1 Output Variables

Ocean model resolution is 0.93^o and 1.875^o for latitude and longitude respectively, with staggered (0.466^o and 0.9375^o - latitude and longitude) grids for scalar to vector output respectively (Gordon *et al.*, 2002). This study reviews a small sub-grid area of the AOGCM, relating to the regional oceanography of Western Australia. The ocean grid utilised incorporates the area 7.5 - 42.5^oS latitude and 101 - 122^oE, with 38 latitudinal (zonal) gridpoints and 12 longitudinal (meridional) gridpoints. The depth-grid includes 31 vertical levels, extending from 5 - 4800 m, with 15 of these levels above 500 m depth. The corresponding atmospheric grid incorporates 6.5 - 44^oS latitude and 99 - 124^oE longitude, with 21 latitudinal (zonal) gridpoints and 14 longitudinal (meridional) gridpoints. Reso-

lution of the atmospheric grid is 1.865^o and 1.875^o for latitude and longitude respectively, with only surface pressures utilised.

3.1.1 Scalar Quantities

These variables were all contoured - allowing a comparison between each of the grid zones with corresponding isotherms (temperature), isohalines (salinity) and isopycnals (density) and regions of similar fluxes for both surface heat and freshwater fluxes.

3.1.2 Vectoral Quantities

These variables were all plotted employing Eulerian visualisation. Each grid point was then analysed independent of the neighbouring grid point, vectoral arrows indicating velocity (speed and direction) for each individual data point.

3.2 Assumptions

In order to calculate variables relating to the model output a series of assumptions have been made relating to physical quantities of the Earth and the model construction. Such assumptions (incorporated in the area and transport calculations) include; a mean equatorial radius of 6,378.136 km, and the ocean model, utilising a cartesian grid, incorporates no change to volume as depth increases. The radius assumption ensures calculated horizontal distances between grid points are representative of Earth surface values only. Real-Earth grid-distance values will decrease as distance from the Earth core decreases (depth increases). The maximum error associated with this assumption is 0.01% at 4800 m depth. Due to the bulk of calculations corresponding to the top $\sim$400 m or above, this error is negligible.

Similarly, to compare 'current' values with that of the model predicted values, assumptions were made relating to the current state of climate and tropospheric GHG concen-

tration. The most current (2001 - year mean) values for CO_2 tropospheric concentrations collected at Mauna Loa Observatory, Hawaii, indicate values of 370.9 *ppmv* (CDIAC, 2002), corresponding closely with the IPCC predictions for 2002 (Houghton *et al.*, 2001). The nature of the IPCC predictions indicates a fairly constant increase in CO_2 concentrations until the year 2030, when the individual scenarios start to take affect. These then indicate values of ∼620 *ppmv* or a 67% increase corresponding to A2070 and ∼850 *ppmv* or a 129% increase for A2100 relative to present values (the A2 scenario).

3.2.1 Temperature

Corresponding to the output of the model, potential temperature (Θ) has been plotted, hereafter termed temperature (T). The difference between these variables can be summarised as follows, due to the slightly compressible nature of seawater, a sample brought to the surface from depth will expand and therefore cool. The temperature of a sample brought to the surface adiabatically (without thermal contact with surrounding water) will therefore be warmer than *in situ*. The temperature that this parcel would have at the surface in these circumstances is called the potential temperature (Θ).

$$T_{in\ situ} = \Theta + \int_{P_a}^{P} T dp = \Theta + \Sigma_i \Sigma_j \Sigma_k A_{ijk}\ P^t (S - 35)^j T^k \tag{3.1}$$

where T is the *in situ* temperature in ^oC, Θ is the potential temperature of seawater, S is (practical) salinity in *ppt* and P is oceanographic pressure in dbar (Bryden, 1973).

Potential temperature (Θ) accounts for the additional heat stored due to compression of seawater at depth. For this reason Sea Surface Temperature$_\Theta$(SST - uncompressed surface water) values replicate temperature (T). Θ values to 400 db (m) depth closely represent T, an error less than 0.35% apparent at 35 *ppt* (Tomczak, 2000).

3.2.2 Density

This variable was calculated from the seawater toolbox (Morgan, 2002), the formula derived from Millero *et al.*(1980). Density (ρ) can be calculated from the UNESCO formula:

$$\rho(T, S, P) = \rho(T, S, 0)/[1 - P/K(T, S, P)] \tag{3.2}$$

where ρ is the density of seawater in kg/m^3, T is the temperature in ^oC, S is the salinity in *ppt* (or *psu*), P is level pressure (due to depth) and $K(S, T, P)$ is the secant bulk modulus. The use of potential temperature (Θ) in the calculation specifies potential density (σ_Θ) is calculated for the dataset, hereafter is termed 'density' (σ_Θ).

3.2.3 Geopotential Anomaly

Geopotential anomaly was calculated from the seawater toolbox, using the formula expressed in equation 3.3 (Morgan, 2002).

The geopotential equation (Pond and Pickard, 1983).

$$\begin{aligned} \phi_2 - \phi_1 = g(z_2 - z_1) &= \textstyle\int_1^2 \alpha_{35,0,p} dp &- \textstyle\int_1^2 \delta dp \\ &= -\Delta\Phi_{std} &- \Delta\Phi \end{aligned} \tag{3.3}$$

where (ϕ_2 - ϕ_1) is the geopotential difference ($\Delta\Phi$) between levels z_2 and z_1 where the pressure will be p_2 and p_1 for each comparative level and g is gravity (9.8 m s^{-1}). The first quantity on the right of the equation (3.3) is called the '*standard* geopotential distance' ($\Delta\Phi_{std}$, a function of p only), while the second is called the 'geopotential *anomaly*' ($\Delta\Phi$, a function of S, T and p)(Pond and Pickard, 1983).

This calculation requires the variables temperature (T), salinity (S) and the sample pressure (p) value determined by depth, values are calculated in reference to the surface pressure (p_a).

This calculation determines the steric height for the depth 285 m (level 12) referenced

against the surface. The calculation of the pressure field at this depth involves a vertical integration of density (σ_Θ). The output of this file determines m^2 s^{-2}, and therefore to determine steric height, dividing this value by gravity (g) indicates a steric height in metres.

Use of geostrophic methods for calculating currents and geopotential (dynamic) heights has some inherent problems, which include: the calculation assumes a level of no motion at the reference depth, in this case ~285 m; and that baroclinic effects (gravity induced flow due to density differences) are nil (Pond and Pickard, 1983). These assumptions are possible sources of inaccuracy in the dataset, as the A2000 ~285 m plot indicates a mean flow of 0.5 cm s^{-1} west of Shark Bay (26.5$^o S$) and a 0.8 σ_Θ difference at 285 m depth (from the density calculation).

Benny and Mizuno (2000) calculated the annual steric height of the Indian Ocean from the thermal field and temperature-salinity (T-S) data. These values were calculated from the Levitus82 dataset, obtained from shipborne; bathythermograph (BT), expendable bathythermography (XBT), conductivity temperature depth (CTD), salinity temperature depth (STD) and Nansen cast collections. The very nature of oceanographic research would ensure that swell, seas and sub-surface internal wave motion were included in this data collection, and it is unlikely that conditions specified as assumptions for the geostrophic equation would be completely satisfied in this example. Comparative conditions are expressed in the model output. For this reason model values will correspond to Benny and Mizuno (2000).

3.2.4 Transports

A calculation of volume of the zonal grid (distance between latitude points) and meridional grid (distance between longitude points) is required to determine transport and heat transport - these values correspond to distance between consecutive latitude points

and longitude values for the zonal and meridional grids respectively. Horizontal (Earth-surface) distances were calculated from the M_map toolbox (Pawlowicz, 2002).

Transport area is then a multiplication of these surface (zonal and meridional) distances by the depth grid:

$$Tp_a = \Delta x \Delta z \tag{3.4}$$

where Tp_a is the transport area through which currents flow, Δx the horizontal grid spacing (either zonal or meridional) and Δz the vertical grid spacing (depth).

For this calculation the following assumptions were made: velocity components for each level are mean values for the corresponding vertical area; and temperature values indicate mean temperature for each model level 'box'.

Transports were calculated utilising both zonal (u) and meridional (v) current velocities. Combined velocities (both u and v) were calculated and integrated over depth for the Indonesian throughflow (IT), South Equatorial Current (SEC), Indian Ocean Central Water (IOCW) and meridional (alongshore) components only for the Leeuwin Current Source region (LCS). Integrated values relate from the surface to a depth of ∼400 m (level 14) for the IT and SEC, in reference to literature on these transports, and ∼160 m (level 9) for the IOCW, with LCS value indicating a calculation to just 285 m (level 12), the depth extent of the LC (300 m - Church *et al.*, 1989; Cresswell and Golding, 1980; Cresswell and Peterson, 1993; Smith *et al.*, 1991) .

Figure 3.1 indicates the grid location for each of the transport calculations.

Transports are then:

$$Tp = Tp_a V \tag{3.5}$$

where Tp is transport in Sv, Tp_a is the area through which currents flow and V is

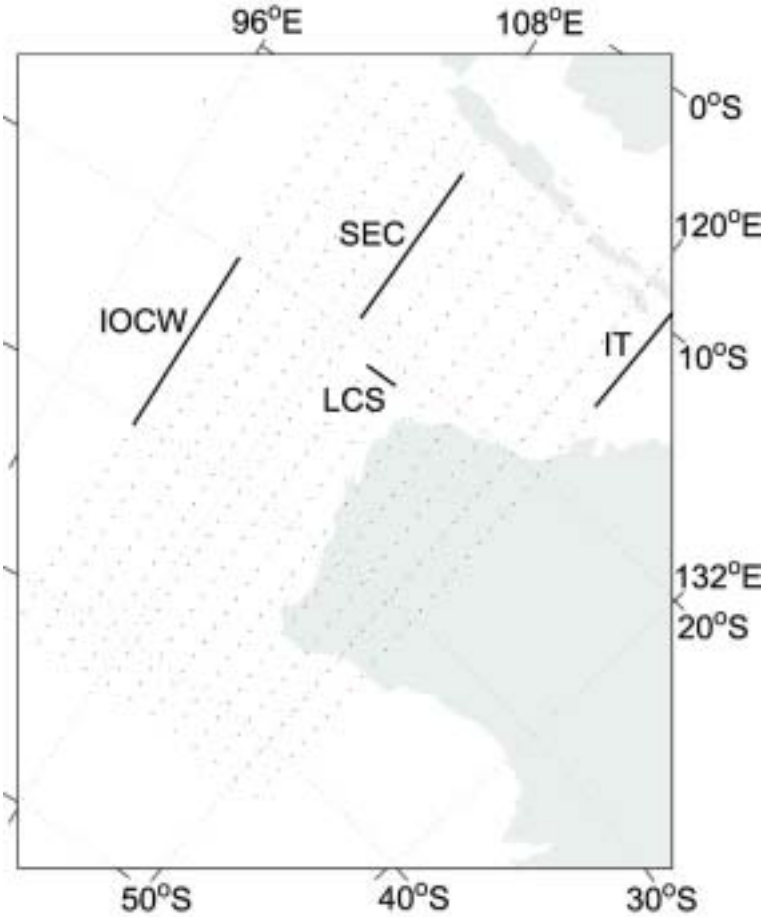

Figure 3.1: Vectoral grid with transport locations annotated. Current acronyms are included in Appendix A

the combined (u and v components) current velocity for this area.

Heat transport is based on the transport calculation of volume for the zonal and meridional grid. Datapoints then indicate mean values for each of the vertical 'boxes' of the ocean. To convert temperature to (heat) energy, specific heat capacity is required. The seawater package is utilised to obtain this value, calculated from *in situ* salinity (S), (potential) temperature (Θ) and level pressure (p).

Heat flux is then calculated by:

$$Tp_h = ETp \tag{3.6}$$

where Tp_h is the heat transport, E is the heat energy of the level for which the transport is calculated and Tp is the transport in Sv.

3.3 Data

Oceanographic output was primarily utilised for this study. The CSIRO model, with increased resolution when compared to the previous Mark 2 model, is very successful at resolving current Western Australia regional oceanography. The source code, from which this model is chiefly comprised, is based on the Geophysical Fluid Dynamics Laboratory (GFDL) Modular Ocean Model (MOM - version 2.2)(Gordon *et al.*, 2002). Model output was compared to the Lamont Doherty Earth Observatory - Levitus94 World Ocean Atlas database (Levitus94 Annual, 2002).

The nature of the AOGCM ensures that a mass balance is attained during spin-up, with a return to surface climatologies (SST and surface currents) prior to commencement of the coupling. The Levitus94 data is a collection of isolated values, then infilled to provide global coverage. These values, were obtained from various sources (the first in 1944, intensifying in 1958, with thorough coverage between Fremantle and Indonesia since

this time). A considerable amount of station data for this region was provided by CSIRO Marine and incorporated into the following World Ocean Database 1998 (Levitus *et al.*, 1998).

A2000 dataset visualisation indicated a successful replication of present oceanography, with temperature and current regimes closely resembling Levitus94 and documented climatologies. It is likely that the model may better represent real ocean climates, as the model is mass-balanced, whereas the nature of the Levitus94 dataset ensures that single point measurements, infilled, only indicate snap-shots for oceanography, possibly due to 'prime' seasonal sampling regimes. The nature of the 10-yr mean data however does not allow for replication of current speeds, these being greatly underestimated, due to integration of opposing seasonal patterns.

3.3.1 Currents

Key currents are qualitatively resolved extremely well in this oceanographic model. Figure 3.2 summarises the observed regional oceanography of Western Australia.

Figure 3.3 (based on the A2000 dataset) replicates a typical surface regional flow pattern (at 15 m depth), with the SEC flowing strongly. A mean flow speed of ∼20 cm s^{-1} is indicated for this current, peaking at ∼35 cm s^{-1} in the Timor Sea. The SEC appears to dominate the top ∼200 m of regional oceanography, with peak flows centred at 12.6^oS (101^oE), broadening from east to west. Between ∼100 and ∼160 m there is a strong interaction between this flow and the simulated Leeuwin Undercurrent (LUC) at 15^oS. This figure also represents a poleward flow that may be replicating a Leeuwin-like current, with a mean speed of ∼5 cm s^{-1}. The eastward flow at 36^oS (just below Cape Leeuwin [CL]) also replicates the strong flow of the Leeuwin Current (LC) and IOCW around the southern capes into the Great Australian Bight, with mean values of ∼10 cm

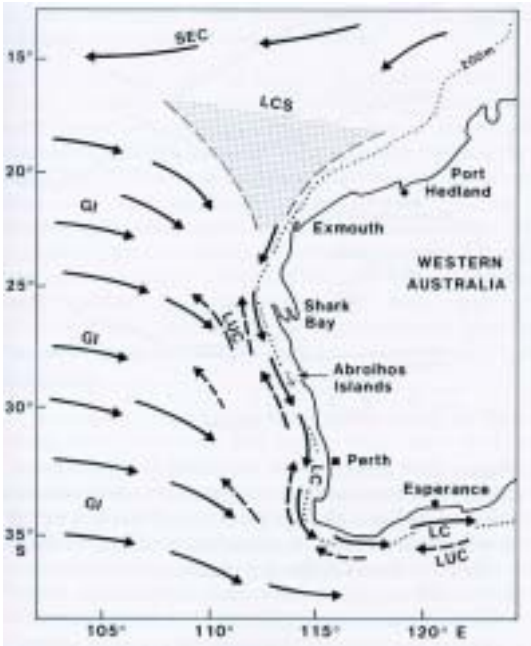

Figure 3.2: Schematic diagram of regional Western Australian oceanography. Current acronyms are included in Appendix A. Solid arrows are surface currents, dashed are subsurface. The dotted line shows the 200m contour *(from Pearce, 1991)*

s^{-1} supporting this conclusion. Church *et al.* (1989) have recorded flows of 1.8 m s^{-1} at this location. However, with seasonal elements averaged in the A2000 dataset, such high values would not be expected.

Transport calculations indicate that the poleward flow is not resolved for completely by the Leeuwin source region. The IOCW (geostrophic) inflow therefore is accounting for ~4.7 Sv of the alongshore transport. Transport calculated for the LCS indicates a value of 0.2 Sv, this value clearly not representing observed LCS values (4 Sv - observed during May, peak period of LC flow, Thompson, 1984). A current reversal occurring at ~128 m (level 8), continuing to becoming part of the LUC, agrees well with ship-board observations of Thompson (1984). Qualitatively then, the model is representing well for this flow (if not the processes [source area] that drive the LC). It is likely that the 10-year mean dataset, with seasonal elements averaged, will underestimate the transport of the LCS. Observed values between 2 Sv (summer) and 5 Sv (winter) (Smith *et al.*, 1991), 6.5 Sv (34^oS) and

3.4 Sv (35^oS) (Cresswell and Peterson, 1993) and 7 Sv off the North West Shelf (Holloway, 1995) have been documented. Model representation of this flow indicates a value of 4.9 Sv (22 - 36^oS), underestimating observed values. These features relate well with figure 3.2 and present knowledge relating to these flows.

Figure 3.4 replicates the current pattern persistent at 60 m depth. A strong SEC flow with a mean speed of ~20 cm s^{-1} is represented, with similar flow to the surface plot in the Timor Sea. This plot also shows a strengthening IOCW inflow, with mean speeds of ~5 cm s^{-1}. The IOCW intrusion is first apparent at a depth of ~30 m and centred around latitude 27^oS. Andrews (1977) named this inflow the West Australian Current (WAC) and indicated a flow width of 100 - 200 km and depth penetration to 370 m. A flux value of 10 Sv and mean equatorward velocity of 0.5 m s^{-1} (peak velocities of 1.5 m s^{-1}) are associated with this flow (Andrews, 1977).

Figure 3.5 visualises the model currents at 406 m depth. This figure also closely replicates present oceanography, with a prominent LUC, with mean flow speeds of ~5 cm s^{-1} and a peak flow of ~7 cm s^{-1} west of Cape Leeuwin. Observed peak flows of 0.3 m s^{-1} have been recorded by Cresswell and Peterson (1993) at 400 m depth, with Thompson indicating values of 0.4 m s^{-1} at 300 m (and 5 Sv total equatorward transport). The flow appears at 18^oS (101^oE) and ~160 m depth. The representative LUC extends through the profile south to ~1500 m centred around 36^oS, in accord with the observations of Thompson (1984), indicating the flow then continues into the interior of the Indian Ocean.

3.3.2 Temperature

Comparative surface temperature profiles are represented in figures 3.6 and 3.7. It is clear from these figures that the surface temperatures (for the A2000 dataset - 3.6) closely represent near-current oceanic temperatures (Levitus94 - 3.7).

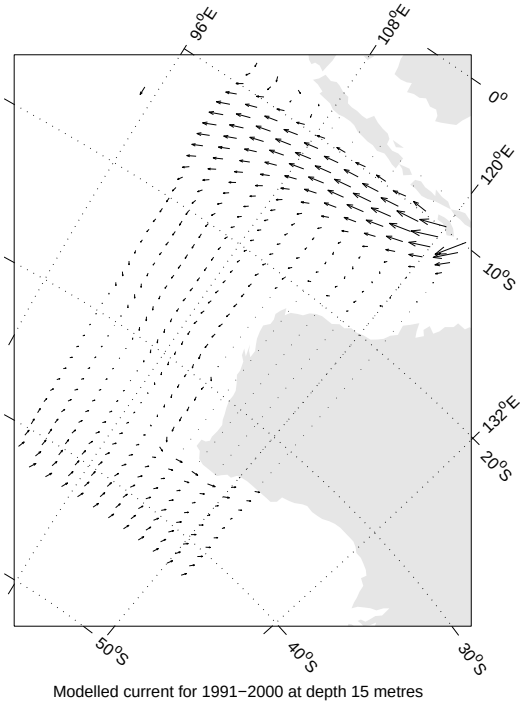

Figure 3.3: Modelled 10-yr mean currents for A2000 at 15 m depth (Scale arrows represent 10 cm s^{-1})

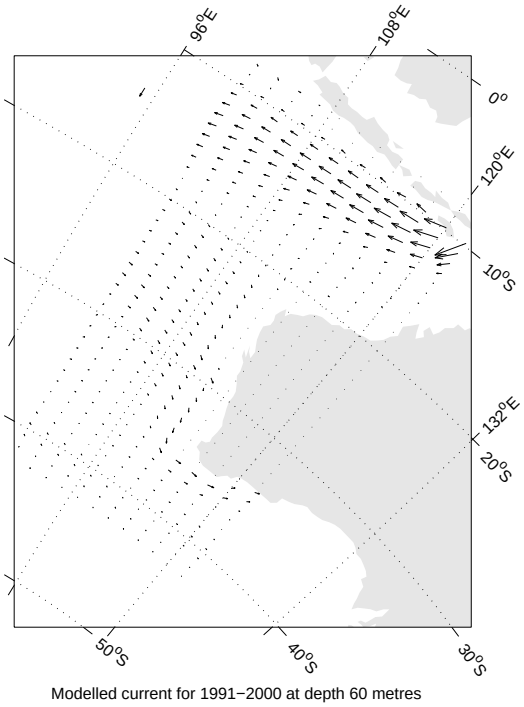

Figure 3.4: Modelled 10-yr mean currents for A2000 at 60 m depth

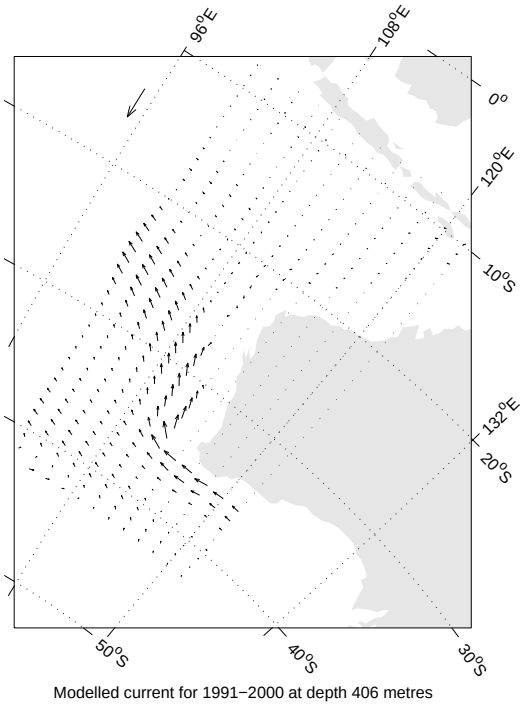

Figure 3.5: Modelled 10-yr mean currents for A2000 at 406 m depth

A2000 output underestimates inshore SST, with a less prominent southern isotherm extension when comparison is made to the Levitus94 plot (figure 3.6 and 3.7 respectively). This is clear, when relating to the IOCW temperature values with equatorward isotherm drift indicating lower temperatures. The underestimation is more marked in the IOCW region (102^oE), with the replication of LC-like temperatures indicating a more realistic inshore profile. The A2000 dataset seems to more prominently visualise the role of the LC, with a marked poleward migration of isotherms as they move towards land (110 - 114^oE). The underestimation of temperature accords with current plots, indicating the presence of a LC-like flow. Both model variables indicate a less dominant LC compared to observed field values. The probable reason for this, is linked to model resolution not completely resolving for the LC. The LC's mean width (ignoring eddies) of ∼100 km (Church *et al*, 1989), is half that of the model ∼200 km zonal resolution.

Depth profile plots of ocean temperature show a similar picture, with figures 3.8 and

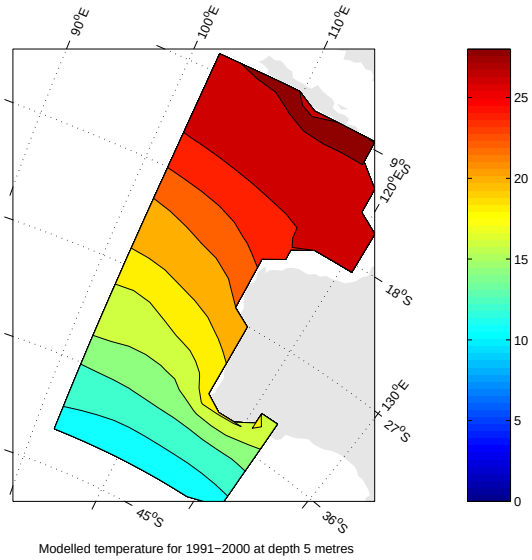

Figure 3.6: Modelled 10-yr mean temperature for A2000 at 5 m depth

3.9 representing the closest complete transect to the shore (113^oE). These plots indicate the model dataset closely resembling Levitus94, with a slight equatorward bias to the extension of the warmer water (similar to surface plots). A sub-surface extension of warmer water at 32^oS is present in the A2000 plot, conflicting with Levitus94 values, however warm water intrusion is underestimated in the northern sector (15 - 25^oS) for A2000. For this reason it appears that the model is replicating the dominance of the LC flow with slight underestimation at the surface, and an exaggeration in the southern sub-surface (25 - 35^oS).

When temperature profiles are related to resolved current flows (see figures 3.3, 3.4 and 3.5), with specific interest to LC flow, these indicate current features are well represented, however grid resolution does not allow for accurate replication of LC flow. This comment is supported by calculated transports relating to this flow, also indicating less than observed values (Cresswell and Peterson, 1993; Holloway, 1995; Smith *et al.*, 1991; Thompson, 1984).

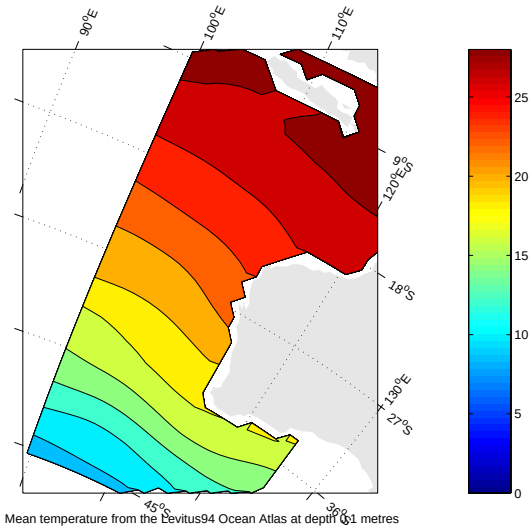

Figure 3.7: Observed mean surface temperature *(from Levitus94 Annual, 2002)*

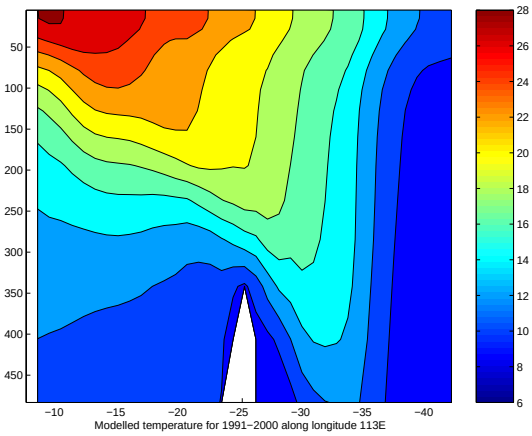

Figure 3.8: Modelled 10-yr mean temperature profile along 113^oE for A2000

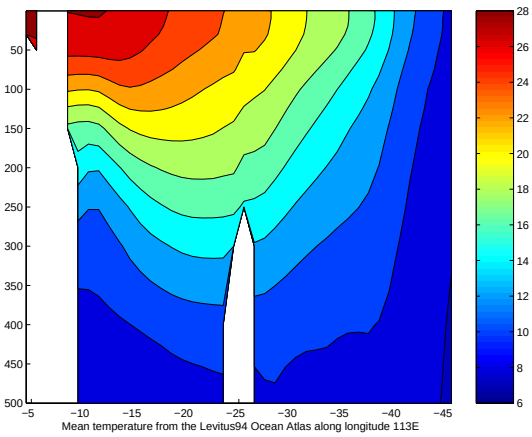

Figure 3.9: Observed mean temperature profile along 113^oE *(from Levitus94 Annual, 2002)*

3.3.3 Salinity

Salinity profiles are not as convincing as the temperature and current plots, with questionable representation of the near-current values when compared to the Levitus94 Ocean atlas.

Comparative surface salinity profiles are represented in figures 3.10 and 3.11. It is clear from these figures that surface salinity (for the A2000 dataset - 3.10) does not closely represent near-current oceanic salinity (Levitus94 - 3.11). The Mark 3 model tends to indicate a decreasing salinity pattern for equatorial to mid-latitudes, of the order 1.0 *ppt* (Gordon *et al.*, 2002). This is likely due to CO_2 forcing, the A2000 dataset corresponding with years 151 - 160 of the model run, enough time for the increased CO_2 forcing to have an effect (Dr Tony Hirst *Pers. Comm.* CSIRO - DAR, 21-10-02).

The salinity profiles show a different picture from the pattern appearing in temperature plots. It is clear, comparing figures 3.10 and 3.11, that the A2000 dataset overestimates the dominance of the SEC flow, the tendency for intrusions from tropical, lower salinity water clearly being visualised in figure 3.10. An underestimation of the salinity and dominance of the IOCW is also apparent. This flow incorporates values of 35.5 *ppt* (Levitus94, figure 3.11), these slightly underestimated in the A2000 dataset with IOCW values of 35 *ppt* indicated. The dominance of this flow is underestimated in the A2000 dataset, with the exaggeration of the SEC flow dominating low latitudes in the A2000 plots. It is clear from surface plots that the A2000 dataset is underestimating salinity by $\sim$0.5 *ppt*, less than the underestimation indicated by Gordon *et al.* (2002). The visualisation of Gordon *et al.* (2002), covering the entire globe, when compared with regional analysis for this study, results in possibly greater ranges. The regional analysis allows for more accurate representation due to smaller scale-changes. The role of the IOCW is visualised in figure 3.10, with this flow extending beneath Cape Leeuwin (35^oS), into the Southern Ocean and

the Great Australian Bight, possibly combining with LC flow at this location (Andrews, 1983, Cresswell and Peterson, 1993).

The nature of this exaggeration becomes more accentuated when looking at the depth-profile plots (figures 3.12, 3.13). The A2000 dataset overestimates the role of the SEC and underestimates IOCW. It is clear from figure 3.12 compared to 3.13 that the SEC is more prevalent, and of a lower salinity when compared to the Levitus94 plots. Values of $\sim$33 *ppt* dominate the A2000 replication of the SEC flow, whereas corresponding salinities of $\sim$34 *ppt* are present at the low latitudes in Levitus94 (indicating a change outside the 0.5 *ppt* model underestimation). The A2000 dataset indicates a dominance of this flow down to 23^oS, whereas the corresponding Levitus94 plot indicates that this low-latitude tropical water is present just to 15^oS. The IOCW is indicated by Levitus94 to flow from 18^oS to 43^oS, whereas the A2000 plots indicate flows from just 26^oS to 37^oS. Maximum values for this flow are grossly underestimated by A2000, with Levitus94 (figure 3.13) indicating values in excess of 35.5 *ppt* at 200 m depth. A2000 indicates values of 32.25 *ppt*, however these are much less expansive when compared to Levitus94 (25 - 37^oS compared to 18 - 43^oS for Levitus94).

It appears that the low-latitude equatorial sub-surface waters are slightly exaggerated when relating to salinity, with figure 3.12 indicating values of 35 *ppt* compared to the 34.5 *ppt* Levitus94 values. Southern Ocean water below 37^oS for A2000 and 43^oS for Levitus94 indicate similar values.

Relating the salinity profiles to resolved current flow (see figures 3.3, 3.4 and 3.5), indicates current features are reasonably well represented. It is clear that salinity is strongly favouring the IT and continued SEC flow, conflicting with the Levitus94 plots indicating IOCW dominance in the region. It is possible that the accuracy of the Levitus94 dataset is questionable too for this reason, the mass balance of the model possibly correcting for

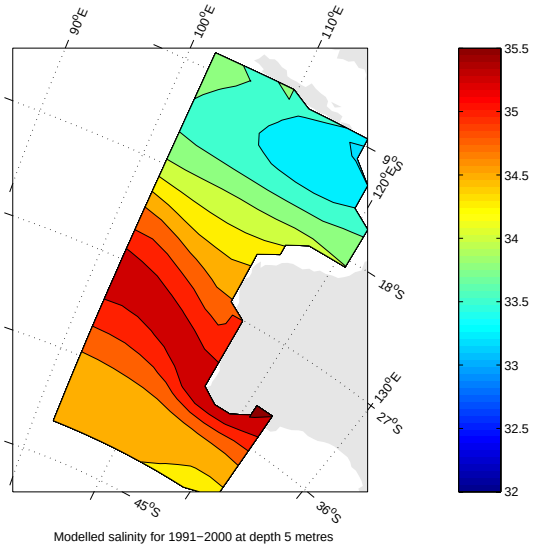

Figure 3.10: Modelled 10-yr mean salinity for A2000 at 5 m depth

anomalous tendencies.

3.3.4 Density

Surface density plots (figure 3.14) closely resemble near-current values represented in the Levitus94 Ocean atlas, however this too exaggerates the role of the SEC and the inflow of warmer, lower density tropical water.

Comparative surface density plots are presented in figures 3.14 and 3.15. These plots indicate a good replication of near-current surface density values by the A2000 dataset, with the slight poleward exaggeration of pycnoclines expressed in figure 3.14 compared to Levitus94 (figure 3.16).

Temperature dominance is apparent in the calculation of density (equation 3.2), as the profile plots (figures 3.16 and 3.17) more closely resemble temperature than the corresponding salinity profiles, agreeing with Batteen and Huang (1998), who indicated that temperature is the most dominant variable influencing density in the LC system.

South of 24^oS density values are well represented in the A2000 dataset. Above this latitude the dominance of the SEC is prevalent, with decreased density due to the warmer,

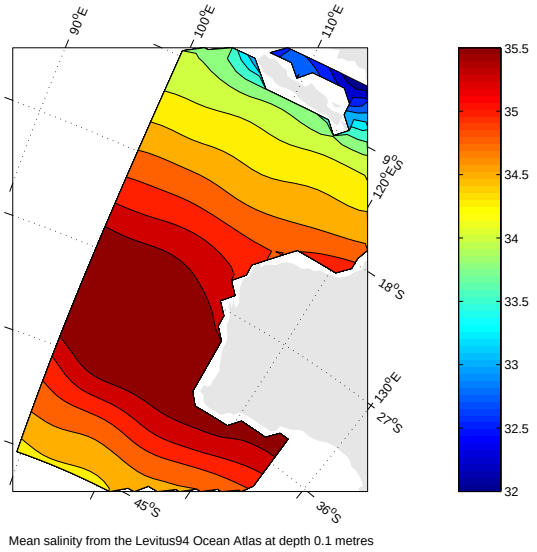

Figure 3.11: Observed mean surface salinity *(from Levitus94 Annual, 2002)*

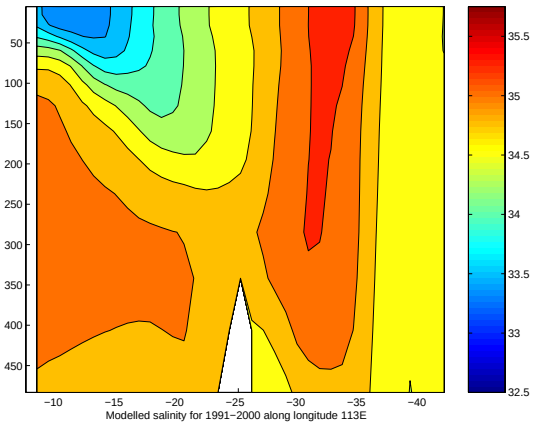

Figure 3.12: Modelled 10-yr mean salinity profile along 113^oE for A2000

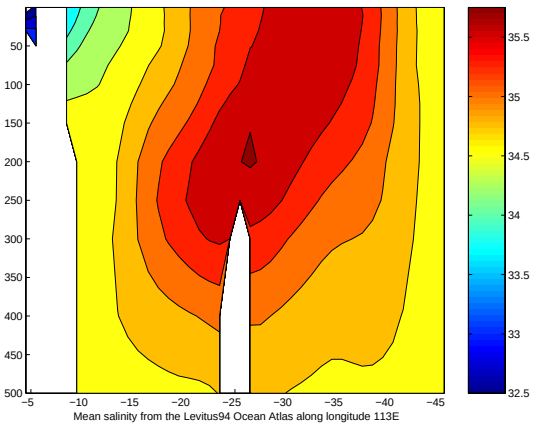

Figure 3.13: Observed mean salinity profile along 113^oE *(from Levitus94 Annual, 2002)*

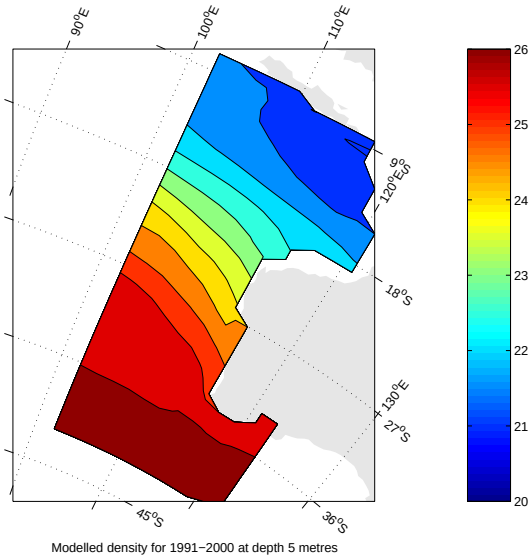

Figure 3.14: Modelled 10-yr mean density for A2000 at 5 m depth

lower salinity tropical IT (and SEC). It is clear from the A2000 plot that the IOCW does not play a marked role, however this flow may be represented poleward of 35^oS as a bulge of higher density water extending around to the Southern Ocean and the Great Australian Bight, possibly combining with LC flow at this location (similar to the salinity plot, figure 3.10). When relating the continued flow of IOCW in the A2000 dataset, it is clear that the salinity and density plots (figures 3.10 and 3.14 respectively) agree well, resolving this extended flow at 35 *ppt* and 25 σ_Θ respectively (South of CL 35 - 36^oS).

Relating density profiles to resolved current flows (see figures 3.3, 3.4 and 3.5), indicates current features are reasonably well represented. It is clear that density plots are representing an exaggerated IT and continued SEC flow, agreeing well with salinity plots. Representation of the IOCW (poleward of 24^oS) closely resembles the Levitus94 profiles, however east of 113^oE underestimation of continued IOCW and LC flows are apparent.

3.3.5 Geopotential Anomaly

Calculated plots of geopotential anomaly indicate that the model is overestimating the (285 m) steric height gradient when compared to the Levitus94 dataset, a feature

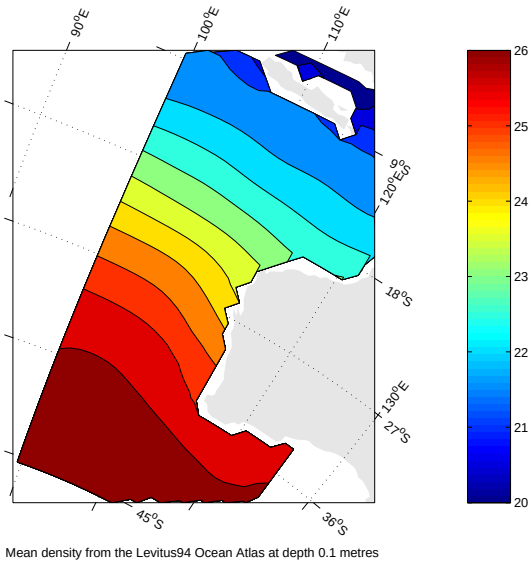

Figure 3.15: Observed mean surface density *(from Levitus94 Annual, 2002)*

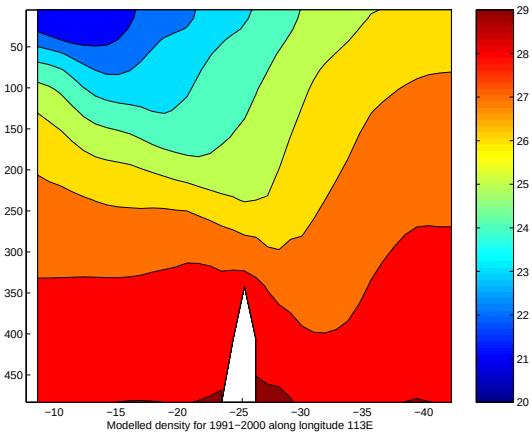

Figure 3.16: Modelled 10-yr mean density profile along 113^oE for A2000

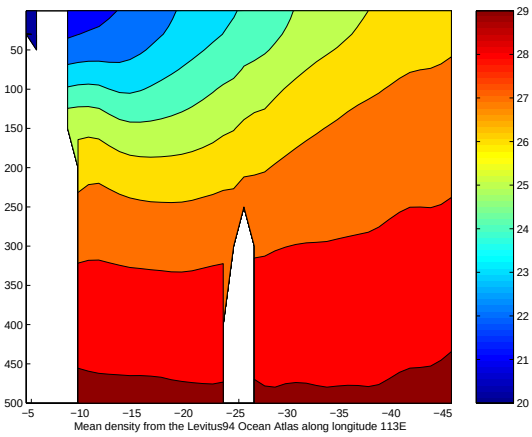

Figure 3.17: Observed mean density profile along 113^oE *(from Levitus94 Annual, 2002)*

acknowledged to drive the LC. This is aligned with the exaggerated (warm, low salinity and corresponding low density) SEC flow - as this flow is persistent over the top ∼200 m of oceanography, and the LUC appearing at 18^oS, 102^oE and 159 m depth. A steric height value of 0.11 m (figure 3.18 - red) relates to the dominance of these flows at 16.5 - 33^oS, 102^oE.

Figures 3.18 and 3.19 visualise the A2000 dataset and Levitus94 respectively. Calculated values off the North West Shelf (21^oS, 109.7 - 113.5^oE) and off Cape Leeuwin (35^oS, 109.7 - 113.5^oE) relate to the steric height gradient driving the poleward LC flow. Values relating to these locations give a fairly similar result, with the model slightly overestimating the gradient at 0.05 m (0.11 North West Shelf, 0.06 Cape Leeuwin), the Levitus94 profile indicating 0.04 m (0.09 North West Shelf, 0.05 Cape Leeuwin). The tendency for the model to exaggerate this is more prevalent in figure 3.18 with this plot relating well to IOCW flow (figure 3.4) and temperature profiles (figures 3.8 and 3.9).

The A2000 dataset indicates the alongshore steric height gradient is slightly overestimated, indicating a potential for stronger LC flows (compared to the Levitus94 plot, figure 3.19), however finer model resolution would need to be developed to resolve this flow specifically.

3.4 Regional replication

The CSIRO Mark 3 AOGCM closely replicates the observed regional ocean climate experienced off Western Australia. This model resolves for the 5 major currents, documented in studies of the region.

The nature of the 10-yr mean dataset indicates that current speeds are not well resolved, and transports associated with currents similarly underestimated. The qualitative replication of these, and good replication of temperature, salinity and density fields

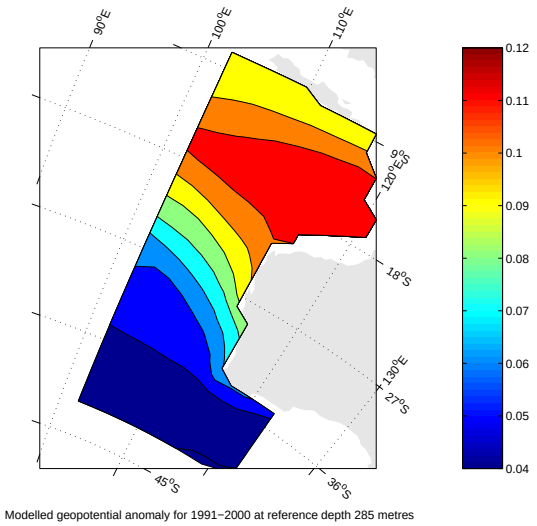

Figure 3.18: Modelled 10-yr mean geopotential anomaly for A2000 at 285 m reference depth

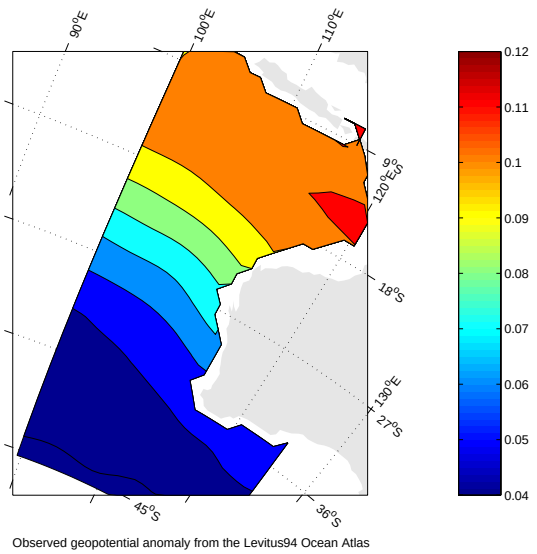

Figure 3.19: Observed mean geopotential anomaly at 300 m reference depth *(from Levitus94 Annual, 2002)*

is expressed by the model, the anomalous warm condition expressed along the Western Australia coast, when compared to equivalent eastern (ocean) boundary regions.

Increased resolution of the Mark 3 model, when comparison is made to the Mark 2, and improved representation (parameterisation) of important sub-grid scale processes (such as meso-scale eddies), are key reasons for improved replication of regional oceanography (Houghton *et al.*, 2001). The nature of the complex sub-grid scale oceanography off Western Australia, due to the narrow (< 100 km) LC flow, is the key reason why regional oceanography is not completely resolved ($\sim$100 km [latitude] by $\sim$200 km [longitude] resolution). A doubling of this resolution is likely then to resolve for the LC flow, with an expectation for future models to reach suitable resolution within the next few years (Dr John McGregor *Pers. Comm.* CSIRO - DAR, 25-10-02).

CHAPTER 4
RESULTS

4.1 Atmospheric Circulation

4.1.1 Regional Circulation Patterns

Figures 4.1 to 4.4 suggest a poleward migration of the subtropical high pressure axis. Analysis of maximum values for each dataset indicate that this is not the case, but rather an intensification of this system, broadening, and centred for A2000 to A2100 (and C2000 to C2100) at 31^oS, 99.5^oE.

Table 4.1 indicates maximum, minimum and gradient (maximum value minus minimum value - representing the pressure gradient between the dominant sub-tropical high pressure and the minimum value [representing subpolar lows] in the southern region) values (and locations for Max. and Min.) for each of the datasets, A2000 to A2100, and C2000 to C2100 respectively.

The A2000 and A2070 (and A2100) MSLP plots (figure 4.1 and 4.2 respectively), indicate an intensification of the subtropical high pressure feature, supported by figures 4.3 and 4.4. When comparing figures 4.1 and 4.2, it is apparent that a subtle decrease to the pressure gradient over the southwest of WA (SWWA) is occurring, suggesting slight decreases in geostrophic windstress, represented by the decreased gradient values (the A2100 plot indicates very similar values to A2070, and for this reason is not included). Dominance of this subtropical high pressure cell becomes evident when comparing these figures, increased pressures indicated in the southern portion of figure 4.2 (43 - 44^oS).

Change seems to be most prevalent when comparing A2000 and A2070, with an increase of 1.6 hPa in the most south-western portion (41 - 43^oS, 99 - 109^oE - figure

Dataset	Max	Min	Gradient
A2000	1021.7 (31^oS, 99.5^oE)	1006.4 (44^oS, 114^oE)	15.3
A2070	1022.3 (31^oS, 99.5^oE)	1007.8 (44^oS, 116^oE)	14.5
A2100	1022.1 (31^oS, 99.5^oE)	1007.1 (44^oS, 114^oE)	15.0
C2000	1021.5 (31^oS, 99.5^oE)	1006.4 (44^oS, 118^oE)	15.1
C2070	1021.5 (31^oS, 99.5^oE)	1005.1 (44^oS, 116^oE)	16.4
C2100	1021.9 (31^oS, 99.5^oE)	1006.1 (44^oS, 114 - 118^oE)	15.8

Table 4.1: Modelled MSLP values and locations for each of the datasets (All values represent hPa)

4.3), attributable to increased dominance of the subtropical high. This feature may reduce the ability for sub-polar low pressure systems to interact with SWWA, limiting northward migration. Dominance of this feature continues to extend southeastwards in figure 4.4 (A2100 compared to A2000), an increase of 1.4 hPa expressed across the entire southern portion of the study region (41 - 44^oS).

An increasing trend is also apparent in the north-western section for this time period, the source region for the tropical-extratropical cloudbands, and associated with cyclone development during the winter monsoon (Jan/Feb - equatorial wet season). Increases to this region may suggest a decline to low pressure developments, corresponding with decreased cloudband and cyclone activity.

Temporal (or drift) variability is inherent in any climate model. To account for this, control scenarios are run, attempting to isolate this feature. To correct forced scenarios, subtraction of the control drift from the forced scenario is undertaken. The resulting output relates to the effect of the forcing only, variability removed.

Comparing forced output to the control scenario ensures that the model (and temporal) variability are also considered. It is clear from figures 4.5 and 4.6 that only subtle change to circulation (between C2000 and C2070 respectively) is occurring, with a slight

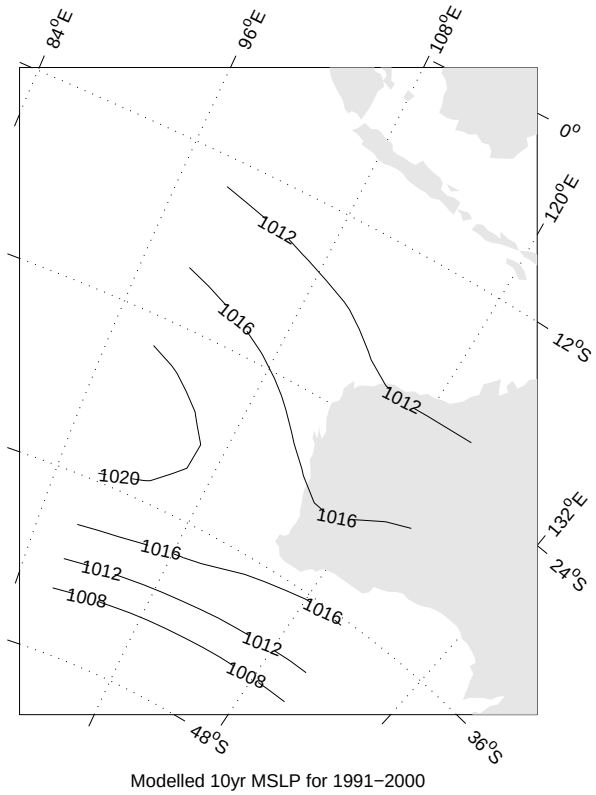

Figure 4.1: Modelled 10-yr mean MSLP for A2000

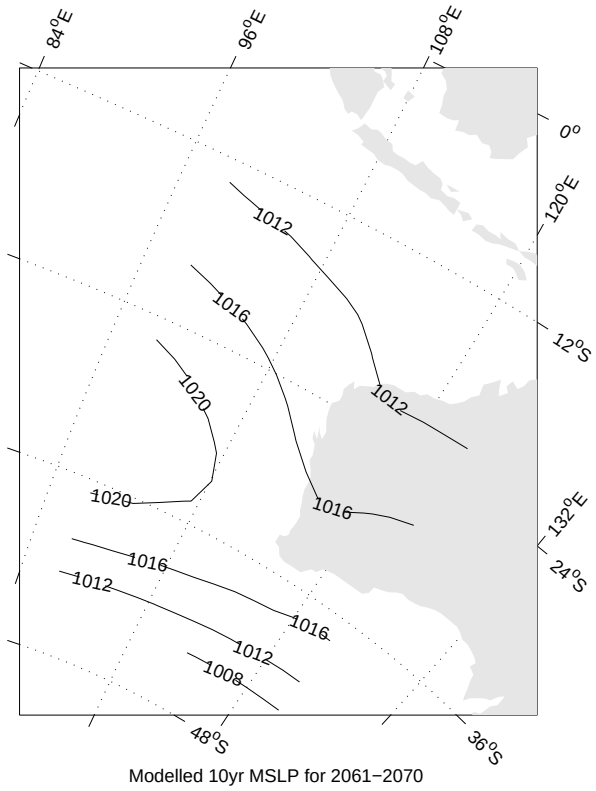

Figure 4.2: Modelled 10-yr mean MSLP for A2070

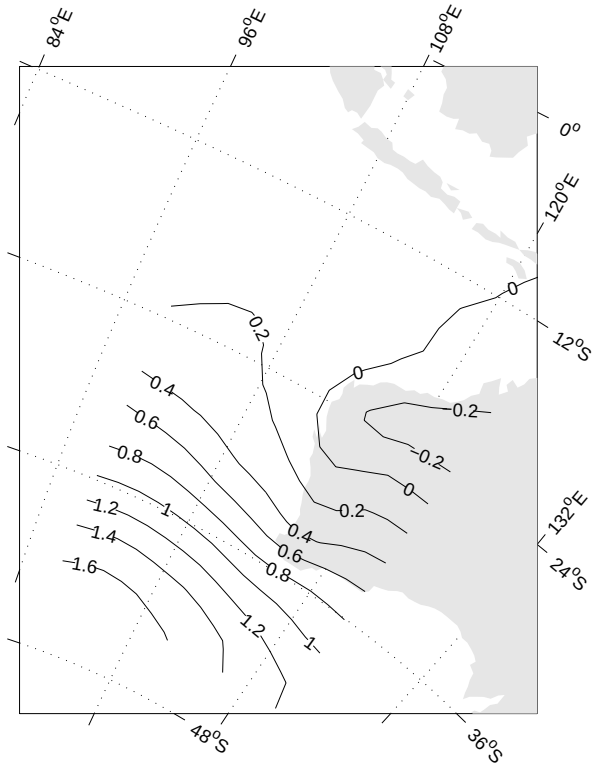

Figure 4.3: Modelled 10-yr mean MSLP change for A2070 compared to A2000

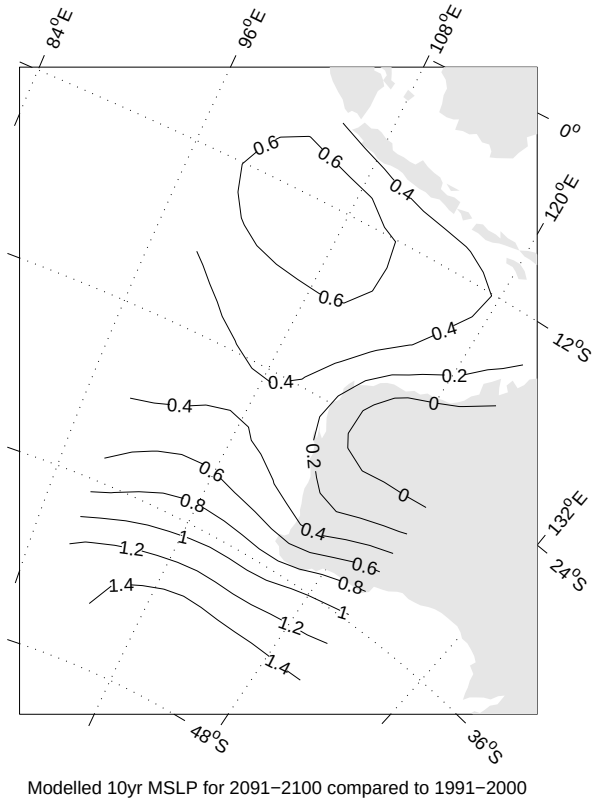

Figure 4.4: Modelled 10-yr mean MSLP change for A2100 compared to A2000

intensification of the pressure gradient existing over SWWA.

A maximum increase (for C2070 compared to C2000) of 0.16 hPa is apparent for the central region (27^oS, 103^oE) associated with the sub-tropical high axis, a decrease of 0.75 in the southern portion (44^oS, 111^oE) expressed in figure 4.7. This change indicates decreased dominance of the sub-tropical high cell, with decreasing values over the southern portion of the study region, an opposing response to the forced scenario. Figure 4.8 (C2100 compared to C2000) indicates a more dominant sub-tropical high, with an increase in maximum pressure of 0.4 hPa aligned with this axis (compared to C2000). The decreased values in the southern portion suggest this feature is weakening from C2000 to C2100, decreased values of -0.4 hPa indicated in the most southern portion of the study region (figure 4.8).

Comparison between C2000 and A2000 were also reviewed, with greatest difference of -0.4 hPa indicating slightly higher values for the forced run. These changes recorded at 26^oS, 122^oE, simulating the sub-tropical high, agreeing with the tendency for higher values, a response to the forcing.

4.1.2 Windstress

Windstress indicates the direction of wind forcing over the ocean surface, leading to wind driven currents, and on an ocean gyre scale, Ekman forcing of the ocean basins.

Analysis of 10-yr mean datasets ensures that wind stress values are greatly underestimated (due to an integration of opposing seasonal patterns), direction of forcing, however, qualitatively replicates documented climatologies, resolving for dominant wind patterns associated with the region.

Table 4.2 indicates the maximum and minimum values for each of the datasets, these values taken from the meridional grid line with the highest windstress values (99.5^oE),

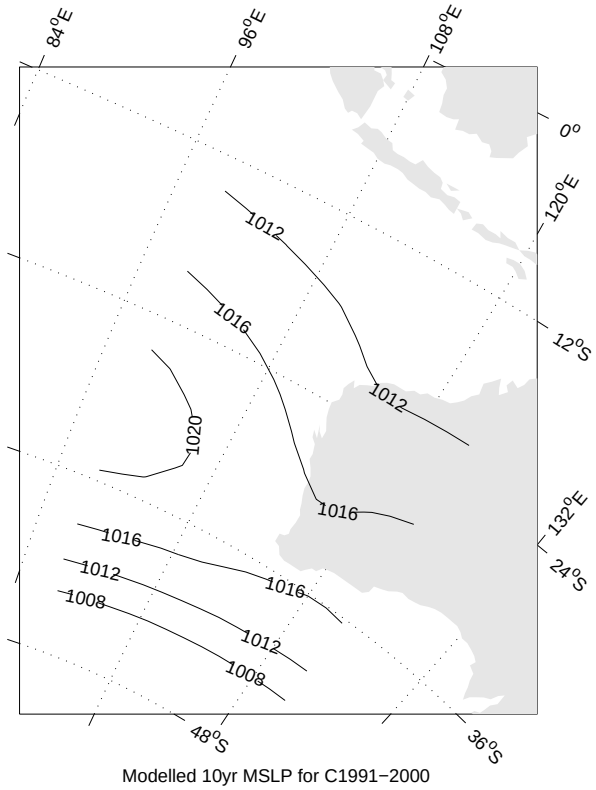

Figure 4.5: Modelled 10-yr mean MSLP for C2000

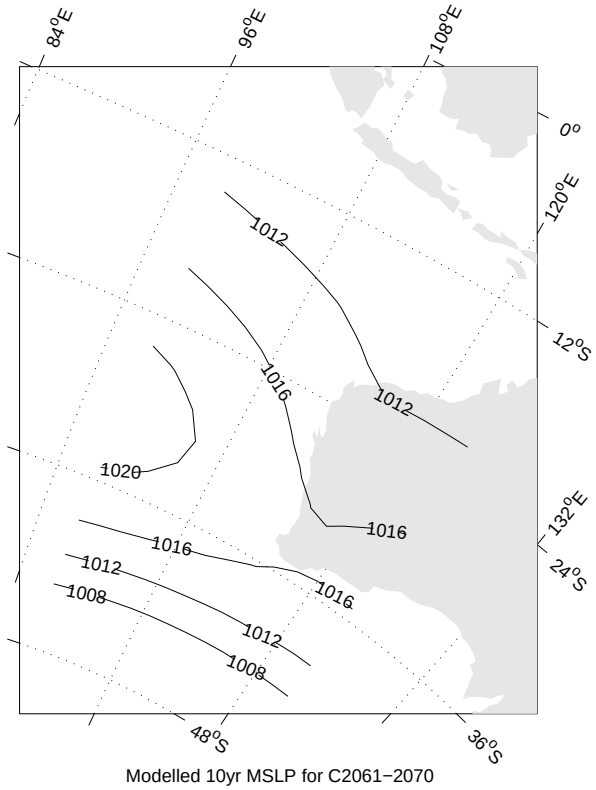

Figure 4.6: Modelled 10-yr mean MSLP for C2070

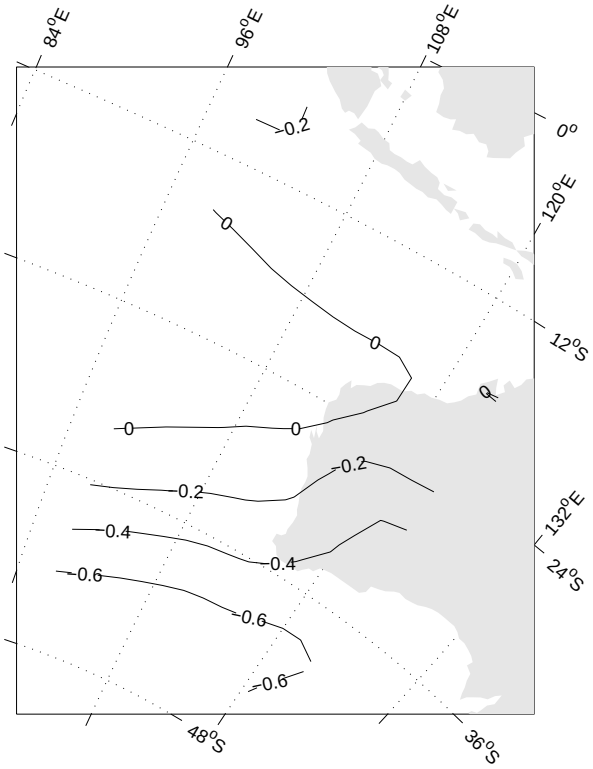

Figure 4.7: Modelled 10-yr mean MSLP for C2070 compared to C2000

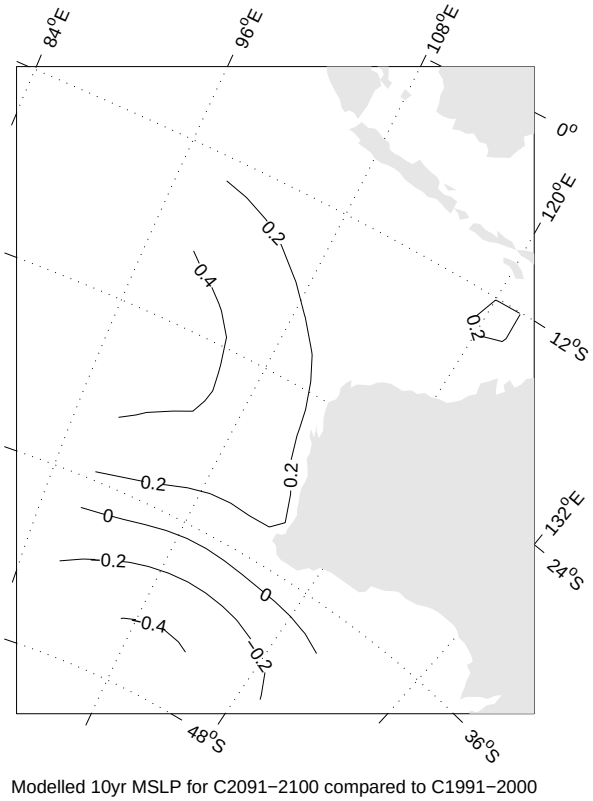

Figure 4.8: Modelled 10-yr mean MSLP for C2100 compared to C2000

Dataset	Max	Min	Mean
A2000	2.14 (42.5^oS)	0.25 (32^oS)	0.757
A2070	2.06 (42.5^oS)	0.26 (32^oS)	0.732
A2100	2.08 (42.5^oS)	0.22 (32^oS)	0.713
C2000	2.07 (42.5^oS)	0.25 (32^oS)	0.754
C2070	2.15 (42.5^oS)	0.27 (31^oS)	0.783

Table 4.2: Modelled windstress values and locations for each of the datasets taken along 99^oE (All values represent $dyne\ cm^{-2}$)

correlating with the highest (roaring forties 42.5^oS, most southerly value) and lowest (sub-tropical high axis 31 - 32^oS) values. It is clear from table 4.2 that a decreased pattern is apparent in the forced scenario, with increased values indicated for the corresponding control dataset. These correspond well with the circulation plots and summary table 4.1, indicating a decreased gradient for the forced scenario, increasing for the control, an enhanced gradient driving stronger winds. This conclusion is supported by mean values expressed in table 4.2. Ekman transport (driven by windstress), therefore is suggested to marginally decrease in the forced scenario, the opposite pattern occurring in the control scenario.

When comparing figures 4.9 and 4.10 (A2000 and A2070 respectively) and relating these to table 4.2, the more dominant subtropical high is represented (low windstress correlating with the axis of the sub-tropical high). Comparing A2100 to A2000 (figure 4.11), it appears that a weakening of the mid-latitude (29 - 42^oS) westerly windstress and a marginal (0.1 $dyne\ cm^{-2}$) weakening of the central low-to-equatorial (17 - 26^oS) south easterly trades is also occurring. Slight increases (0.1 $dyne\ cm^{-2}$) to the equatorial (7 - 12^oS) south easterly is also apparent, a decreasing trend for the southern latitudes westerly windstress (20 - 42^oS), corresponding well a more dominant high pressure cell (figures 4.1

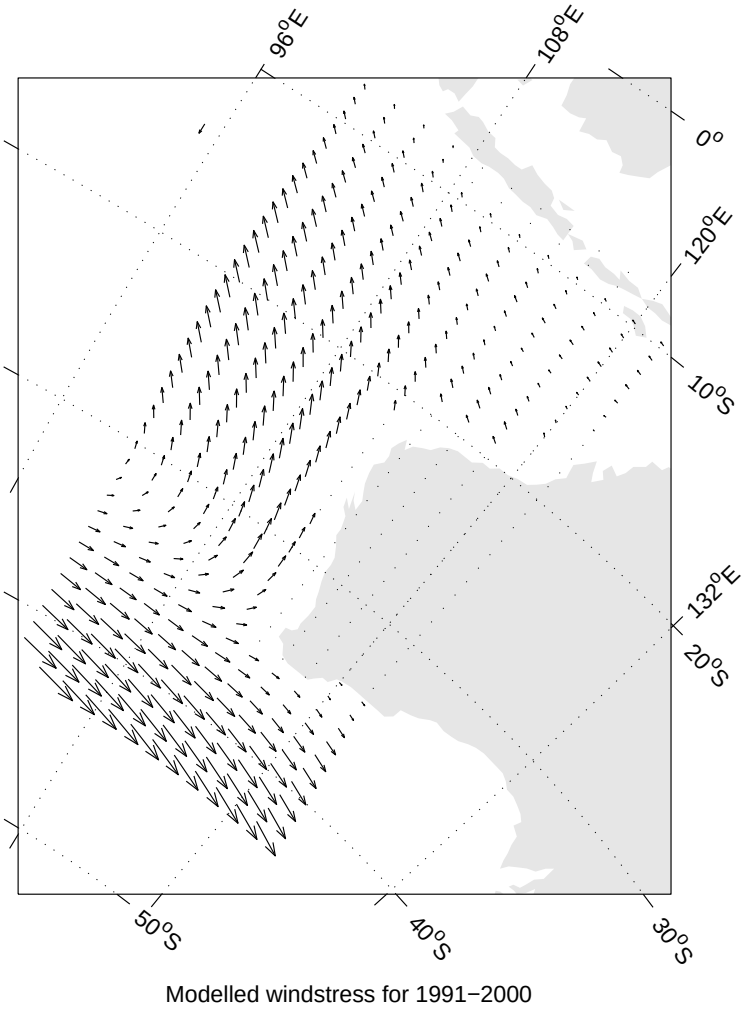

Figure 4.9: Modelled 10-yr mean wind stress for A2000 (Scale arrows represent 0.5 *dyne* cm^{-2})

to 4.4). Plots relating A2070 to A2000, indicate change occurring to westerly windstress only, maximum decreases of ∼0.25 *dyne* cm^{-2} indicated by a comparison plot (not shown).

Peak windstress values are observed in the most south-western corner of the study region, replicating the roaring forties, with values exceeding 2.1 *dyne* cm^{-2} for A2000 and C2070 (table 4.2). Lowest values correspond to the centre-axis of the subtropical high, at 32^oS for A2000 to A2100 and C2000, and 31^oS for C2070 respectively.

C2000 and C2070 were the only control datasets available for windstress comparison. Analysis of these indicated only subtle changes between C2070 and C2000 (a maximum change of 0.08 *dyne* cm^{-2}), associated with the increased roaring forties (table 4.2, possibly

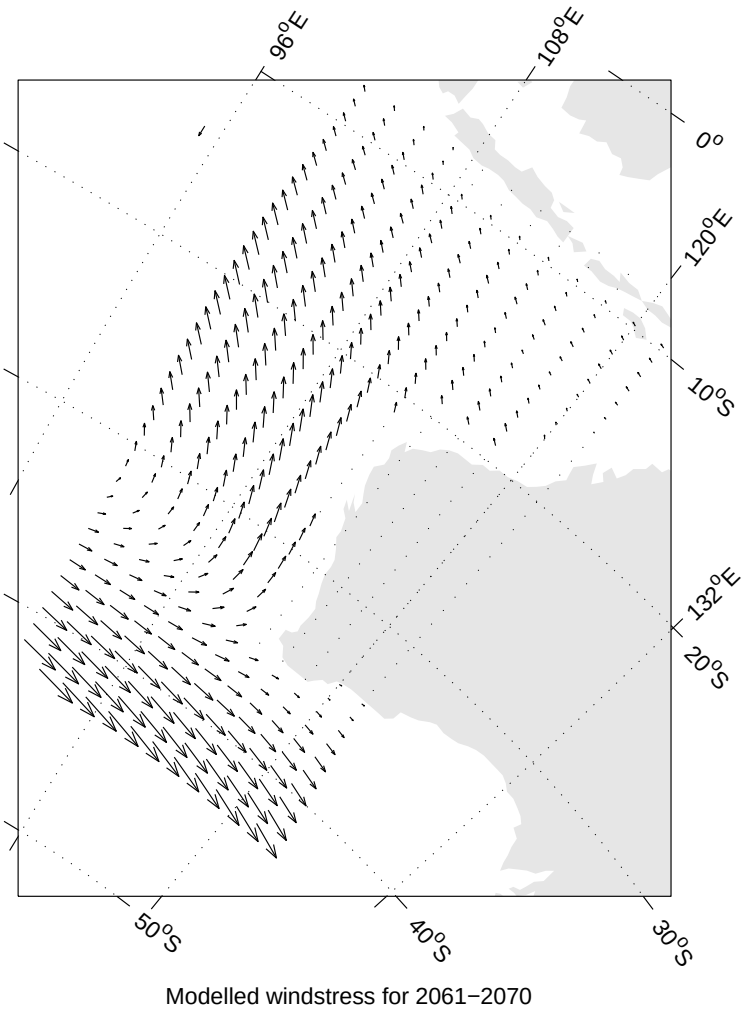

Figure 4.10: Modelled 10-yr mean wind stress for A2070

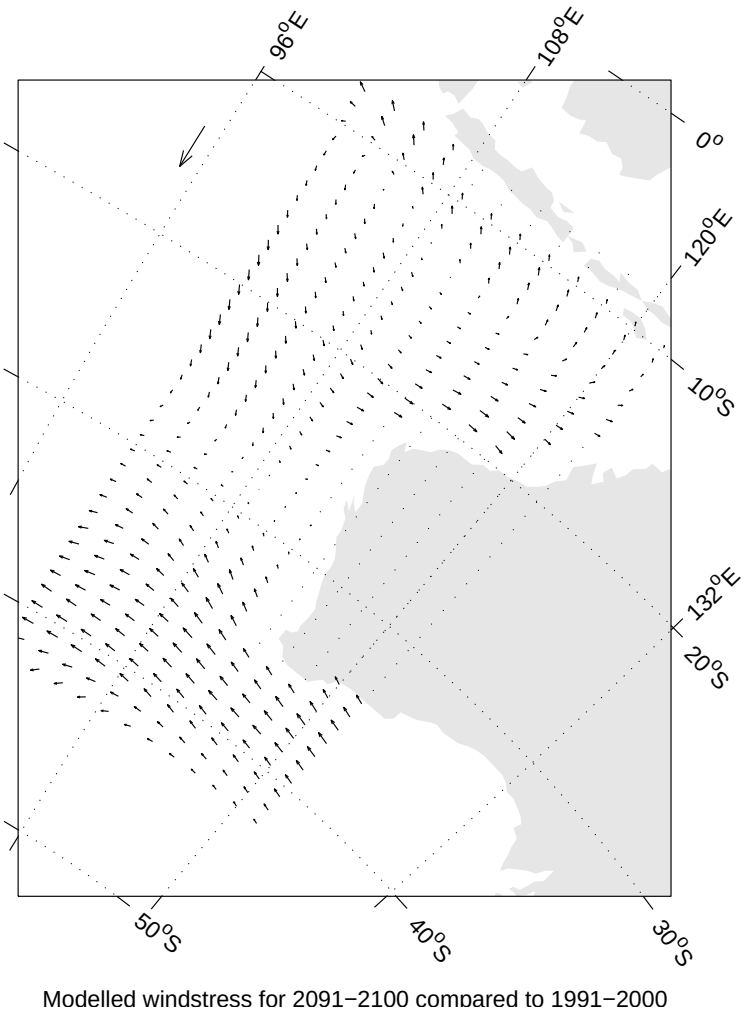

Figure 4.11: Modelled 10-yr mean wind stress for A2100 compared to A2000

linked to sub-polar low pressure systems) and a less dominant sub-tropical high, agreeing well with figure 4.7.

Comparison between the C2000 and A2000 datasets were also reviewed, with greatest change of 0.07 $dyne\ cm^{-2}$ indicating slightly lower values for the control run. These changes recorded at 42^oS, 99^oE, agreeing with values presented in table 4.2.

4.2 Ocean Circulation

4.2.1 Sea Surface (and subsurface) Temperature

Figure 4.12 and 4.13 summarise changes to surface (5 m) temperatures for A2070 - A2000 and A2100 - A2000 respectively. It is clear from these plots (and supporting profile plots) that marked increases in SST (and subsurface temperatures) are suggested by the model. For A2100 - A2000 a mean increase of 1.1^oC calculated for the top ∼285 m of the study region and maximum increases of 1.5^oC on the sea surface are indicated, with sub-surface values exceeding 2.0^oC at ∼78 m depth (2.13^oC - 18.5^oS, 121^oE). A corresponding increase of 0.6^oC is occurring for A2070, with a maximum sub-surface increase of 1.1^oC at ∼102 m depth (1.14^oC - 26^oS, 102^oE). This warming trend is clear when referring to profile plots (A2070 - A2000, figure 4.14 and A2100 - A2000, figure 4.15 - taken along 113^oE, the closest complete north/south transect to land). These values suggest an exponential rise in temperature, when the time period of 70 and 100 years respectively is taken into account.

It is likely that this increased temperature is attributable chiefly to greater flux from the atmosphere to the ocean, heating the top ∼500 m of the ocean profile considerably (figure 4.16), leading to a marked stratification of the ocean profile. This hypothesis is supported by calculated North Pacific-Indian Ocean heat transport (attributable to the IT flow, table 4.5), indicating very small increases associated with this heat source, and consequently, not accounting for the considerable increase to these temperature values.

Climatic Domain	Seconds	Equivalent
ATMOSPHERE		
Boundary layer	10^5	24 hours
Free	10^6	11 Days
OCEAN		
Mixed layer	10^6 - 10^7	Months to years
Deep	10^{10}	300 years
Sea-ice	10^6 - 10^{10}	Days to 100's of years

Table 4.3: Equilibrium times for key climate subsystems *(from McGuffie and Henderson-Sellers, 1999)*

IOCW heat transport is also a significant feature affecting regional oceanography. This feature is accountable for increased heat transport into the region, with an increasing trend suggested for the forced scenario. Values of 0.6 and 1.1^oC correspond to 70 and 100 year predictions. Forecasts for global atmospheric warming, indicate amplified temperatures of between 1.4 - 5.8^oC predicted for 2100 (Houghton *et al.*, 2001), these values correlate with increases to atmospheric heat flux into the ocean, the magnified gradient driving increased flux. Smaller increases in the ocean (when compared to the atmosphere, and expressed by the model output), are linked with the high specific heat capacity of seawater. This ensures that the response of the ocean is much slower to a changing mean global surface temperature, some representative timescales presented in table 4.3.

Table 4.4 indicates a marked change to temperature of the ocean. It is interesting to note the nature of these changes. Table 4.4 suggests a significant increase in mean temperature occurs between the years A2000 to A2070. The bulk of this increase corresponds to a $\sim$0.6^oC increase in the maximum value, with a $\sim$0.3^oC increased minimum. Table 4.6 continues this analysis, with a determination of difference values for each of the datasets. There appears to be a pattern in the maximum temperature values, with values located

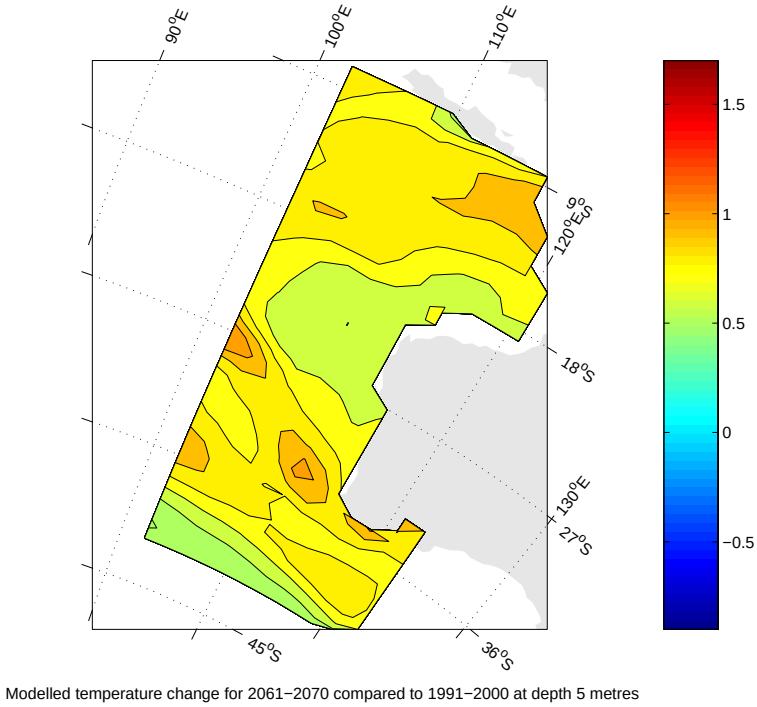

Figure 4.12: Modelled 10-yr mean SST change for A2070 compared to A2000

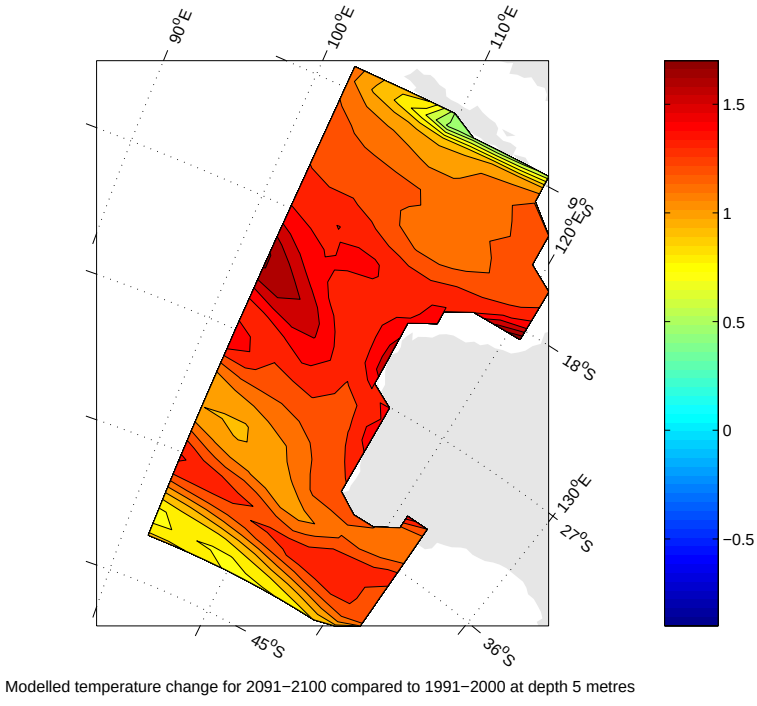

Figure 4.13: Modelled 10-yr mean SST change for A2100 compared to A2000

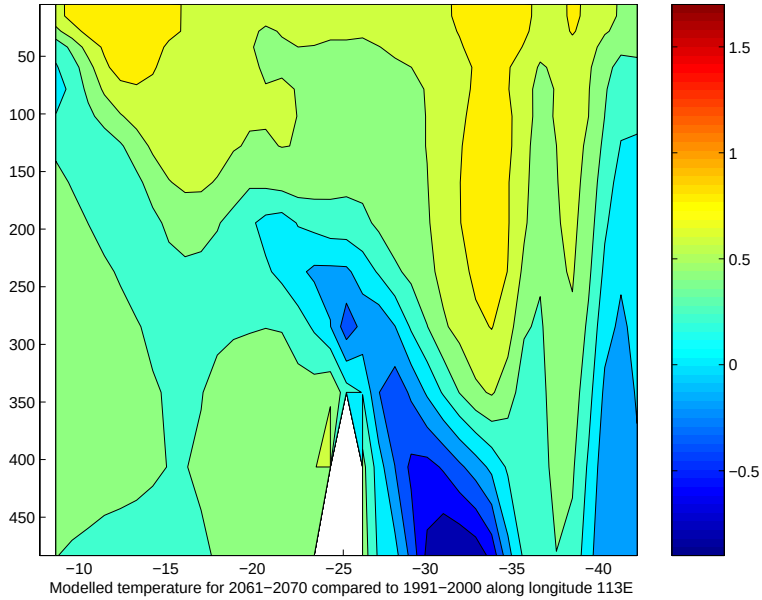

Figure 4.14: Modelled 10-yr mean temperature change for A2070 compared to A2000 along 113^oS

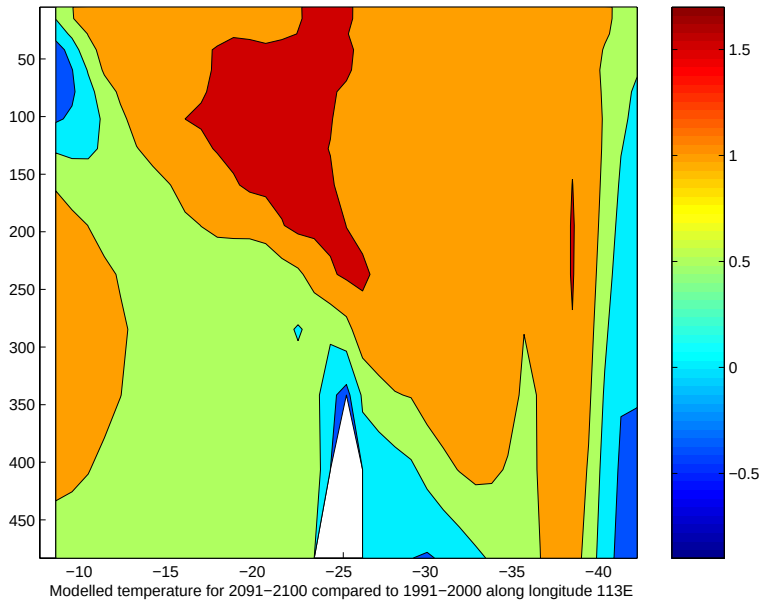

Figure 4.15: Modelled 10-yr mean temperature change for A2100 compared to A2000 along 113^oS

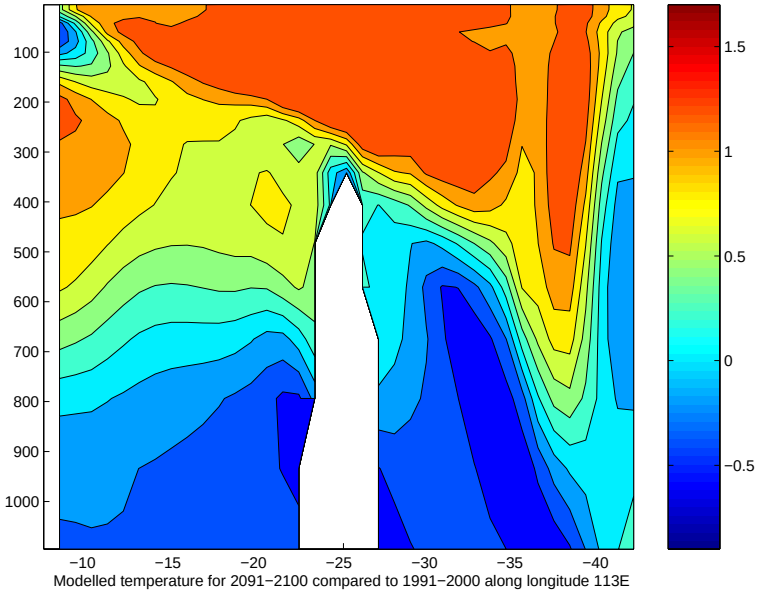

Figure 4.16: Modelled 10-yr mean temperature change for A2100 compared to A2000 along 113^oS

Dataset	Surface mean	Grand mean	Max	Min	Median	SE
A2000	20.8	17.8	29.3	8.1	17.3	0.0826
A2070	21.6	18.4	29.9	8.4	17.9	0.0840
A2100	22.0	18.9	29.9	8.8	18.4	0.0842
C2000	20.5	17.5	28.6	7.9	17.2	0.0813
C2070	20.3	17.3	28.7	7.8	16.8	0.0817

Table 4.4: Modelled temperature values for each of the datasets relating to the top ∼285 m (All values represent ^oC)

Dataset	IT	IOCW
A2000	1.21	0.49
A2070	1.22	0.52
A2100	1.19	0.54
C2000	1.18	0.55
C2070	1.18	0.53

Table 4.5: Modelled heat transport inputs for each of the datasets relating to the IT (top ∼400 m) and IOCW (top ∼160 m) (All values represent PW)

in the subsurface layers (levels 7, 6 and 6 [102 and 78.5 m] respectively for A2070-A2000, A2100-A2000 and A2100-A2070), in accord with Cai and Gordon (1998) who indicated maximum heating occurred in the subsurface layers, their analysis undertaken from output of the CSIRO Mark 2 ocean model. A similar order of increase is also expressed for A2070 to A2100, $\sim 0.5^oC$ for the grand mean, and a $\sim 0.4^oC$ increase to the minimum. The maximum value remains static at 29.9^oC (in reference to A2070), whereas the median value increases to 18.4^oC (from 17.9^oC, A2070). This suggests that advection of heat within the ocean is occurring, a change from the pattern expressed in A2070, correlating with greatly increased flux from the atmosphere, driving ocean heating, supported by surface mean values (0.8^oC increase A2000 to A2070, and 0.4^oC increase A2070 to A2100).

Work by Bi *et al.* (2001), Cai and Gordon (1998), Clark *et al.* (2002) and Matear and Hirst (1999) suggest that increased CO_2 model runs are indicating a decreasing global THC. This is driven by a more stratified (less dense subsurface water) condition, leading to a decreased density gradient driving the circulation. Figure 4.16 illustrates this scenario, with an increase in the mean temperature of the top 1000 m, A2100 compared to A2000 along 113^oE. It is clear from this figure, due to the marked increase to subsurface temperatures, a strengthened gradient is occurring at $\sim$500 m depth. Such a feature is illustrative of a more stratified ocean, leading to decreased THC.

The temperature (depth) layer plots relate closely to corresponding current plots, resolving the 5 major currents and their respective ocean climates. Figure 3.7, a surface plot for the A2000 dataset, resolves the cooler water of the WAC, the warmer IOCW, the tropical, warm SEC and the temperature profile of the LC (with downward aligned isotherms indicating greater temperatures inshore compared to the central Indian Ocean). Depth profile plots resolve for the cooler LUC, this feature prominent from $\sim$160 - $\sim$1500 m depth.

Dataset comparison	Surface mean	Grand mean	Max	Min	Median	SE
A2070 - A2000	0.8	0.6	1.1	-0.3	0.62	0.0034
A2100 - A2000	1.2	1.1	2.1	-1.2	1.19	0.0055
A2100 - A2070	0.4	0.5	1.8	-1.4	0.5	0.0045
C2070 - C2000	-0.2	-0.2	1.6	-1.0	-0.25	0.0029

Table 4.6: Modelled changes to temperature for each of the datasets relating to the top ∼285 m (All values represent ^oC)

The control scenario indicates cooler initial conditions (C2000 compared to A2000) with corresponding maximum, minimum and median values expressed in table 4.6. Temperature increases for the A2 scenario are likely due to increased CO_2 forcing, the sub-region reflecting changes expressed in the global grid (Dr Tony Hirst *Pers. Comm.* CSIRO - DAR, 21-10-02).

Analysis of the control run output indicates a decreasing temperature trend, with greater variation when compared to corresponding A2 scenario output. Table 4.6 highlights this increased variation, with a maximum increase of 1.6^oC and decrease of -1.0^oC (variation 2.6^oC) compared to the equivalent 1.4^oC for A2070-A2000. Figure 4.17 and 4.18 express this decreasing trend, surface values indicating changes of between 0 to -0.5^oS, and the profile plot indicating a general decrease of -0.5^oC, with a subsurface heating of 1.6^oC occurring at 25^oS in ∼300 m of water.

4.2.2 Salinity

Figure 4.19 summarises the change to the surface (5 m) salinity (values are indicative of changes in *ppt*), corresponding well with the surface current plot, indicating continued flow of the SEC into the central Indian Ocean. The SEC is clearly more dominant in the top ∼150 m of the profile (figure 3.12), with a return to homologous salinities beneath this

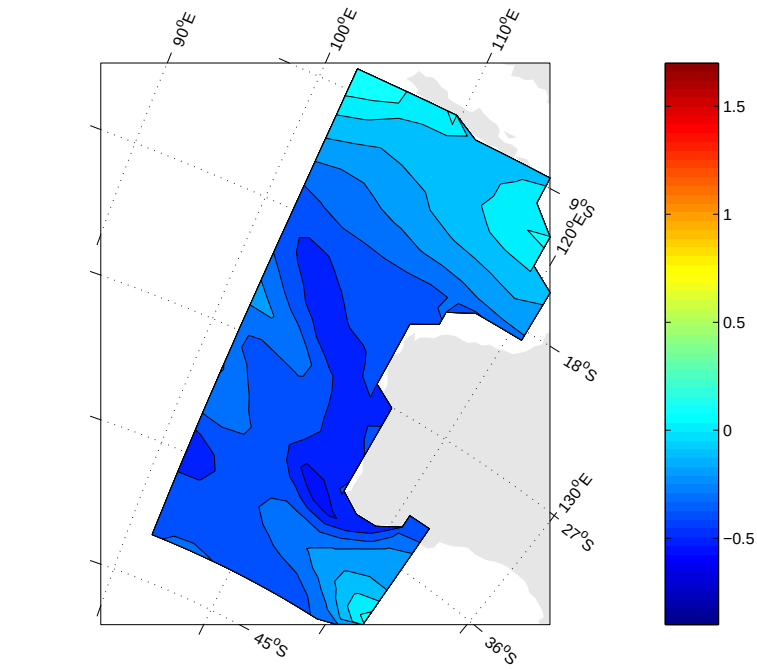

Figure 4.17: Modelled 10-yr mean SST change for C2070 compared to C2000

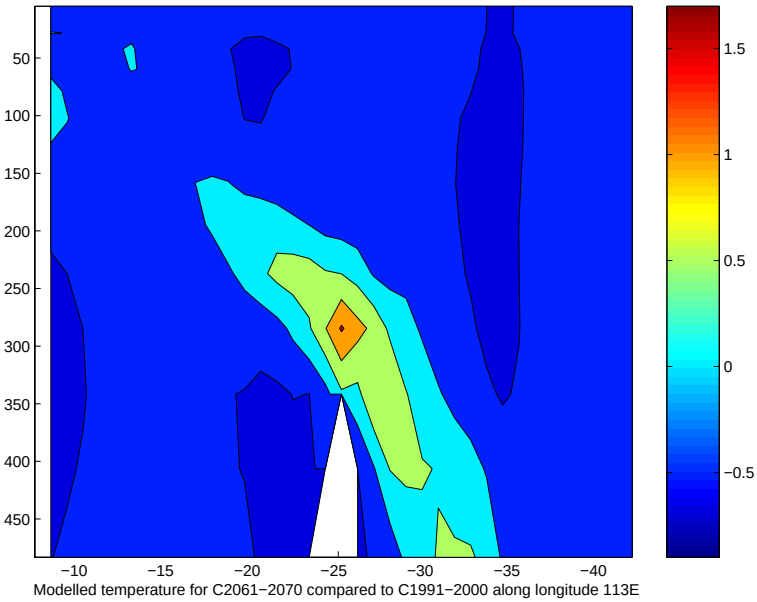

Figure 4.18: Modelled 10-yr mean temperature change for C2070 compared to C2000 along 113^oS

depth .

It appears that the greatest decrease in salinity is apparent at the interface between the IOCW and the SEC (18 - 23^oS, figure 4.19). The dominance of this decreasing salinity pattern is prevalent when looking at the grand mean calculation for the top ~285 m of the ocean profile. The relevance of such a broad calculation is questionable, as this averages key salinity signatures for corresponding currents, however, the -0.07 *ppt* mean change for A2070 compared to A2000 indicates that the forcing enhanced tropical water intrusion (IT - tropical high-temp, low-salinity water and continued SEC flow) has a significant effect on regional oceanography. This tendency is also expressed in tables 4.7 and 4.8. Mean values indicate a drop in salinity from A2000 to A2070, corresponding well with figure 4.19, suggesting increased dominance of the IT and SEC flows. The comparison of minimum and median values for A2000 and A2070 also support this conclusion.

Analysis of the A2100 dataset when compared to both A2000 and A2070 shows a different story. These values indicate a marked increase to salinity, with corresponding increases to all values included for table 4.7. This indicates a more dominant IOCW inflow, bringing saltier, denser water from the central Indian Ocean. This feature is clear in figure 4.19, in agreement with the analysis of Andrews (1977, 1983) and Church *et al.* (1989), indicating this flow is centred around 29 - 34^oS interacting with the LC at this location and continuing to flow south and east into the Great Australian Bight. The IOCW intrusion becomes more pronounced between A2070 to A2100. The reason for this increased intrusion is not clear, however, may be linked to geostrophic flow attempting to balance for the decreased salinity (and density) trend apparent over A2000 to A2070.

Depth profile plots suggest a more dominant IT and SEC flow for A2070, again these plots indicating a tendency for upper profile decreased salinities (supporting the concept of a more stratified global ocean), and A2100 dominated by IOCW (apparent due to the

Dataset	Surface mean	Grand mean	Max	Min	Median	SE
A2000	34.4	34.6	35.7	32.8	34.7	0.008
A2070	34.3	34.6	35.7	32.7	34.6	0.009
A2100	34.5	34.8	36.0	32.9	34.8	0.008
C2000	34.2	34.5	35.5	32.7	34.6	0.009
C2070	34.2	34.5	35.6	32.4	34.6	0.009

Table 4.7: Modelled salinity values for each of the datasets relating to the top ∼285 m (All values represent *ppt*)

Dataset comparison	Surface mean	Grand mean	Max	Min	Median	SE
A2070 - A2000	-0.09	-0.07	0.17	-0.62	-0.05	0.001
A2100 - A2000	0.09	0.06	0.42	-0.38	0.06	0.001
A2100 - A2070	0.18	0.13	0.90	-0.23	0.09	0.002
C2070 - C2000	-0.01	-0.01	0.25	-0.22	-0.02	0.001

Table 4.8: Modelled changes to salinity for each of the datasets relating to the top ∼285 m (All values represent *ppt*)

intrusion of increased salinity water, however still indicating a more stratified ocean from increased upper profile temperature). Figure 4.20 indicates the modelled change to salinity for the top ∼285 m of the ocean for A2070 compared to A2000. It is clear when reviewing this plot that static (no-change) or decreases of up to -0.2 *ppt* are apparent for the upper ∼200 m, these changes again indicating the more dominant IT/SEC flow.

The salinity plots relate well to the temperature (and current) plots. It becomes clear when reviewing the output relating to depths greater than ∼800 m that there is no significant change, with all plots indicating a homologous ∼34 - 35 *ppt* (these depths taking many 100's of years to react to upper profile change [McGuffie and Henderson-Sellers, 1999], and not resolved in the limited time series of this dataset). Visualisations more clearly represent

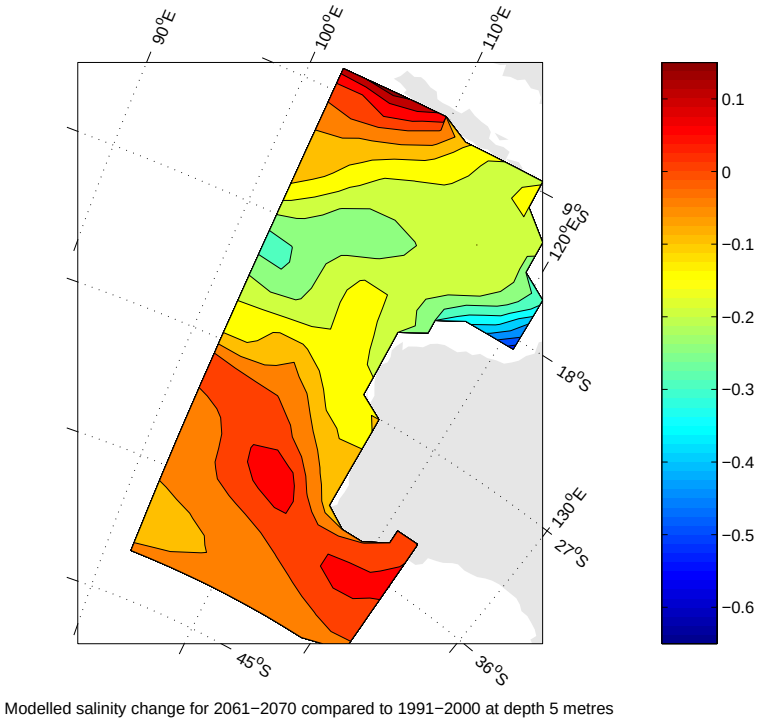

Figure 4.19: Modelled 10-yr mean surface salinity change for A2070 compared to A2000

the flow of the SEC at the surface when compared to the Levitus94 plots. A resolution of sub-surface lower salinity flow (possibly the SEC) is more prevalent in the Levitus94 dataset when compared to the model output, with the most clear representation of this flow between 100 - 300 m depths. It appears that the model therefore is underestimating the depth penetration of the SEC flow.

The freshening occurring off the North West Shelf (figure 4.19) is linked to a corresponding area of increased precipitation in the Mark 3 atmospheric output, feeding out to the ocean at this point (Dr John McGregor *Pers. Comm.* CSIRO DAR, 25-10-02).

The control scenario indicates fresher initial conditions (C2000 compared to A2000) with corresponding maximum, minimum and median values expressed in table 4.8.

Analysis of the control run output indicates a fairly static trend, with far less variation when compared to A2 output. Table 4.8 highlights this increased variation, with a maximum increase of 0.25 *ppt* and decrease of -0.22 *ppt* compared to 0.17 *ppt* and -0.62

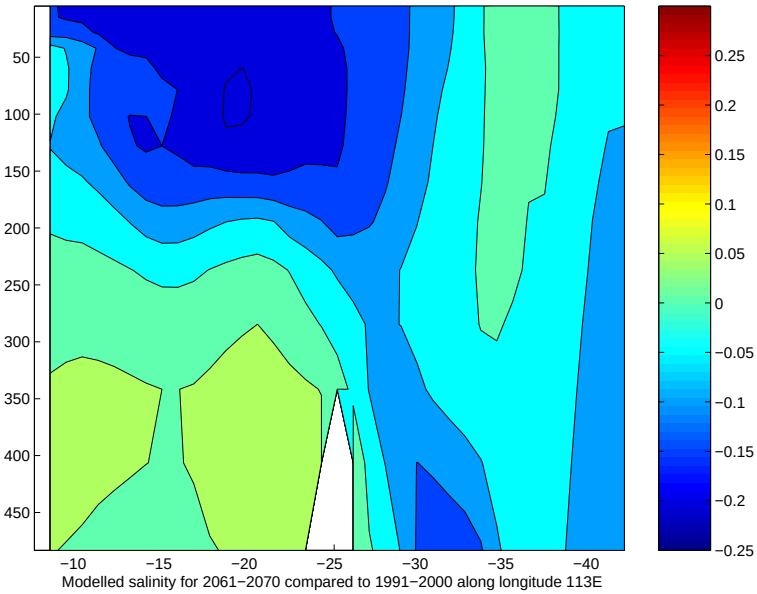

Figure 4.20: Modelled 10-yr mean salinity change for A2070 compared to A2000 along 113^oS

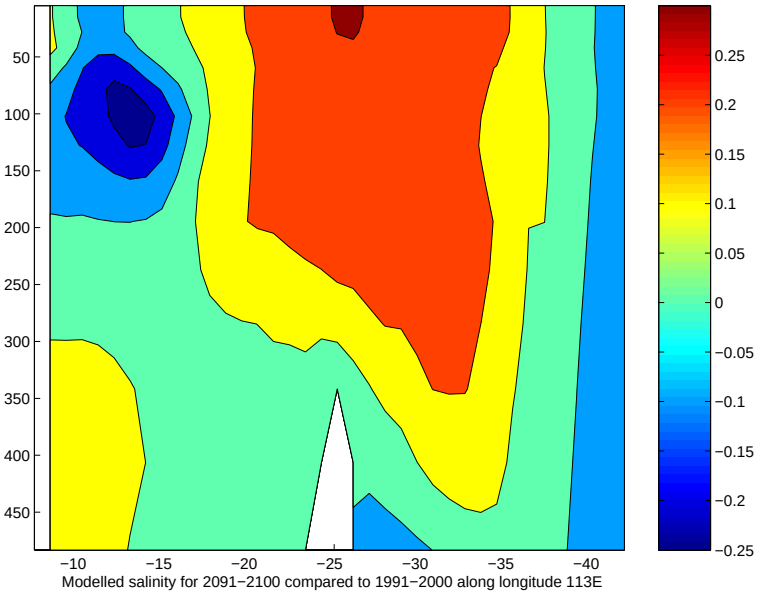

Figure 4.21: Modelled 10-yr mean salinity change for A2100 compared to A2000 along 113^oS

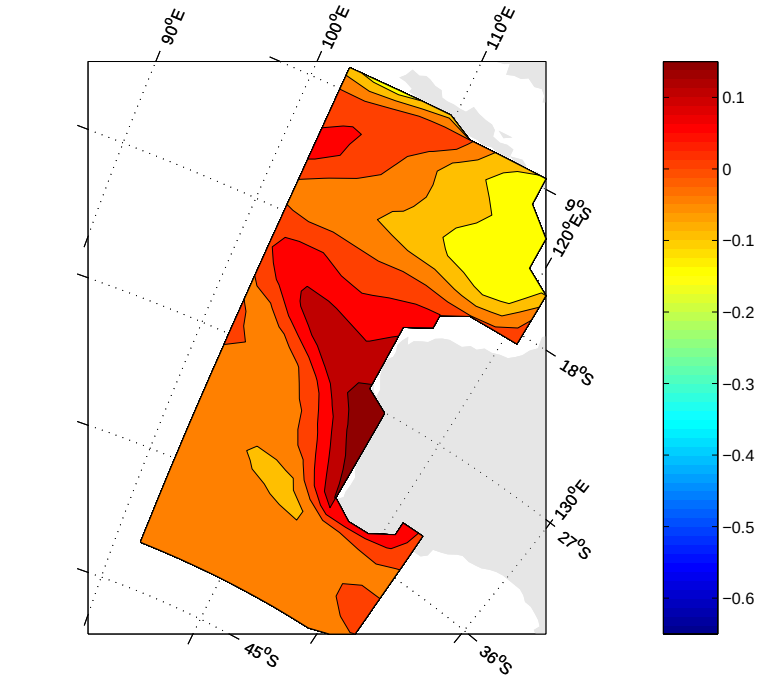

Figure 4.22: Modelled 10-yr mean salinity change for C2070 compared to C2000

ppt for C2070-C2000 and A2070-A2000 respectively. Figure 4.22 and 4.23 illustrate this, surface values indicating changes of between 0.1 to -0.15 *ppt*, associated with a marginal decrease in salinity corresponding to the SEC, and increased associated with the IOCW intrusion. Figure 4.23 relates well with figure 4.22 indicating a slight freshening to the Southern Ocean (-0.05 *ppt*) possibly linked with melting sea-ice (a response to increased atmospheric temperature), and increased salinities (< 0.15 *ppt*) associated with the IOCW intrusion centred from 18 - 34^oS. A subsurface freshening is occurring from 9 - 25^oS indicating change of the order -0.1 *ppt*.

4.2.3 Density

Figure 4.24 illustrates change to surface density (values indicate σ_Θ). Surface density values relate decreased salinity and increased temperature of tropical inflow from the IT and the denser IOCW from the central Indian Ocean (this is represented by figure 4.12 and supported by figure 3.2). In accord with Andrews (1977, 1983) and Church *et al.* (1989),

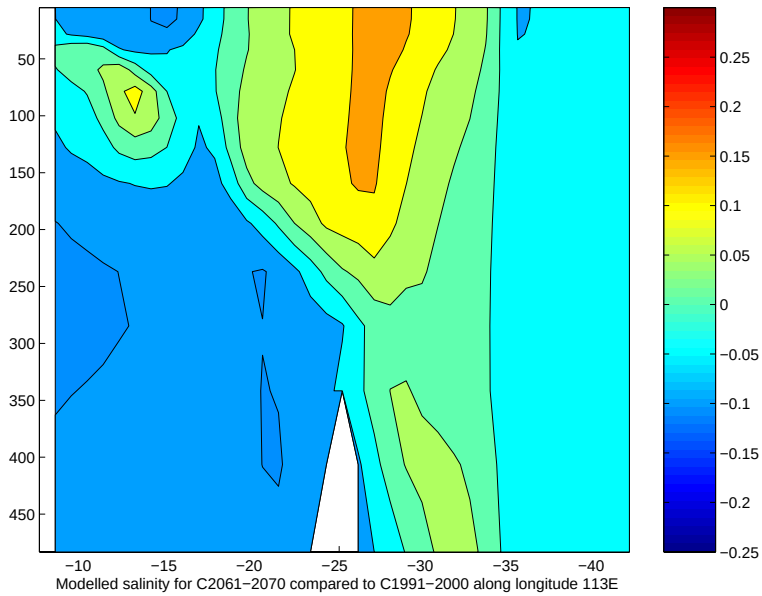

Figure 4.23: Modelled 10-yr mean salinity change for A2070 compared to A2000 along 113^oS

this inflow (IOCW) is centred around 30^oS (25 - 32^oS, 101^oE, figure 4.24).

It is clear from the profile plots that the SEC is the dominant feature for A2070 - A2000 (figure 4.25) and the IOCW dominating figure 4.26 (A2100 - A2000). These features are supported by table 4.9 and 4.10, indicating a decreasing mean (and corresponding minimum values) for A2070 compared to A2000. The situation occurring for A2100 compared to A2000 becomes more complex, with dramatically increased heat content decreasing the density, counteracting the effect of increased salinity water from the more prominent IOCW, leading to fairly constant values A2070 to A2100. This agrees with the work of Batteen and Huang (1998), indicating temperature is the primary determinant of density for the region. Salinity values, however, indicate a more dominant IOCW for this time period, bringing higher salinity water into the regional system. This is clearly indicated by table 4.10 with an order of magnitude change in mean values, from 0.20 (A2070 compared to A2000) to 0.03 (A2100 compared to A2070), supporting the hypothesis that concurrent change to both temperature and salinity are accounting for each other, with almost

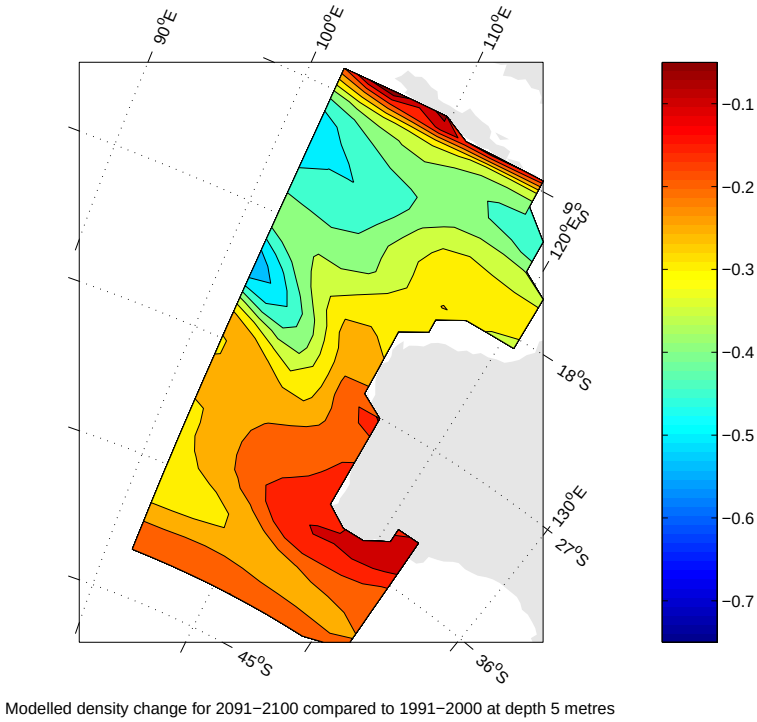

Figure 4.24: Modelled 10-yr mean surface density change for A2100 compared to A2000

constant density values.

The control scenario indicates slightly higher values for density, and less change (decrease, when related to the forced scenario - table 4.10), comparing C2000 to A2000. Fairly constant salinity values are expressed by the control scenario, with marginal (-0.01 *ppt*) decreases between C2070 - C2000. Higher density values then correspond with temperature, -0.23^oC between C2070 - C2000 (a decreasing trend).

Slight changes to surface density are reflected in the control scenario, with values < 0.15 σ_Θ, representing the SEC flow, the remaining area indicating no change to -0.05 σ_Θ decreases (figure not shown). The profile plot (figure 4.27) however, tells a different story. It is clear from this plot, that an increase corresponding to the IOCW is present, this indicating values of 0.1 to < 0.2 σ_Θ. The marginal freshening (for the surface) agrees well with figure 4.27, indicating a decreased density signature of -0.1 σ_Θ. A subsurface feature centred at 25^oS, 300 m depth corresponds with increased temperature (figure 4.18). A

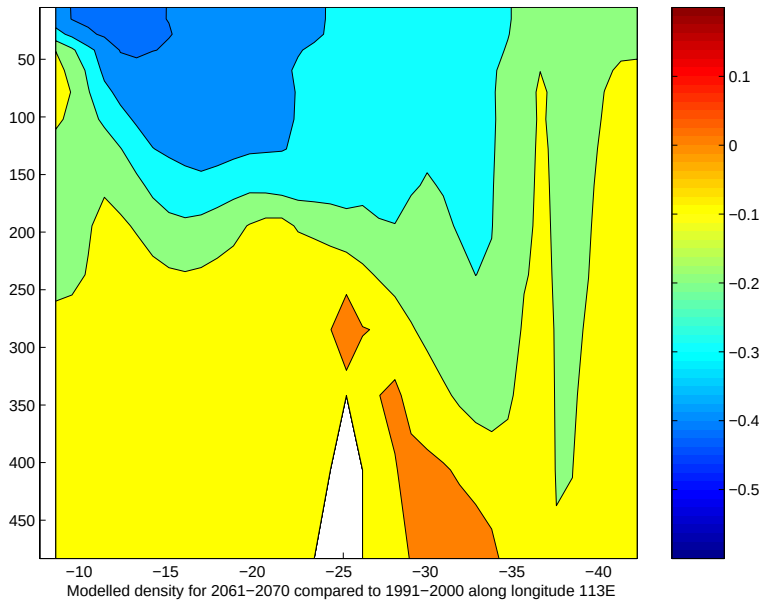

Figure 4.25: Modelled 10-yr mean density change for A2070 compared to A2000 along 113^oS

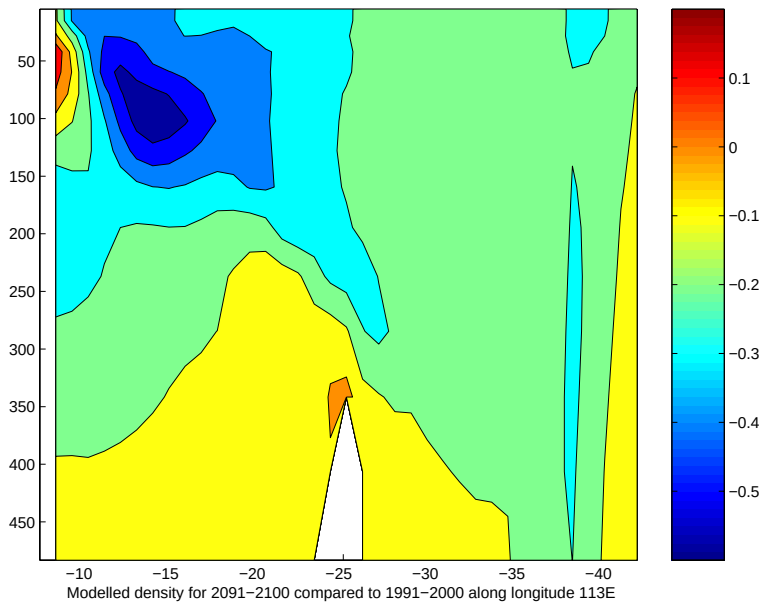

Figure 4.26: Modelled 10-yr mean density change for A2100 compared to A2000 along 113^oS

Dataset	Surface mean	Grand mean	Max	Min	Median	SE
A2000	24.0	25.4	28.1	20.7	26.0	0.028
A2070	23.7	25.2	28.0	20.3	25.8	0.030
A2100	23.7	25.2	28.0	20.4	25.8	0.029
C2000	23.9	25.4	28.2	20.7	26.0	0.029
C2070	23.9	25.4	28.2	20.5	26.1	0.029

Table 4.9: Modelled density values for each of the datasets relating to the top ∼285 m (All values represent σ_Θ)

Dataset comparison	Surface mean	Grand mean	Max	Min	Median	SE
A2070 - A2000	-0.28	-0.20	0.06	-0.69	-0.20	0.002
A2100 - A2000	-0.27	-0.23	0.59	-0.82	-0.20	0.002
A2100 - A2070	0.01	-0.03	0.55	-0.50	-0.04	0.001
C2070 - C2000	0.05	0.04	0.34	-0.38	0.03	0.001

Table 4.10: Modelled changes to density for each of the datasets relating to the top ∼285 m (All values represent σ_Θ)

slight increase to density (0.1 σ_Θ), occurring at 12^oS, 100 m depth refers to an increased salt signature (figure 4.23).

4.2.4 Geopotential Anomaly

Figures 4.28 and 4.29 summarise the steric heights for A2000 and A2100 respectively. The gradient existing between the North West Shelf and Cape Leeuwin is clear from these plots, with a values 0.04 m (A2000) and 0.05 m (A2100), the increase due to a more dominant SEC flow, and the feeder tropical (warm, low-density) IT. This marginally increased alongshore gradient, hypothesised to drive the LC (Andrews, 1983; Godfrey and Ridgeway, 1985; Pearce, 1991; Smith *et al.*, 1991; Thompson, 1984), may suggest increases to LC flow, a response to forcing.

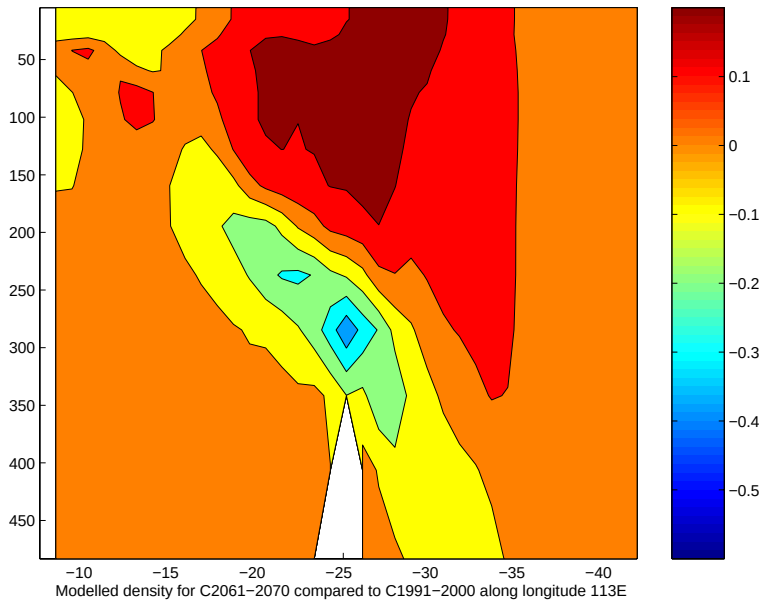

Figure 4.27: Modelled 10-yr mean SST change for A2100 compared to A2000

Thompson (1984, 1987) and Thompson and Veronis (1983) indicated that the presence of the LUC was likely due to a similar steric height gradient at 400 db (400 m). Analysis of the A2000 and Levitus94 datasets indicates that this supposed gradient is not clearly evident. It is possible that this flow may respond to the IOCW inflow, attempting to balance mass by contributing a counter flow beneath this and LC flows.

The C2000 plot replicates the A2000 geopotential anomaly. C2070 essentially replicates C2000, with a slight migration of the gradient increasing to 0.04 m North West Shelf to Cape Leeuwin (0.03 m for C2000). The increased gradient modelled in the forced scenario is likely due to the decreased density flow associated with the IT and SEC in the equatorial region of the study area. This marginally increased gradient may support a strengthened LC flow.

4.2.5 Currents

Figures 3.3, 3.4 and 3.5 have indicated the Mark 3 model resolves present oceanography very well, replicating the five main currents in the study region.

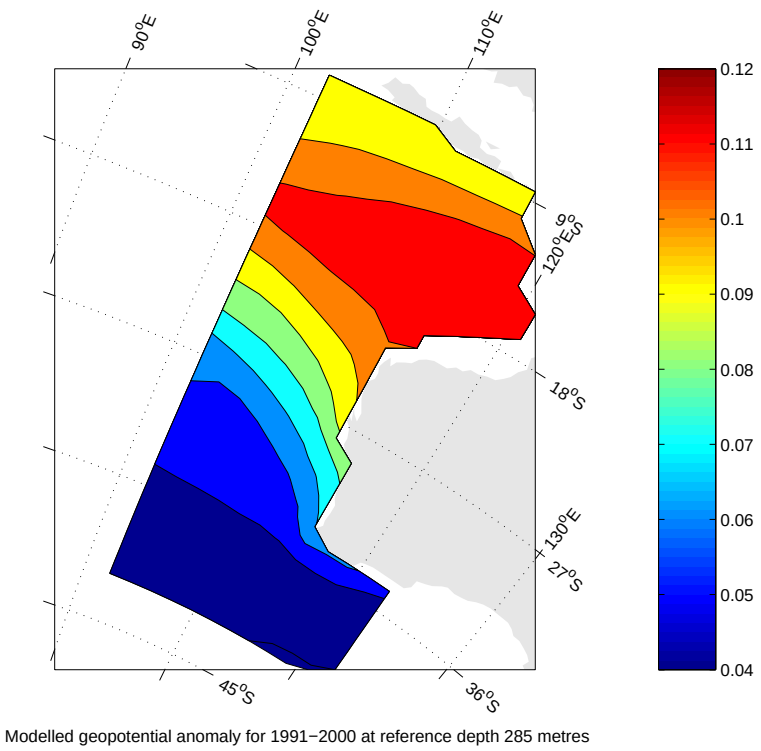

Figure 4.28: Modelled 10-yr mean geopotential anomaly for A2000 for reference depth 285 m

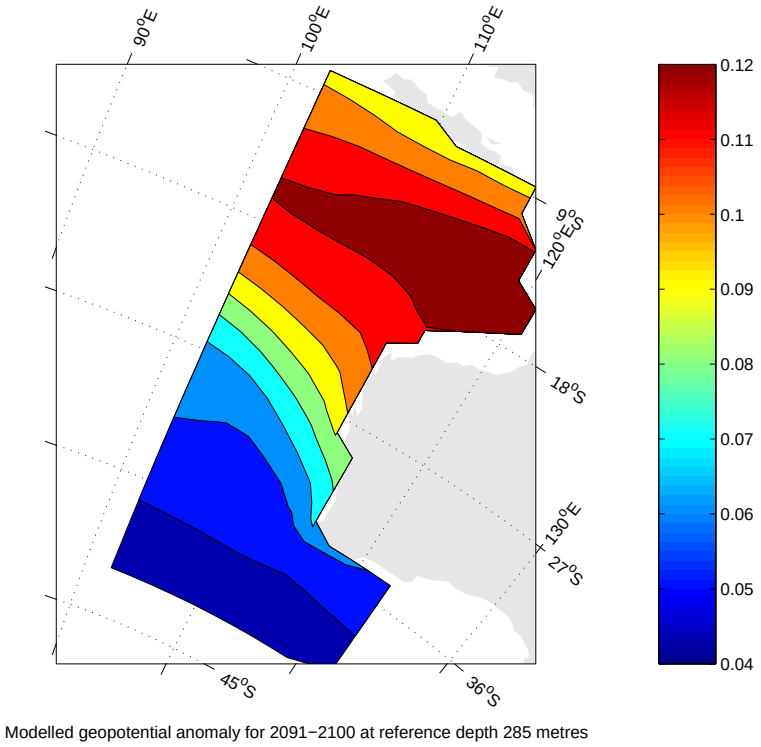

Figure 4.29: Modelled 10-yr mean geopotential anomaly for A2100 for reference depth 285 m

It appears that there is little change to the currents when comparing the plots of A2070 and A2000, however, changes to the dynamic top ∼285 m of the ocean profile is prevalent when reviewing the A2100 - A2000 plots. Figure 4.30 visualises modelled changes to surface currents for A2100 compared to A2000. These plots indicate an increase to the equatorial (8 - 12^oS) component of the SEC, possibly a response to increased windstress at this location. Maximum increases of ∼10 cm s^{-1} are prevalent in the eastern equatorial zone of the study region (8 - 12^oS, 101 - 109°E), with surface mean values exceeding 5 cm s^{-1} for this region. This change is occurring to a depth of ∼60 m. These flows are also supported by the corresponding windstress plot (figure 4.11), with increasing south easterly trades a consequence of changes to the circulation patterns.

The (geostrophic) IOCW inflow appears to be strengthening at the surface, with this flow extending to 102 m depth, relating well to the documented regime. A maximum value of 5 cm s^{-1}, occurring along the most western portion of the study region(23^oS, 99^oE). This may suggest a geostrophic response to the decreased density of regional oceanography, the IOCW inflow (a source of more saline, denser water), attempting to balance for decreased density of the region, supported by table 4.9 and 4.10.

A decreasing westerly current is apparent in the south-western portion of the study area (35 - 39^oS, 106 - 122^oE) indicating the combined ACC/WAC, with mean decreases of ∼5 cm s^{-1}). This feature closely reflects the decrease to windstress at this latitude, decreasing wind-driven current flow due to changes to the circulation pattern.

Datasets for the control run only allowed comparison between C2070 and C2000. Corresponding with the A2070 and A2000 plots, only very slight changes are indicated. Figure 4.33 summarises the most obvious changes to the oceanography for C2070 compared to C2000. It is clear from this plot that there are slight decreases occurring to the IOCW and continued flow south of Cape Leeuwin ([35^oS] combined with LC flow at this location).

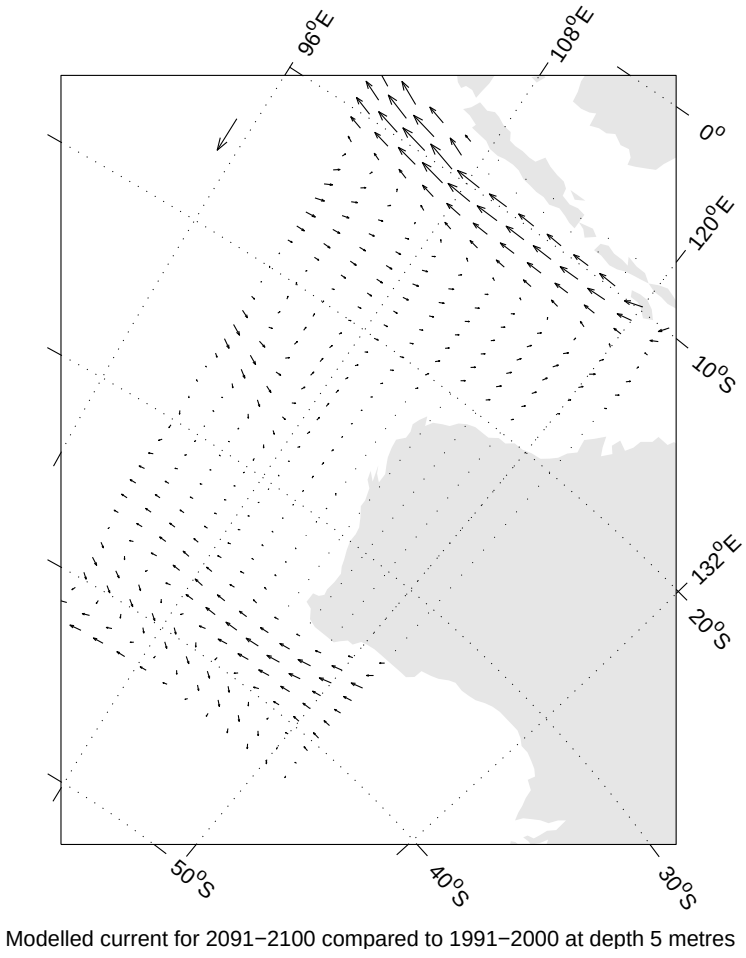

Figure 4.30: Modelled 10-yr mean surface currents change for A2100 compared to A2000

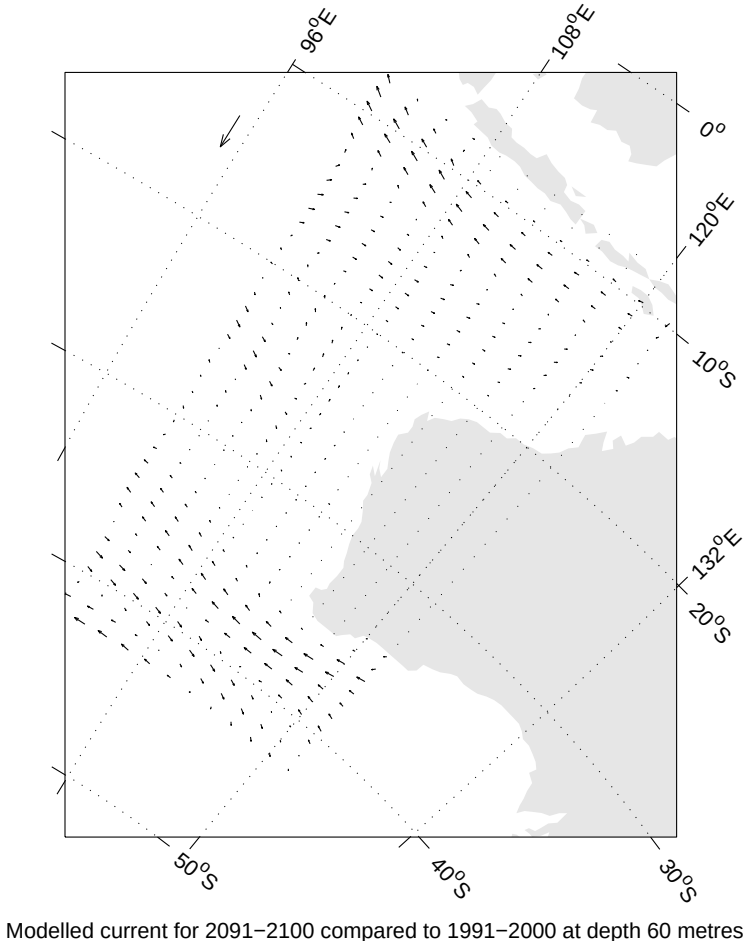

Figure 4.31: Modelled 10-yr mean currents change for A2100 compared to A2000 at 60 m depth

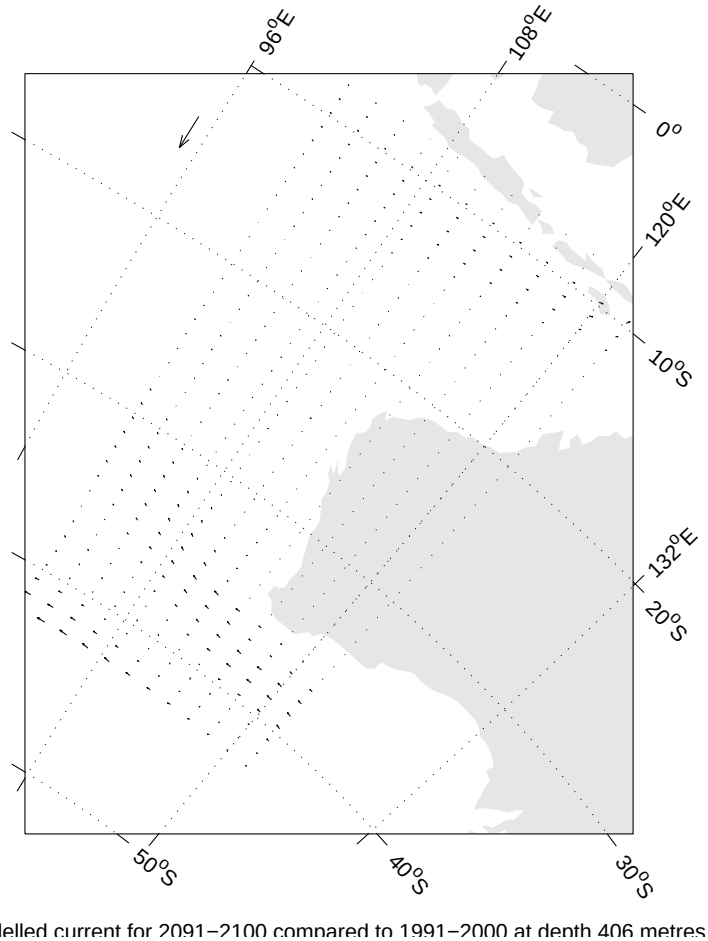

Figure 4.32: Modelled 10-yr mean currents change for A2100 compared to A2000 at 406 m depth

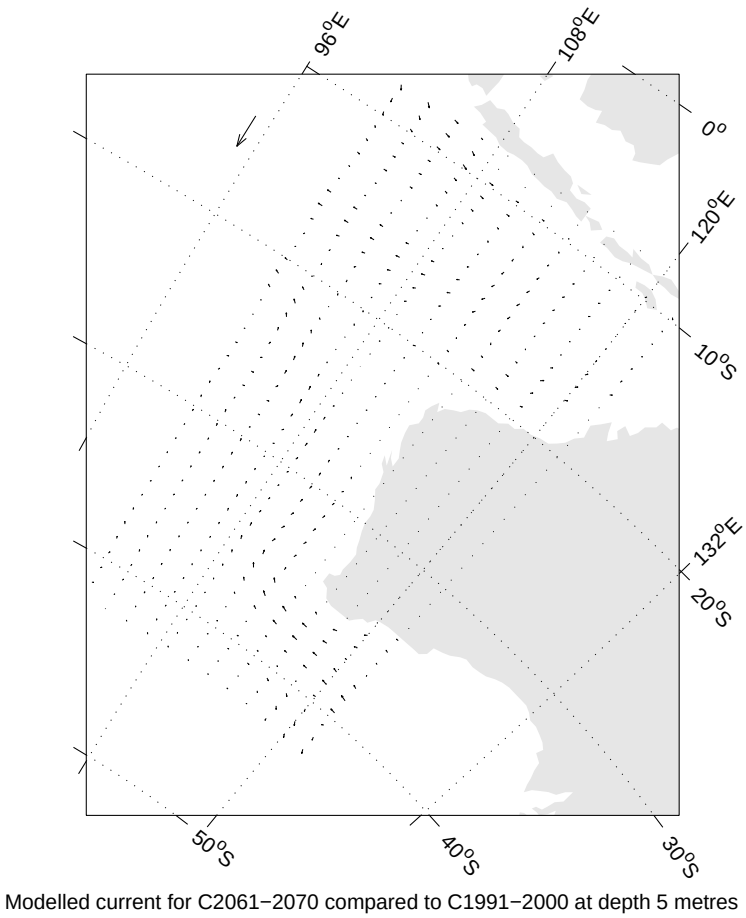

Figure 4.33: Modelled 10-yr mean surface currents change for C2070 compared to C2000

It is likely then too, that the LC flow is decreasing in the control run, indicated by very marginal (< 0.2 cm s^{-1}) decreases extending from 28 - 35°s, conflicting with the increased alongshore gradient expressed by the geopotential anomaly.

Plots of corresponding depths (to the A2 scenario, 60 and 406 m) indicate changes of lesser magnitude than figure 4.33, and for this reason are not included. The lack of a C2100 dataset has not allowed a direct comparisons to be made, the C2070 (similar to the A2 scenario) indicating slight changes.

4.2.6 Volume Transports

Figure 4.34 indicates the most dominant flows to be the combined IT and (extension to form the) SEC. The (geostrophic) IOCW and the LUC, are both indicated through high

transport values suggested around the southern capes (possible LC entraining IOCW), extending into the central Indian Ocean (15 - 30^oS). These are indicated by representative values of 1 - 2 Sv, extending from $\sim$20^oS (101^oE) to beneath Cape Leeuwin ($\sim$35^oS, 120^oE).

Table 4.11 summarises change to transports for each of the datasets. Transport values calculated for this table relate to both the meridional (along-shore) and zonal (cross-shore) components for the IT, SEC and IOCW with meridional component only calculated for the LCS.

It is clear from values calculated for each of the datasets that a considerable decrease to most flows is occurring, with an increase suggested for IOCW transport (table 4.11). It is interesting when reviewing the surface current change plot (figure 4.30) that a slight increase of the order of 4 cm s^{-1} is occurring in the zone of greatest transport (9.8^oS, 121.9^oE), linked with surface flow of the IT. This increase is occurring only in the top portion of the IT region, with possible decreases at depth linking to the decreased transport value. Slight decreases (of the order $\sim$2 cm s^{-1}) are suggested from 12.6 - 15.4^oS, 121.9^oE, the feeder flow that sets up the LC through the LCS.

The control scenario indicates similar trends to the forced scenario. A general decreasing trend is apparent for all flows apart from the IOCW, this flow becoming more dominant. This value agrees well with the temperature plots, indicating a more stratified ocean, and corresponding decreases to the global THC expressed through the IT calculation.

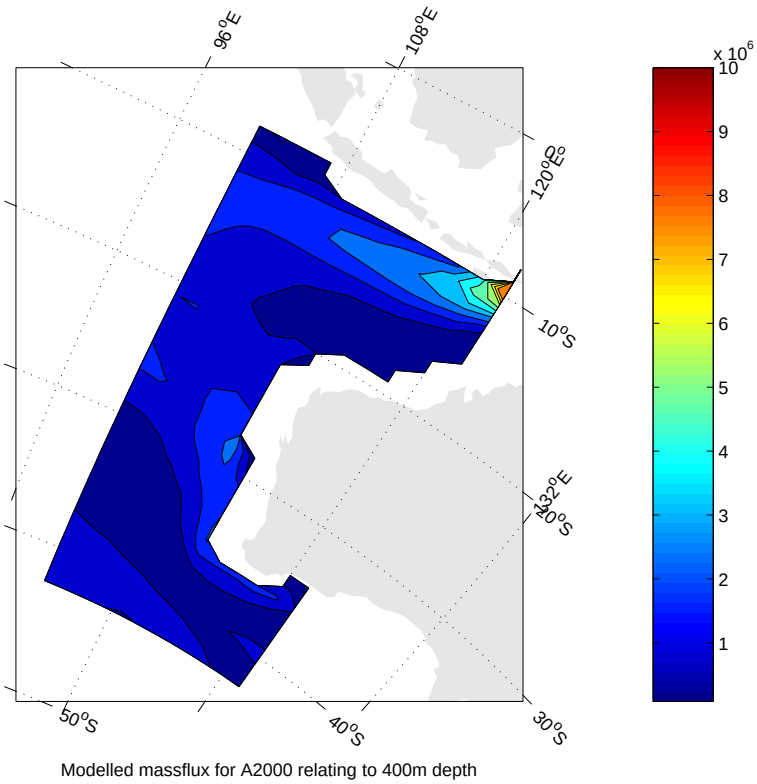

Figure 4.34: Modelled 10-yr mean transport for A2000

Dataset	IT	SEC	LCS	IOCW
A2000	12.71	17.18	0.28	6.19
A2070	12.45	17.06	0.21	6.32
A2100	12.20	16.03	0.16	6.34
C2000	12.76	17.49	0.30	7.04
C2070	12.69	17.40	0.22	6.93

Table 4.11: Modelled current transports for each of the datasets
(All values indicate flows in Sverdrups (10^6 m^3 s^{-1})

4.2.7 Surface Fluxes

4.2.7.1 Heat flux

Driven by the temperature gradient between the SST and lowest atmospheric layers, negative values indicate a heat loss from the ocean to the atmosphere, positive values indicating the opposite. Figure 4.35 indicates the surface heat flux for A2000. The general trend is for increasing heat flux into the ocean (positive values) for A2000 through A2100.

Figure 4.35 indicates greater flux (loss) from the ocean associated with the warm low to mid latitudes (13 - 27^oS), intensifying alongshore (18 - 36^oS), corresponding with high SST attributable to LC flow. Southern Ocean values (south of 36^oS) suggest flux (gains) to the ocean from the atmosphere, indicating the ocean is far cooler than the atmosphere, fluxes attempting to balance heat.

Changes are relatively small when compared to large flux values for each of the datasets. Table 4.12 suggests a trend of decreased fluxes from the ocean, indicated by increased mean values (values becoming more positive [gain]). Minimum and median values for each of the datasets (table 4.12), indicate slight alterations to this general pattern, with decreases to maximum loss values, the ocean storing more advected heat, this clear relating to temperature analysis (tables 4.4 and 4.6).

Grand mean calculations indicate that a significant decrease to heatflux from the ocean occurs between A2070 to A2100, with mean decreases from -9.79 to -5.06 $W\ m^{-2}$. A corresponding increase in heat flux into the ocean is represented by maximum values, indicating a 20% increase occurs between A2070 - A2000, with a 70% increase for A2100 - A2000. The opposite pattern is suggested in the control scenario, with a 12% decrease C2070 - C2000 (table 4.12). These values support the hypothesis that increased mean temperature of the ocean is due to increased flux from the (increased temperature) atmosphere (Houghton *et al.*, 2001).

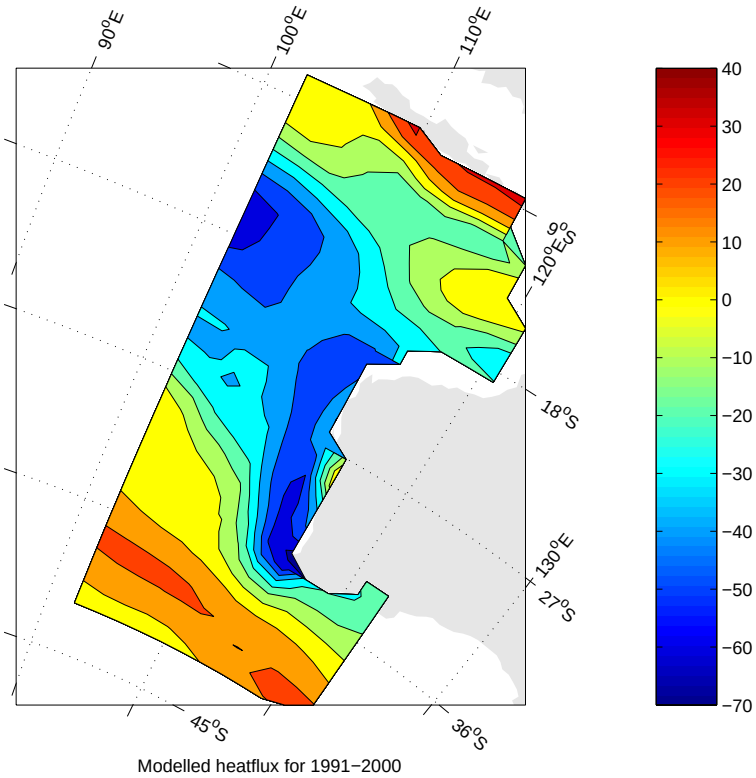

Figure 4.35: Modelled 10-yr mean surface heat flux for A2000 (All values represent $W\ m^{-2}$)

A2070 values indicate that fluxes from (loss) the ocean are increasing only slightly, the increased median value supporting this theory. A significant drop occurs by A2100 (-7.91 compared to -2.8 $W\ m{-}2$ - A2070 to A2100), possibly suggesting that atmospheric temperatures have risen, driving increased advection, contributing to oceanic heat content. The opposite pattern is apparent for the control dataset, indicated by table 4.12.

Figures 4.36 and 4.37 summarise changes to the surface heat flux for A2070-A2000 and A2100-A2000 respectively. These plots indicate a marked increase in heat flux from the atmosphere for A2070 to A2100, associated closely with the high SST off the North West Shelf. This feature becomes clearer when reviewing the summary included in table 4.12. It is most clear in figure 4.36, a close coupling occurring between areas of increased SST (figure 4.12) and increased flux from the ocean (negative values, also supported by figure 4.35 suggest greater losses linked with high SST).

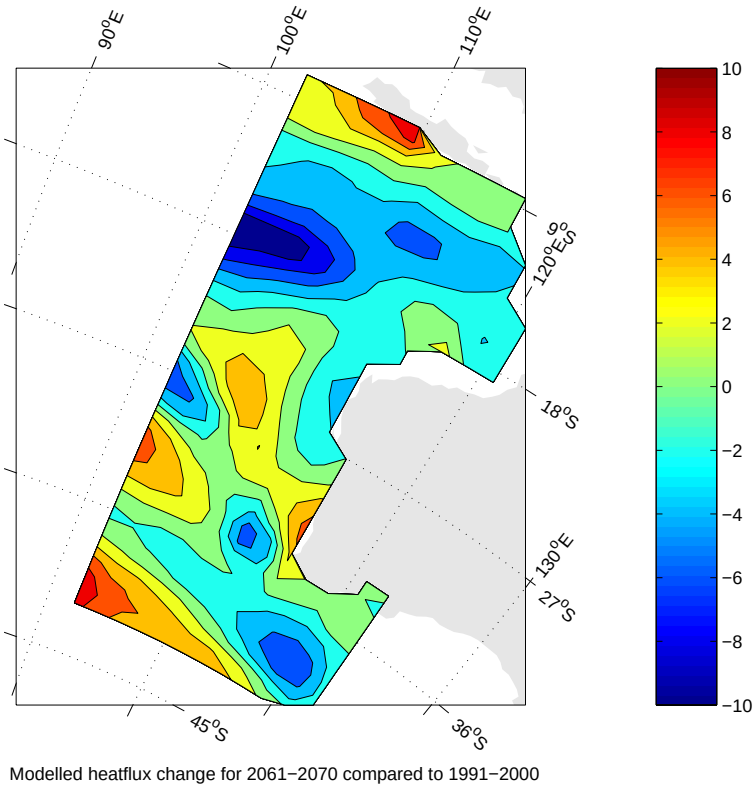

Figure 4.36: Modelled 10-yr mean surface heat flux change for A2070 compared to A2000 (All values represent $W\ m^{-2}$)

Summary values included in table 4.12 suggest that heating associated with the top ∼285 m of the profile is due chiefly to increased flux transport from the atmosphere for the period A2000 to A2070 (represented by marked increases to the maximum values and much smaller increases to the minimum values). Using similar logic then - analysis of values relating to the A2100 dataset indicate no change to maximum temperature (maximum value of 29.9), and this would correspond to a distribution of heat through advection into the deeper waters that are not directly affected by the surface ocean-atmosphere heat flux.

The control run indicates a slight increase to fluxes from the ocean, values agreeing well with areas of higher SST (figure 4.17). When comparison is made between figures 4.36 and 4.38, it is clear that far greater loss is modelled for the control run, possibly tied to decreased atmospheric temperatures (or constant atmospheric temperatures) when compared to predicted increased for atmospheric temperatures (Houghton *et al.*, 2001).

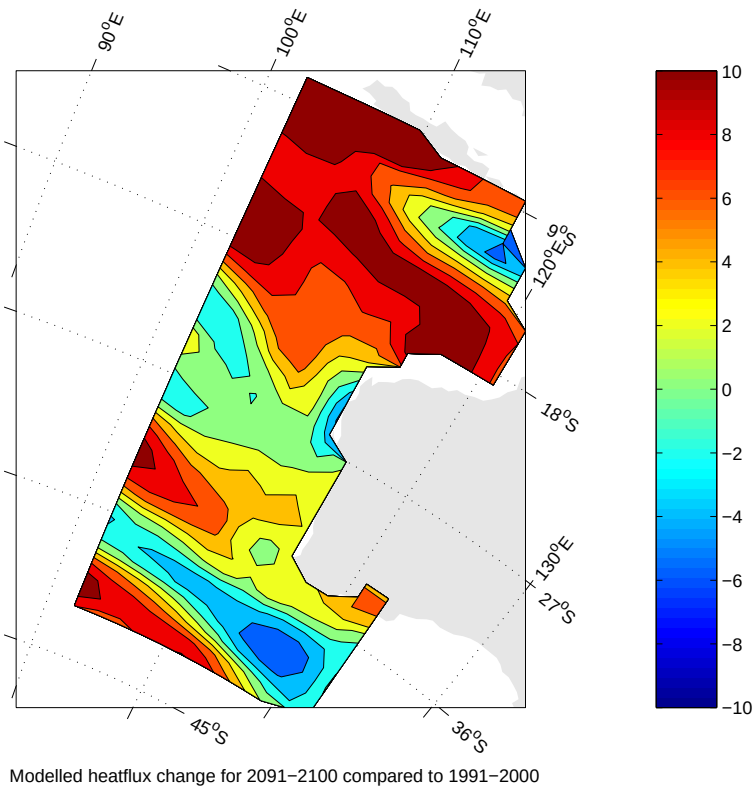

Figure 4.37: Modelled 10-yr mean surface heat flux change for A2100 compared to A2000 (All values represent $W\ m^{-2}$)

Dataset	Grand mean	Max	Min	Median	SE
A2000	-9.95	36.56	-63.01	-6.54	1.169
A2070	-9.79	44.50	-64.16	-7.91	1.235
A2100	-5.06	62.62	-60.43	-2.8	1.178
C2000	-11.24	36.17	-60.97	-9.68	1.18
C2070	-13.14	32.24	-62.54	-11.13	1.185

Table 4.12: Modelled surface heat flux for each of the datasets (All values represent $W\ m^{-2}$)

Dataset comparison	Grand mean	Max	Min	Median	SE
A2070 - A2000	0.163	9.768	-9.740	-0.056	0.173
A2100 - A2000	4.891	26.892	-5.752	4.550	0.268
A2100 - A2070	4.727	22.960	-5.780	3.590	0.286
C2070 - C2000	-1.899	7.229	-11.369	-1.447	0.149

Table 4.13: Modelled changes to surface heat flux for each of the datasets (All values represent $W\ m^{-2}$)

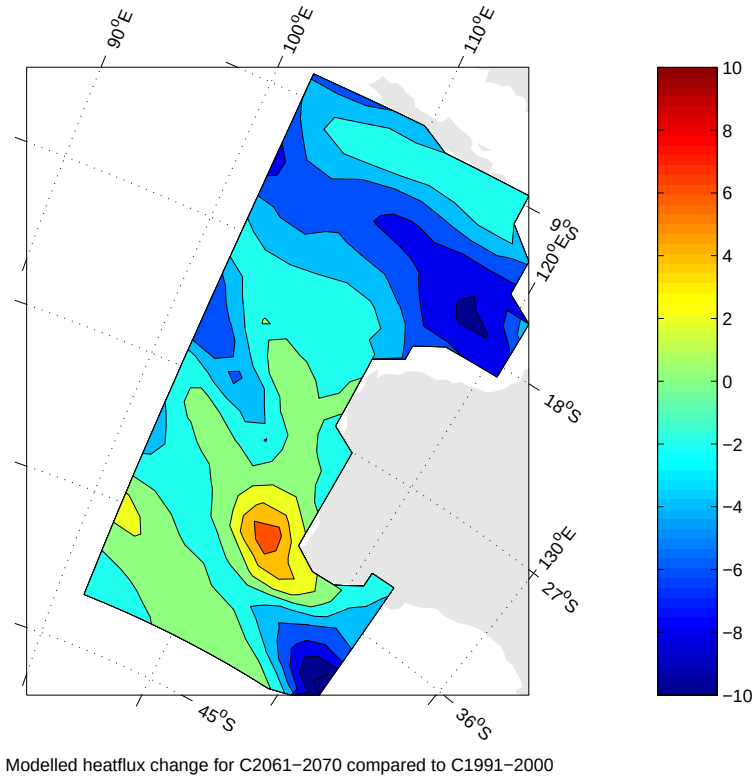

Figure 4.38: Modelled 10-yr mean surface heat flux change for C2070 compared to C2000 (All values represent $W\ m^{-2}$)

C2070 and C2000 datasets were the only control scenario datasets available for analysis, for this reason comparison between these and the A2100 is not possible, however it is likely that the trend indicated by C2070 - C2000 would continue, conflicting with the forced scenario output.

4.2.7.2 Freshwater Flux

Freshwater flux is representative of precipitation minus evaporation, positive values indicating precipitation (freshwater input), negative values evaporation (freshwater export). Figure 4.39 indicates modelled freshwater flux for the A2000 dataset. The general trend is for decreased freshwater input, corresponding with increased evaporation.

It is clear from this dataset (A2000) that greatest loss is associated with central ocean low to mid-latitudes, linked to higher SST, and increased evaporation. The LC in

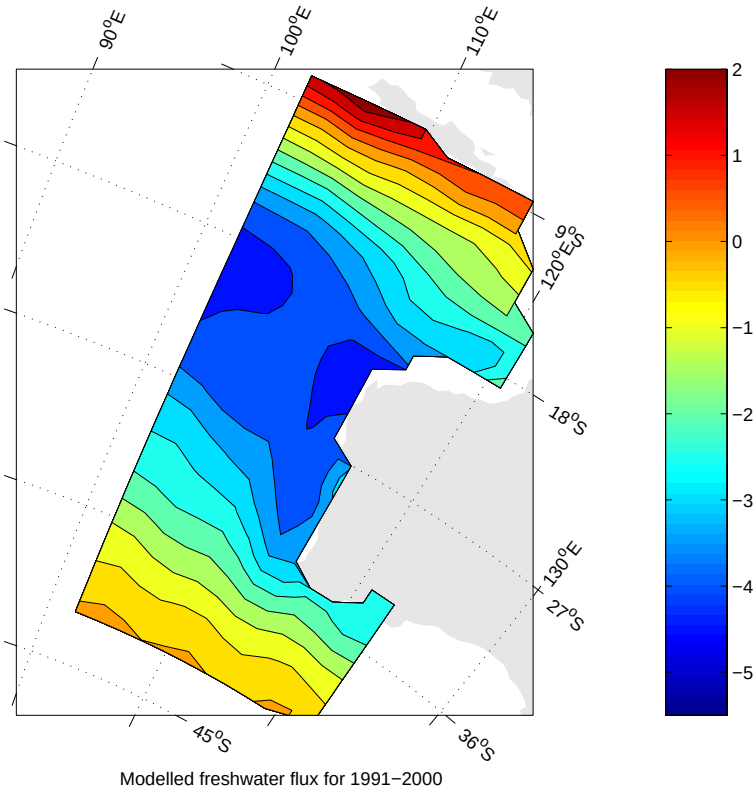

Figure 4.39: Modelled 10-yr mean freshwater flux for A2000 (Values indicate $mm\ day^{-1}$)

this example leads to increased evaporation, indicated by strong negative values. Maximum values correspond to tropical Indonesia, this location indicating positive values (precipitation), peaking at 2 $mm\ day^{-1}$ in the top western corner of the study region (7.5^oS, 107^oE).

Figure 4.40 and table 4.14 indicate the change to surface freshwater fluxes. It is clear from table 4.14 that a significant decrease to precipitation (and corresponding increased evaporation) is occurring over the time period. Revision of the comparative maximum values indicate a order of magnitude change, with a decrease to less than a third of the A2000 value when comparing A2100. A standard error 0.0765 for the A2100 dataset also indicates that a decrease in variation is occurring, with a strong negative tendency around the mean value of -2.36 likely.

An alternate trend is present in the control datasets. These indicate a decrease to

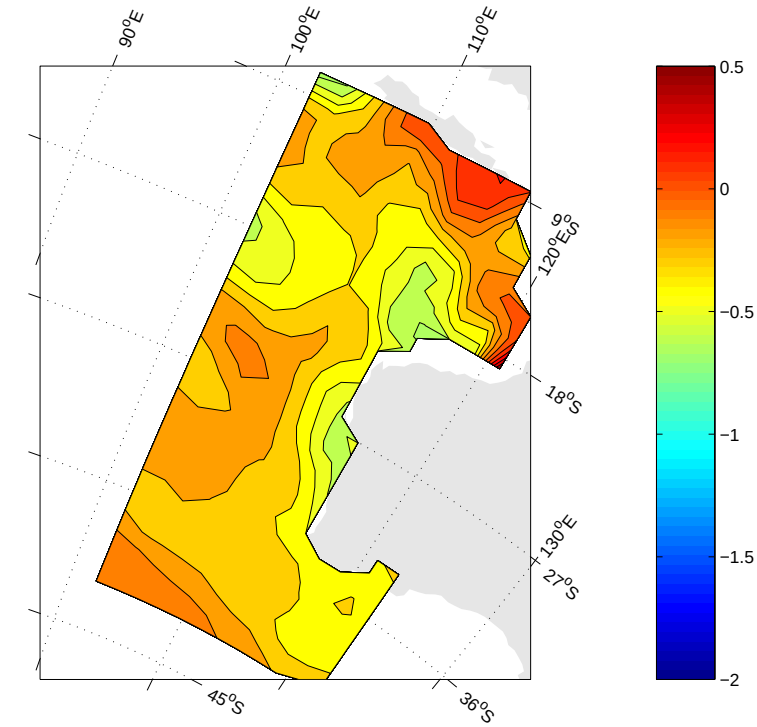

Figure 4.40: Modelled 10-yr mean freshwater flux change for A2070 compared to A2000 (Values indicate $mm\ day^{-1}$)

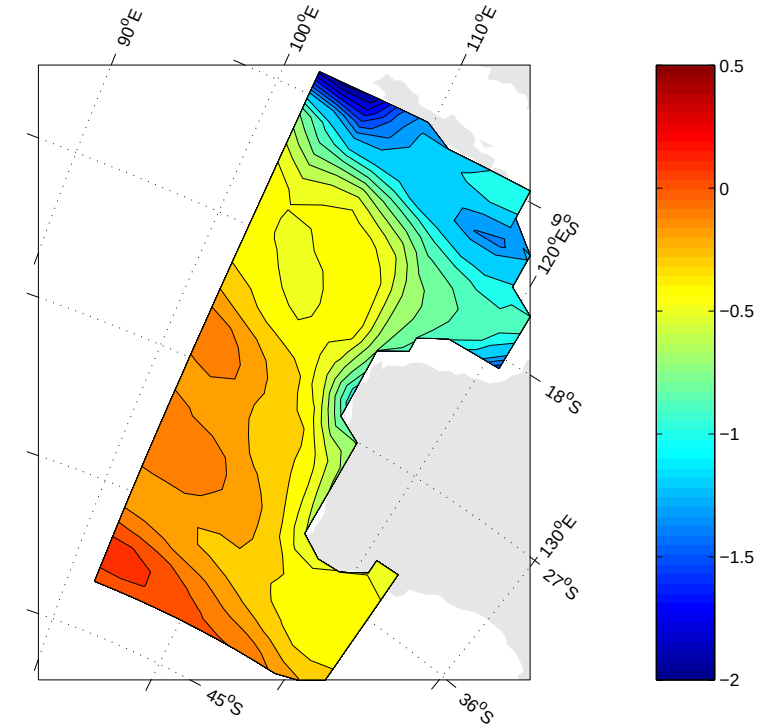

Figure 4.41: Modelled 10-yr mean freshwater flux change for A2100 compared to A2000 (Values indicate $mm\ day^{-1}$)

Dataset	Grand mean	Max	Min	Median	SE
A2000	-1.87	2.46	-4.36	-1.87	0.0816
A2070	-2.10	2.16	-4.69	-2.17	0.0859
A2100	-2.36	0.71	-5.11	-2.41	0.0765
C2000	-1.80	2.40	-4.48	-1.88	0.0905
C2070	-1.75	2.76	-4.64	-1.86	0.0955

Table 4.14: Modelled surface freshwater flux for each of the datasets (All values represent $mm\ day^{-1}$)

Dataset comparison	Grand mean	Max	Min	Median	SE
A2070 - A2000	-0.227	1.459	-0.663	-0.230	0.009
A2100 - A2000	-0.482	0.143	-1.954	-0.366	0.021
A2100 - A2070	-0.254	0.204	-2.986	-0.051	0.024
C2070 - C2000	0.053	0.961	-0.29	-0.003	0.01

Table 4.15: Modelled changes to surface freshwater flux for each of the datasets (All values represent $mm\ day^{-1}$)

evaporation, possibly linked to predicted decreasing atmospheric temperatures (Houghton *et al.*, 2001). Figure 4.42 indicates very subtle changes, the mean value for this analysis indicating 0.053 $mm\ day^{-1}$, a very small change when relating to values for each of the individual datasets (table 4.14).

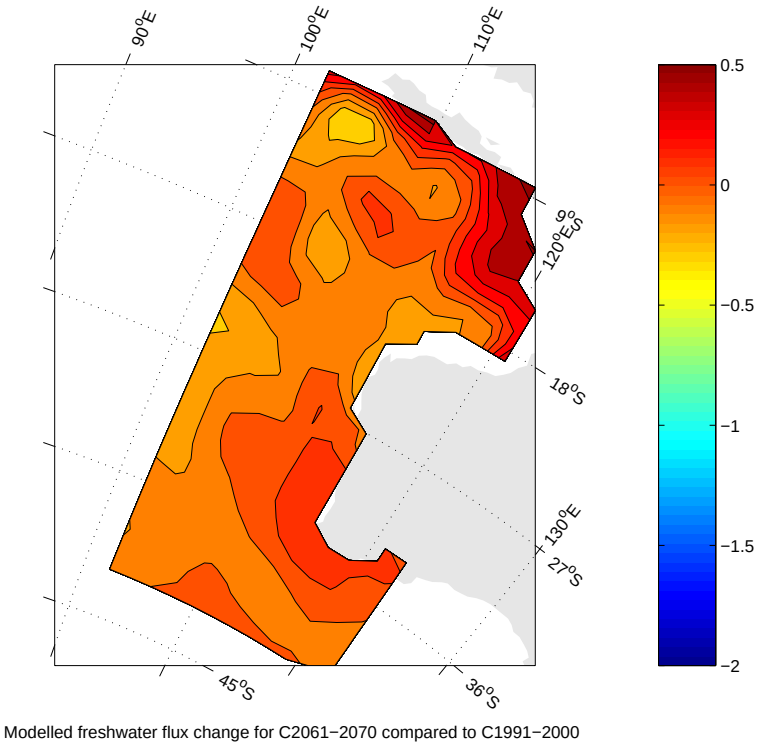

Figure 4.42: Modelled 10-yr mean surface freshwater flux change for C2070 compared to C2000 (Values indicate $mm\ day^{-1}$)

CHAPTER 5
DISCUSSION

The results presented in the previous chapter illustrate the response of Western Australian Regional Oceanography to increased CO_2 forcing as represented by the CSIRO Mark 3 AOGCM.

Early models incorporating increased CO_2 forcing, suggested changes to the upper (<1000 m) layer of the oceans, producing significant (2 - 4^oC) increases to temperature at these levels (Bernal, 1991). Recent advancements, including more optimised parameterisations, increases to model resolution, improvements made to atmospheric composition changes (calculated from the emission scenarios), and the application of climate models for this task, provide more realistic replication of real climate systems (Wigley and Raper, 2002), resulting in better replication of regional features.

Output from the Mark 3 ocean model (simulating the A2 scenario), relate well with work on global (and regional) climate change, with realistic outputs when compared against other international climate models, and recent observations (Houghton *et al.*, 2001). Results indicate increases to SST (and subsurface temperature), changing salt distribution of the oceans, inferred changes to the global THC (attributable to changing density gradients [Bi *et al.*, 2001; Cai and Gordon, 1998,1999; and Matear and Hirst, 1999]) and corresponding changes to ocean-atmosphere fluxes, linking these dynamic systems together.

The intrinsically coupled nature of the climate system ensures each variable links, either directly or indirectly, to every other. An example of this: increased heat flux into the ocean due to increased mean atmospheric temperatures, the system attempting to attain mass and energy balance, transporting heat through surface (and subsurface) transport

and fluxes. Driven by the equilibrium balance of mass and energy, geostrophic transports attempt to balance these across the globe.

The IT, a key geostrophic current, attempts to balance the global system. This flow is responsible for a large component of the heat and freshwater balance of the Indian Ocean (Shneider, 1998; Schiller *et al.*, 1998), transporting tropical water from the North Pacific. Transport estimates ranging from 26 to -10 Sv (Fieux *et al.*, 1996), and representative mean flows of $\sim$7 Sv (Meyers, 1996), with associated heat transports of 1.45 $\pm$ 0.3 PW, indicate one of the largest heat transports of the global ocean system (Macdonald, 1998), this feature a choke-point for global circulation (Broecker, 1991; Gordon, 1986).

5.1 Caveat

It is convention to correct model output for climate (or model) drift. This is achieved by running a corresponding control run, indicating climate (temporal or model) drift over the period assessed. These values are then used for reference against forced scenario runs, enabling correction of the scenario output for climate drift, the resulting output, limited to the effect of forcing only (Banks and Woods, 2002). While control-run correction will only subtly effect scenario output (Dr Tony Hirst *Pers. Comm.* CSIRO - DAR, 21-10-02), it may significantly alter mean calculations, possibly magnifying subtle changes.

The lack of a control dataset for the ocean component of 2100 (C2100) did not allow for correction for the corresponding forced dataset (A2100). This was due to the control scenario having not been run to completion, hitting significant problems in the early stages, subsequently stopped prior to completion (Dr Tony Hirst *Pers. Comm.* CSIRO DAR, 21-10-01). The forced (A2 scenario) and control runs therefore, have been analysed separately, with an attempt to infer predicted climate drift from the available C2000 and C2070 runs. The nature of the forced scenario would indicate as far as A2100 is concerned, a climate

change signal becoming very large, dwarfing climate (model) drift (Dr Tony Hirst *Pers. Comm.* CSIRO - DAR, 21-10-02).

The limited spatial extent of the study region, and the global linkages that are present within both oceanic and atmospheric circulation, ensure changing regional oceanography cannot be accounted for completely within the dataset. In order to explain some of these changes, reference to suggested global-scale change must be undertaken.

5.2 Key variables reflecting changing patterns to climate

Barnett *et al.* (1999) indicate that current methods focus almost exclusively on the SST of the ocean for detection of anthropogenic climate change. It is likely that detection of a changing climate is closely linked to the heat content of oceans, represented in both SST and subsurface values (Levitus *et al.*, 2001; Barnett *et al.*, 2001), with the Mark 3 model suggesting considerable changes to regional oceanography in response to CO_2 forcing.

Banks and Wood (2002) have attempted to isolate key features from AOGCM ocean model output, linking changing oceans to anthropogenic climate change. They concluded that subsurface temperature and salinity have the potential for detecting anthropogenic change over just 30 years.

For the Mark 3 output, temperature and salinity were the most representative of changes for regional oceanography, agreeing with Banks and Wood (2002).

5.2.1 Temperature

Tables 4.4 and 4.6, and figures 4.12 to 4.18 indicate changes to both the forced and control scenario temperatures. The most prominent change is expressed in the heat content (represented by increased mean temperature) of this region. It is clear from the forced scenario that considerable increases to surface temperatures are taking place (figures 4.12

and 4.13, tables 4.4 and 4.6), with corresponding grand mean increases of 0.6 and 1.1^oC for A2070 and A2100 respectively (relative to A2000). Subsurface values (figures 4.14, 4.15 and table 4.6), suggest increases of a greater magnitude at depth. Cai and Gordon (1998) reported that previous runs of the Mark 2 AOGCM also indicated maximum heating in the subsurface, suggesting greater stratification occurring in the upper ocean. This stratification is linked to decreases in the global THC (driven by geostrophic flows, dependent on an unstratified ocean), represented by large-scale oceanic currents. Clark *et al.* (2002) support the conclusions of Cai and Gordon (1998), suggesting that due to increased CO_2 forcing, decreased Atlantic (NADWF) and Antarctic (AABWF) overturning (corresponding to decreased [or a shutdown of the] THC) could result. Banks and Wood (2002) indicate that continuous time-series are more appropriate to determine collapse of the THC. The inherent variability (drift) in models may lead to incorrect conclusions, drawn from snapshot datasets. With small changes possibly representing decadal (or longer) signals, not attributable to anthropogenic climate change.

Calculated values relating the the heat transport attributable to the IT (North Pacific - Indian Ocean) indicate this flux to be virtually constant, (changes <0.1% are indicated over the 100-yr model run), supporting the concept of increased ocean temperatures attributable to increased heat flux from the atmosphere. Analysis of the summary values contained in table 4.4 and 4.6 support the hypothesis that heating is attributable to increasing heat flux from the atmosphere. Increased heat flux to the ocean is indicated by table 4.12 and 4.13, corroborating with this hypothesis, and the increased heat content of the ocean profile. This agrees well with the IPCC summaries, predicting a considerable increase to global temperatures, 1.4 - 5.8^oC by 2100, possibly driving heat flux increase (Houghton *et al.*, 2001).

Revision of the control run output indicates a decreased temperature trend C2000 to

C2070. The corresponding A2000 to A2070 dataset indicates a marked increased trend. These results may indicate that the forced runs are underestimating heating, a response to forcing. Incorporating the variability suggested by the control run, into the forced output, indicates considerably greater increases to heat are attributable to increased forcing. A simple calculation may suggest that the true heat increase due to CO_2 forcing is 0.8^oC (0.6 - [-0.2], A2070-A2000 change subtract variability indicated by the C2070-C2000 run, table 4.6), a 25% (0.8^oC compared to 0.6^oC) increase compared to the forced scenario in isolation.

5.2.2 Salinity

Tables 4.7 and 4.8, and figures 4.19 to 4.23 indicate changes to both the forced and control ocean salinities. Changes to mean salinity (top ~285 m) for the forced scenarios indicate a dynamic system operating over the 100-years of data. A freshening occurs over the period A2000 - A2070, attributable to (decreased salinity) SEC flow, with an increase indicated for A2100 - A2000 attributable to increasing IOCW (agreeing with changes to currents and transport values, figure 4.30 and table 4.11). CO_2 forcing is likely to be the cause of the decreased salinity signature present in the A2000 dataset, when comparison is made to Levitus94 profiles (Dr Tony Hirst *Pers. Comm.* CSIRO - DAR, 21-10-02). The greatest freshening is associated with the IT and continued SEC flows, possibly linked to freshening of the northern Pacific Ocean (suggesting high-latitude freshening), a response to forcing.

Amplified salinity values, are attributable to a more dominant IOCW flow. The origin of this flow is currently unknown, however, reflects salinities from the central Indian Ocean. The more dominant nature of this flow is indicated by mean values expressed in tables 4.7 and 4.8. Increasing salinities also agree with the freshwater flux plots, indicating increased

evaporation off the ocean surface. Cai and Gordon (1998) reported that forced runs (of the Mark 2 CSIRO AOGCM) indicated a decrease in the large scale oceanic currents which have a significant thermohaline driven component. The reduction in these currents reduces the poleward transport of salt out of the tropical and subtropical regions of these oceans. This and enhanced evaporation contribute to increases in surface salinity in the tropical and subtropical regions.

Control run output indicates lower initial (C2000 compared to A2000) salinity values. There appears to be little change (-0.01 *ppt*) to the control output with constant surface and grand mean values obtained over C2000 to C2070. Increased values for the forced runs may link to increased evaporation off the ocean surface (Cai and Gordon, 1998), indicated by decreasing freshwater flux (evaporation), the control scenario indicating slight increases (table 4.8).

5.2.3 Density

Density changes are a complicated mix of temperature and salinity responses to forcing. Work by Batteen and Huang (1998) have indicated that the primary determinant for density is temperature in this region. The tendency A2000 to A2100 is for a mean increase to salinity, due to a more dominant IOCW intrusion, confused with corresponding increases to heat content, indicating decreased density values.

It appears that there is a clear pattern in the comparative density datasets. A decrease from A2000 to A2070 is linked to decreased salinity (IT/SEC) and increased temperatures due to greater heat flux from the atmosphere. Decreases from A2000 to A2100 are chiefly due to increased heat content, however this is moderated by a more dominant IOCW intrusion bringing saltier water from the central (and lower) Indian Ocean.

Control run output indicates lower initial (C2000 compared to A2000) density values

(23.9 compared to 24.0 σ_Θ). There appears to be little change to the control output with constant surface and grand mean values obtained over C2000 to C2070. Decreased values for the forced runs may link directly with the considerable increase to heat content of the profile, indicated by SST (and subsurface) temperature increase. Greater heat content overrides the more dominant nature of the IOCW, bringing denser, saltier water into the region.

Studies reviewing the output of AOGCM's indicate that decreasing density (increasing ocean temperatures, and decreased salinity, a response to increasing atmospheric temperature), may in turn lead to a decrease in the global THC (a breakdown of this circulation is predicted by models when triple current CO_2 levels are attained [Bi *et al.*, 2001]), due to a stratification of the global ocean. The Mark 3 model output supports this theory, with the key THC currents (IT/SEC), indicating a significant decrease to transport values. Corresponding control run scenarios, also indicate decreases for these currents, however, at considerably lower scales (table 4.11). It is likely that this decrease to circulation is chiefly due to increased thermal stratification in the ocean basins, this effect reducing deep overturning circulation and reducing deep-water exchange in major global oceans (Bi *et al.*, 2001; Cai and Gordon, 1998, 1999; Matear and Hirst, 1999).

5.2.4 Geopotential Anomaly

Results indicate a slight increase in the alongshore gradient that is predicted to drive LC flow (Godfrey and Ridgeway, 1985; Thompson, 1984), from 0.04 m to 0.05 m, A2000 to A2100. This is likely attributable to increased temperature and decreased salinity water of the IT (and SEC), lifting the steric height, visualised in figures 4.28 and 4.29. Increased alongshore gradient suggests the geostrophic-driven LC (Godfrey, 1996) may then increase A2000 to A2100.

The corresponding control scenario indicates similar changes to the forced results, however, on a lesser scale. This would indicate that the increase presented in the forced scenario is attributable to the forcing, due to increased tropical (low density) inflows.

5.3 Changes to ocean circulation affecting current and heat-transport systems

5.3.1 Currents

The most prominent change is evident in the top 60 m of the profile. The most dominant change is the increase to IOCW, clearly illustrated in figures 4.30 and 4.31. This flow is likely responsible for the marked changes to salinity for the period A2070 to A2100, bringing increased salinity water from the central Indian Ocean. IOCW appears to become the dominant flow over regional oceanography, intensifying in both control and forced scenarios (represented by transport figures, table 4.11), considerably influencing the salinity signature over this region. The model also suggests increases to the equatorial SEC, attributed to increased windstress. Slight decreases are indicated for 15 - 20^oS, agreeing with reduced windstress. Lower transport values for the IT and SEC agree with this conclusion. A reduction in the westerly windstress associated with the Southern Ocean is also suggested, reflected in the surface (and upper-layer) currents 35 - 40^oS. Reduced surface windstress (indicated by values expressed in table 4.2), may lead to decreases to Ekman transport, these indicated most strongly by surface values, with corresponding changes to depth also presented.

It is likely that the major changes to currents are linked to external features that may not be resolved by the regional dataset. The IOCW flow is likely to be an attempt by the Indian Ocean basin to mass balance, with this system intrinsically linked to the flow

of the LUC (appearing to counter the IOCW at 128 - 406 m depth), with work by Seidov and Haupt indicating that this current may be sourced from deep oceanic (2 - 5 km) water from the western Indian Ocean basin, off Africa.

5.3.2 Transports

The most considerable transports for the region relate to the IT (and continued SEC) and the IOCW. Transports south of Cape Leeuwin also indicate fairly high transport, with the combination of the LC and the IOCW/WAC at $\sim 30^o S$ flowing south and around the southern Capes into the Great Australian Bight (as suggested in figure 2.1).

The model resolves for these currents qualitatively well, with slightly greater transports ($\sim$12.7 Sv) than observed records (5 - 18 Sv, with a mean flow regime of $\sim$10 Sv [Meyers, 1996]), however, better replication is achieved than comparison AOGCM's ($\sim$24 Sv indicated by the HadCM3 [Banks, 2000]).

Output suggests a decreasing trend for all currents, apart from the IOCW (table 4.11). Calculated transport values correspond with the reduction (or shutdown) of the global THC (Bi *et al.*, 2001; Cai and Gordon, 1998, 1999; Matear and Hirst, 1999), accounting for decreases to the IT, SEC and LCS transports, however do not resolve the suggested increase to the IOCW.

The source of increases to IOCW are not clear. The relationship between this flow and the LUC seem to be dependent, the LUC attempting to counter the incoming IOCW, balancing this flow at $\sim$160 m (the depth extent of the IOCW) and extending to $\sim$1500 m (this flow is centred at $18^o S$, $\sim$160 m, moving south, centred at $37^o S$, $\sim$1500 m). Thompson (1984) suggested the LUC is driven by an equatorward pressure gradient at depth, however, this is not resolved by the Levitus94 or A2000 dataset. Model output may indicate the source of this flow, from the deep ($>$ 1500 m) eastern Indian Ocean basin (Seidov and

Haupt, 1997), however, cannot be quantified in this regional dataset.

A2000 values most closely represent current climate. When comparison is made to C2000 values, it is clear forcing indicates a decrease to most transports are occurring. The magnified nature of this trend in the forced scenario (table 4.11), may suggest that this is attributable to increased CO_2.

Transport values for the LCS indicate greater variability, compared to the other transports. Suggested decreases are of the same magnitude in both the forced and control scenarios (for the 2000 to 2070 time period), indicating a low signal-to-noise ratio. The resolution (when related to the sub-grid scale LC) does not appear to completely resolve for this flow (LCS transport values disagreeing with observations), with no clear signal expressed in model output. Indirect features, such as decreased southerly windstress and increased alongshore steric height gradient, suggest that this flow may increase A2000 to A2100.

5.3.3 Heat Transport

Observed values of 1.34 PW are indicated by Macdonald (1998), relating to Indo-Pacific heat transport. The CSIRO Mark 2 model provides the best replication of this value from the 27 climate models reviewed in the IPCC TAR (Houghton *et al.*, 2001).

The Mark 3 model indicates values of 1.21 PW for the A2000 dataset, however, this value is obtained using a different method to Macdonald (1998), accounting for IT heat transport directly (7.5-13^oS, 122^oE). Macdonald (1998) reported that the heat transports due to the IT were 1.45 $\pm$ 0.30 PW at 18^oS and 1.30 $\pm$ 0.28 PW at 35^oS, based on model estimates. Values of Macdonald (1998) may incorporate a component of heat flux due to the IOCW (this indicates a considerable heat flux of 0.49 PW for 20 - 28.5^oS, 99.5^oE), overestimating the flux attributable solely to the IT.

Increased heat content for regional oceanography corresponds with an increase to the IOCW flow, possibly linked to increased heat flux associated with this increasing flow (a 9% increase in this flux occurs A2000 to A2100, table 4.11). It is unlikely that the IT (and associated heat flux) is responsible for this marked increase to heat content for the region, with only slight variation (less than 1%, table 4.11), and decreased heat flux associated with A2000 to A2100.

Banks and Wood (2002) indicate that THC and the IT need to be monitored over a long period of time (utilising continuous datasets) to indicate changes to climate, with snapshot datasets possibly clouded by variability. As a result, they suggest climate change signals will not be expressed by ocean heat transports. This agrees well with the results obtained in this study, with very small changes apparent in the calculation of heat transport from the Pacific through the IT.

The most marked result from this model output is the role of IOCW in the regional oceanography of Western Australia. This feature, while not acknowledged in prominent work of the region, relates well to magnified heat content of the region, heat flux values suggesting that this flow is a considerable source of heat for the region.

5.3.4 The Leeuwin Current

The LC is not completely resolved in transport calculations from model output, indicating a low signal-to-noise ratio. It is qualitatively represented in the top ~128 m of oceanography, extending from the North West Shelf, fed by IOCW/WAC at $\sim 30^o S$, then extending south to the Cape Leeuwin, accelerating around the southern Capes. This flow agrees well with the work of Church *et al.* (1989) and Smith *et al.* (1991), however current speeds are greatly underestimated due to 10-year mean datasets removing strong seasonal signals.

Dynamic changes occurring to regional oceanography indicate confused signals for the LC, with similar magnitude changes indicated in both the forced and control outputs. Current plots and corresponding transports associated with the LCS indicate a decreasing trend for the LC, with slight decreases to surface and source region currents, and corresponding alongshore transport (a 43% reduction is suggested by the model A2100 compared to A2000 (table 4.11 and figures 4.30, 4.31). The alongshore steric height gradient, hypothesised to drive the LC (Godfrey and Ridgeway, 1985; Thompson, 1984), indicates a slight increase. A decrease in southerly windstress, (opposing wind to the LC), may also indicate more suitable conditions for increased LC flows, a decreasing trend for windstress over the region, expressed in mean values (table 4.2).

No clear signal expressed in the current output for the Mark 3 model. Indirect features, such as decreased windstress and increased alongshore gradient, suggest that this flow may increase in intensity A2000 to A2100, attributable to increased CO_2 forcing.

5.3.5 IOCW

Predicted increase to the IOCW (expressed in current plots [figures 4.30 and 4.31] and transport calculations [table 4.11]), may in-turn lead to a stronger LC, this flow entraining the IOCW at the approximate latitude $\sim 30^o S$, leading to strengthened poleward flows south of this point. It is likely that the increase to flow would provide a low pressure zone for increased LC flow, drawing greater flow off the North West Shelf, south, forming the LC (combined flows extending eastwards into the Great Australian Bight). Lower density IT water (attributable to increased temperatures, and high-latitude freshening) effectively then has a greater steric height, leading to a strengthened gradient. Decreased density IT and SEC flows, suggested by the model may indicate that this gradient strengthens beyond the period covered within these datasets, attributable to increased forcing.

5.3.6 Inner-shelf Currents

Inner-shelf currents are sub-grid scale features, and are not resolved by the model. Changing patterns expressed for the oceanography and atmospheric circulation may be inferred, however, linking to these flows.

The equatorward inner-shelf currents discovered by Pearce and Pattiaratchi (1998) and Taylor and Pearce (1999), termed CC and NC respectively, are chiefly driven by seasonally strong southerly windstress of the summer months. Southerly windstress is predominant over the region, a consequence of the dominant subtropical high and subpolar low pressure systems (Hobbs *et al.*, 1998; Linacre and Hobbs, 1977). Suggested decreases to windstress by the forced scenario, coupled with a decreased LC, indicate confused responses for inner-shelf currents. The presence of the LC is acknowledged to suppress upwellings, driving cool inner-shelf currents. It is likely that due to the suggested decrease to the LC, more prominent inner-shelf flows would be expected.

5.4 Modelled change to oceanography - effects to climate for Western Australia

5.4.1 Climate

The role of the regional oceans in climate are acknowledged, with links between SST and rainfall clearly obvious in observations and modelled work. Modelled climate work has acknowledged the role of SST's in relation to the rainfall that is experienced around Australia, with accurate SST datasets, when used to begin a model run, providing much better climate replication, when compared to scattered or coarsely modelled SST data (Dr John McGregor *Pers. Comm.* CSIRO - DAR 25-10-02). Smith *et al.* (2000) have undertaken a study of the link between SWWA rainfall and Indian Ocean climate variability. They

concluded that there is a significant link between Indian Ocean SST and the rainfall that is experienced along both SWWA and a considerable portion of Australia. Rao *et al.* (2002) indicate that tropical Indian Ocean SST is linked to subsurface temperature features. It is likely that such features force SST, and consequently atmospheric patterns.

5.4.1.1 Atmospheric Circulation

The results presented in the chapter 4 indicate broadscale pressure features, and the associated gradient between these key features. Circulation features, apparent in the source regions for the key currents, are more influential than the broadscale patterns, linking closely with windstress and mesoscale features influencing ocean circulation. Mark 3 atmospheric resolution may not account for such features, with a coarse ∼200 km latitude by ∼200 km longitude grid (Gordon *et al.*, 2002).

A tendency for increased dominance of the subtropical high pressure cell is apparent in the forced output, the opposite tendency indicated by the control output (table 4.1. This is also expressed in the windstress plots (decreased values indicated for the forced scenario, increased for the control [table 4.2]).

While atmospheric circulation plays a large role in the global climate, these are key-linked to SST represented in the ocean basins. High SST leading to increased evaporation, associated with low pressure and cloud formation (expressed by the El Niño signal in the Western Pacific [Webster and Palmer, 1997]).

Work by Charles *et al.* (1999) and IOCI (2001) indicate changing circulation patterns, indicating weaker frontal systems hitting SWWA and therefore less rainfall. Simmonds and Keay (2000a, 2000b) support this conclusion with reanalysis of the NCEP-NCAR dataset, with Leighton *et al.* (1997) also indicating the number and intensity of synoptic depressions affecting SWWA have declined over the past 40 years (1958-1998). Mark 3 model output

tends to agree with this hypothesis, however, 10-year mean datasets do not resolve for seasonal patterns. The forced scenario indicates an increased pressure tendency, associated with a more dominant sub-tropical high pressure cell. A tendency for the greatest increased pressures in the most southern portion of the study region (41 - 44^oS, figures 4.3 and 4.4), may indicate a weakening (or decreasing dominance) of the strong frontal systems that are responsible for the largest proportion of SWWA rainfall during wet months (April to October). The general increasing trend occurring over the bulk of the study region (figure 4.4) indicates the increased dominance of the sub-tropical high pressure belt.

Extension of this analysis must be undertaken to determine whether the 10-yr mean data analysed during this study indicate a weakening of these systems over the entire annual cycle. The nature of analysis does not allow for this question to be answered, clearly further work needs to be done to look at suggested changes to seasonal patterns, indicated by the Mark 3 model.

5.4.1.2 Windstress

The model suggests a mean decrease to windstress over the forced scenario, with an increase indicated for the control scenario (table 4.2), corresponding with the increasing dominance of the subtropical high (decreasing for the control run). A close coupling between surface current flows and windstress is apparent from the change plots, A2000 to A2100 (figures 4.30 and 4.11 respectively). Increases of $\sim$10 cm s^{-1} are apparent in the equatorial-to-low latitudes (SEC), corresponding with a marginal increase (0.3 cm s^{-1}) to current flows. Entrainment of the IT flow, may counteract the slightly decreased transport values, the alongshore gradient setup by increased windstress linking the equatorial flows of the region. Marginally increased surface current values, replicating the IT, support this conclusion (10^oS, 116 - 122^oE - figure 4.30). Decreased low-latitude south easterly

tradewinds correspond with ∼0.2 cm s^{-1} increases to the IOCW, and decreased westerly windstress (corresponding with the roaring forties [35 - 43^oS]) indicates a decrease to ACC/WAC south of Cape Leeuwin.

Decreases to windstress across the Indian Ocean link to the Indian Ocean subtropical gyre. This anticyclonic circulation is driven by windstress (roaring forties) driving the ACC and supplementing the SEC (south easterly trades), providing a border to this flow in the south and north respectively. Decreases to this windstress (for A2100 - A2000, figure 4.11) suggest a decreased tendency for this gyral flow (indicated by decreased westerly flows, figure 4.30). The eastern boundary flow (WAC), is a counteracting feature to the poleward LC flow, decreases suggesting that the LC would continue to flow uninhibited (with possible increased intensity). Decreased windstress would also inhibit the development of inner-shelf (CC and NC) flows of the region.

5.4.1.3 Surface Fluxes

Change to surface fluxes of the ocean relate most closely with increased temperature suggested by model output. Increased heat flux into the ocean is suggested by model output, agreeing with predicted increases to global mean surface temperatures (Houghton *et al.*, 2001). The increase in oceanic heat content is chiefly resolved by increasing flux to the ocean (represented by marked increases to the maximum values presented in table 4.12), with a small component attributable to increased heat flux of the IOCW. Table 4.12 indicates that heat flux from the ocean halves (49% decrease) from A2000 to A2100, corresponding with an inferred decrease to the temperature gradient (between the ocean and the atmosphere [the atmosphere heating]). Concurrent increases to evaporation (expressed by decreasing freshwater flux values) are occurring with a 25% increase, A2000 to A2100. Increasing evaporation is another source of increased salinity for A2100, agreeing well with

the findings of Cai and Gordon (1998).

5.5 Model Agreement

Limited research has been undertaken on the ocean output of AOGCM's. Houghton *et al.* (2001) relate the output of 27 AOGCM's, reviewing key diagnostics of ocean circulation. A feature of this analysis, acknowledges the heat transport of the Indo-Pacific, attributable to flow of the IT. The CSIRO Mark 2 model has already been acknowledged as the best single-model replication for this region (section 2.6.2.1), and it is expected that the Mark 3 model would replicate this performance, being comprised chiefly of optimised Mark 2 code (Gordon *et al.*, 2001). Comparison can be made to Banks (2000), with the HADCM3 model, indicating a value of 24 Sv. The Mark 3 model resolves this flow at $\sim$12.7 Sv, with Meyers (1996) indicating mean values of $\sim$7 Sv (5 - 18 Sv range) are representative of this flow, the Mark 3 model fairing considerably better than its UK counterpart for this regional calculation.

5.5.1 Levitus Dataset

The Mark 3 model was initialised using the Levitus dataset, also providing restoration conditions prior to coupling (Gordon *et al.*, 2002). Considerably less observations for the Southern Hemisphere oceans have been taken, when comparison is made to the Northern Hemisphere (Levitus *et al.*, 1998). Extending this further, it is also clear that the Indian Ocean is the least sampled, compared to the Pacific and Atlantic Oceans (figure 5.1).

The accuracy of Levitus values for the Indian Ocean is questionable, these values obtained from mixed sources from 1941 to 1998, with considerable error related to data collected using XBT profilers (Levitus *et al.*, 1998). The mass-balance of the model disagrees quite markedly with the presentation of features such as the salinity signature of

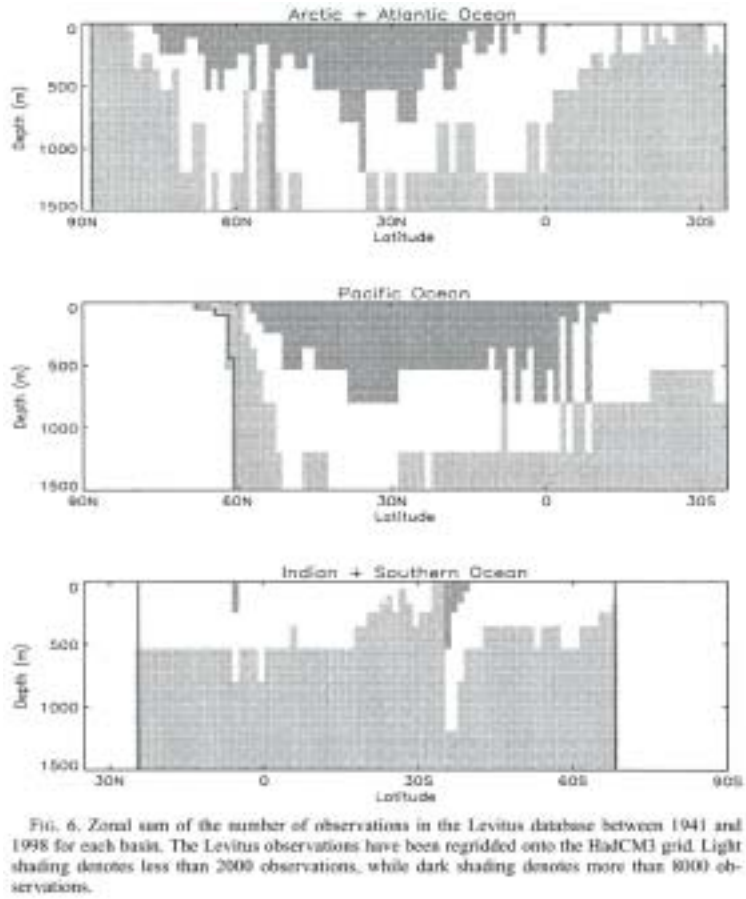

FIG. 6. Zonal sum of the number of observations in the Levitus database between 1941 and 1998 for each basin. The Levitus observations have been regridded onto the HadCM3 grid. Light shading denotes less than 2000 observations, while dark shading denotes more than 8000 observations.

Figure 5.1: Zonal sum of the number of observations in the Levitus Database 1941 - 1998 *(From Banks and Wood, 2002)*

IOCW, Levitus indicating far greater dominance (figures 3.10 to 3.13). Model replication may resolve for real oceanography better than the Levitus profiles, the T-S signature expressed in data collected off the coast of Perth, agreeing more closely with the Mark 3 output. Figure 3.10 more closely representing the work of Andrews (1977, 1983) and Church *et al.* (1989).

5.6 Synergy

Substantial changes are predicted for the regional oceanography of Western Australia, attributable to anthropogenic climate change. Key changes are linked to increased heat content of the ocean profile, due chiefly heat flux from the atmosphere, in accord with

predictions for increases to global mean surface temperature (Houghton *et al.*, 2001). A proportion of this increase may also be linked to the more dominant IOCW inflow, this current becoming more prominent A2000 to A2100.

Changing salinity patterns are also indicated, due to forcing, corresponding to changing T-S signatures of the key currents of the region. Changes such as melting of polar ice-caps, are suggested by increased surface mean temperatures, causing localised (polar) freshening, altering the density (mass) balance of the polar oceans. When coupled to increased temperatures of the upper ocean, these lead to decreased THC (Bi *et al.*, 2001; Cai and Gordon, 1998, 1999; Clark, 2002), directly affecting IT flow, and consequentially the regional oceanography of WA. A decreased trend to salinity is apparent in the A2070-A2000 calculations, with the higher salinity IOCW becoming dominant A2070 to A2100.

Changing density is acknowledged to be linked most directly to temperature of the regional ocean (Batteen and Huang, 1998). This is clear in calculations of density for the region, with saltier IOCW dominating the A2100 oceanography, however increased temperature linked to constant density values A2070 to A2100.

Predicted changes to global circulation patterns, suggest a strengthening of the subtropical high pressure cell, linked with a decreased rainfall signal over SWWA (Charles *et al.*, 1999). Increased heat content for the upper ($\sim$500 m) ocean profile and changes to salinity lead to a decrease to regional salinity, and a more stratified ocean, possibly linking to decreased THC in global oceans. Decreases to the IT and SEC are suggested by transport calculations, with possible increases to the LC due to decreased windstress and increased alongshore gradient. Decreased windstress suggests decreases in inner-shelf countercurrents to the LC.

CHAPTER 6
CONCLUSION

Oceanographic output from the CSIRO Mark 3 model suggests significant changes for regional oceanography over the next century. Increased heat content, linked to increased global mean atmospheric temperatures are the most prominent change predicted for the region.

Changing features are linked with increased CO_2 forcing modelled by the A2 scenario. Associated with increased temperatures, feedbacks including polar-ice melting (causing high-latitude freshening), atmospheric heating causing SST (and subsurface) increases, and surface fluxes link the ocean and atmosphere systems (Houghton *et al.*, 2001).

6.1 Research gaps

Analysis of the ocean component of an AOGCM alone does not allow for a conclusive resolution of change to the coupled climate system, however, may suggest key features linking to corresponding to atmospheric output.

10-year mean datasets, utilised in this study, have not allowed for analysis of seasonal patterns. The suggestion of a more dominant high pressure cell over SWWA needs to be resolved using seasonal data. The assumption that this system is strengthening over the entire period may actually be incorrect. A more pronounced summer dominance may be biasing output. The seasonal northward migration, presently experienced through winter, leads to increased rainfall associated with cold fronts interacting with SWWA. In order to further understand links between the ocean and the atmosphere, analysis of these seasonal patterns must be resolved.

The limited time period for this study has ensured that detailed analysis of each

of the current and current-paths has not been undertaken. The grid resolution of the model resolves for key currents (except for the LC) with transports associated to these flows qualitatively reasonable. An extension of this study to relate seasonal atmospheric circulation with oceanographic patterns, would hopefully uncover more fully the dynamics governing this coupled system, and may resolve for the seasonal LC signal.

Water masses that show the highest signal-to-noise ratios in the framework of Banks and Wood (2002) include; Arctic, North Atlantic, subpolar North Pacific, Arabian Sea, the Southern Ocean, and the Southern Boundary of the Indian Ocean. For subsurface temperature and salinity, there are large areas with significant signal-to-noise ratios after 30-years. Combining new observations with historical observations may lead to clear patterns of climate change evolving. Observations of the ocean circulation require much longer time periods to achieve similar detection indices (Banks and Woods, 2002).

The use of snapshots, as opposed to a continuous time series, do not account well for rapid changes to oceanography. The predicted sudden collapse of the THC, may be better analysed through continuous data sources, these allowing noise associated with the system to be separated from changes attributable to anthropogenic causes.

6.2 Future Studies

The scope for future research in this field is really endless. The work of Houghton *et al.* (2001) summarise current knowledge relating to climate change, with specific interest in atmospheric and terrestrial responses. Changes to oceanography have not been documented in detail.

There is an acknowledgement that more field-based global observation is required to fill knowledge gaps for the ocean. The international Global Ocean Observing System (GOOS - a component of UNESCO) is an international incentive attempting to fulfill

this requirement. The lack of extensive coverage of ocean observations in the Southern Hemisphere, and even less observations for the Indian Ocean (compared to Pacific and Atlantic coverage, figure 5.1), lead to widespread gaps in knowledge for this region, leading to an inability to answer questions relating to changing patterns of the region.

The development of higher resolution coupled AOGCM's is steering towards regional replication, supported by the very good qualitative replication of Western Australia regional oceanography by the Mark 3.

Banks and Wood (2002) indicate that the difficulty in determining long-term trends may be easier if the ocean is used as an indicator of climate change. The oceans absorb increased fluxes from the atmosphere, the upper ocean levels act to integrate these fluxes, producing less noise and a stronger signal to noise ratio, when compared to components such as high-variability surface fluxes. They indicate that temperature and salinity observations are more useful for the detection of climate change than other ocean climate indices.

The dominance of the IOCW feature has been highlighted by this study. Lack of knowledge relating to this flow, indicate that a large component of regional oceanography is presently unaccounted for. This flow is the chief cause of increased salinity for the region, with a significant heat transport contribution also suggested by the model. It is likely that continued dominance of this flow would lead to a dramatic change to the salinity signature expressed in the regional ocean. Such change may suggest that the T-S signature of WA regional oceanography is set to change. Increased salinities may lead to a decrease in the tropical life expressed in regional oceanography, with possible consequences for key fisheries of the region. These features linked to the tropical (low salinity) signature of the LC, the most southern extent of such features on any eastern (ocean) boundary globally.

A compartmental-study approach may be best method to develop a more wholesome

understanding of this system, resolving for individual currents and their regions separately, attempting to tease out interlinking relationships. This approach would link currents with their sources, categorising relationships with the atmosphere, allowing for resolution of local features driving these systems.

The need for a complete understanding of the systems governing the regional oceanography of Western Australia is the the underlier to effective resolution of the changing climate patterns and atmospheric phenomena. Such features cannot be explained simply by the analysis these above-ocean phenomena. It is likely, that the key linkages between the decreasing trend in SWWA rainfall since the 1970's is locked in the history of the Indian Ocean, and the forcing mechanisms driving this change. Such linkages have been uncovered by Rao *et al.* (2002), linking SST with subsurface temperature features in the tropical Indian Ocean.

APPENDIX A
ACRONYMS AND CONVENTIONS

The following list includes some key acronyms utilised in this study. Abbreviations where possible acknowledge published work, replicating these terms.

AABWF = Antarctic Bottom Water Formation (also AABW = Antarctic Bottom Water)
AC = Agulhas Current
ACC = Antarctic Circumpolar Current
ADCP = Acoustic Doppler Current Profiler
AGCM = Atmospheric Global Climate Model
AOGCM = Atmosphere-Ocean Global Climate Model
BT = Bathythermograph
CC = Capes Current
CSIRO = Commonwealth Scientific and Industrial Research Organisation
CTD = Conductivity Temperature Depth
CDIAC = Carbon Dioxide Information Analysis Centre
DAR = Division of Atmospheric Research (CSIRO)
DBAR = Decibar (unit of pressure measurement in oceanography)
EAC = East Australian Current
EACC = East African Coastal Current
EGC = Eastern Gyral Current (After Meyers, 1996)
EICC = East Indian Coastal Current
EMC = East Madagascar Current
ENSO = El Niño Southern Oscillation
GCM = Global Climate Model
GHG = Greenhouse Gas
GW = Great Whirl
IOCI = Indian Ocean Climate Initiative
IOCW = Indian Ocean Central Water (noted as the WAC)
IOD = Indian Ocean Dipole mode
IPCC = Intergovernmental Panel on Climate Change
IT = Indonesian Throughflow
JC = Java Current
LC = Leeuwin Current
LCS = Leeuwin Current Source region
LH/LL = Laccadive High/Low
LUC = Leeuwin Undercurrent
LUCIE = LeeUwin Current Interdisciplinary Experient
MAX = Maximum
MIN = Minimum
MJO = Madden-Julian Oscillation
MSLP = Mean Sea Level Pressure
NABWF = North Atlantic Bottom Water Formation (also NADW = North Atlantic Deep Water)
NADWF = North Atlantic Deep Water Formation
NC = Ningaloo Current
NEMC = North East Madagascar Current
NMC = Northeast Monsoon Current

OGCM = Ocean Global Climate Model
OLR = Outgoing Longwave Radiation
PW = Peta Watt (10^{15} Watts)
RHJ = Ras al Hadd Jet
SAR = Second Assessment Report (IPCC, 1996)
SC = Somali Current
SE = Standard Error (SD/$\sqrt{n}$ [Standard Deviation divided by the square root of n numbers in the sample])
SEC = South Equatorial Current
SECC = South Equatorial Countercurrent
SEMC = South East Madagascar Current
SG = Southern Gyre
SMC = Southwest Monsoon Current
SOI = Southern Oscillation Index (the index - Darwin to Tahiti MSLP)
SST = Sea Surface Temperature
STD = Salinity Temperature Depth
SWWA = Southwest Western Australia
T-S = Temperature-Salinity signature
TAR = Third Assessment Report (IPCC, 2001)
THC = Thermohaline Circulation
UNESCO = United Nations Educational, Scientific and Cultural Organisation
WA = Western Australia
WAC = West Australian Current (noted as the EGC [Eastern Gyral Current] by Meyers, 1996 and IOCW)
WICC = West Indian Coastal Current
XBT = Expendable Bathythermograph

The following units and numerical conventions are used in this study, these closely follow current oceanographic conventions.

Θ = **(Theta) Potential temperature**, due to the slightly compressible nature of seawater, a sample brought to the surface from depth will expand and therefore cool. The temperature of a sample brought to the surface adiabatically (without thermal contact with surrounding water) will therefore be warmer than *in situ*. The temperature that this parcel would have at the surface in these circumstances is called the potential temperature.

σ_Θ = **(Sigma Theta)**, is the potential density of seawater. The density of seawater at the surface (atmospheric pressure) usually varies between 1025 and 1028 (kg m^{-3}), and since the variability is so small, oceanographers typically subtract of 1000 to get a value between 25 and 28. This is typically referred to as σ_T, however use of potential temperature (Θ) indicates potential density (σ_Θ).

g = **Gravity** (9.8 m s^{-1})

Sv = **Sverdrup**, is a unit of measurement for volume flow (10^6 m^3 s^{-1})

ppt = **parts salt per thousand parts water**. The mean value for the oceans is about 34.7 with values in the Red Sea up to 40. Region of high freshwater input (rivers, estuaries) may have values close to pure water, 0.

hPa = **Hectopascal**, is a unit of pressure in the International System of Units (SI) annotation, equal to 102 Pa. It is equivalent to one millibar in the metric (CGS) system. Intense

sub-tropical high pressure cells may have summer pressures up to 1040 hPa, intense cyclones (or sub-polar low pressure systems) may have central pressures of 950 hPa or below.

dyne = **an acceleration of 1 cm s^{-2}** produced when a force of 1 dyne is exerted on a 1 gram mass.

APPENDIX B
CAPES CURRENT EXTENSION STUDY

These images (Figure B.1 and B.2) indicate the position of RV Franklin (1/96 and 4/96 respectively) transects analysed during the study of the Capes Current extension. The approximate locations of major towns and cities have been indicated on the maps.

These images were taken from the CSIRO - Franklin data website
(http://www.marine.csiro.au/franklin/ - accessed 15/12/2000).

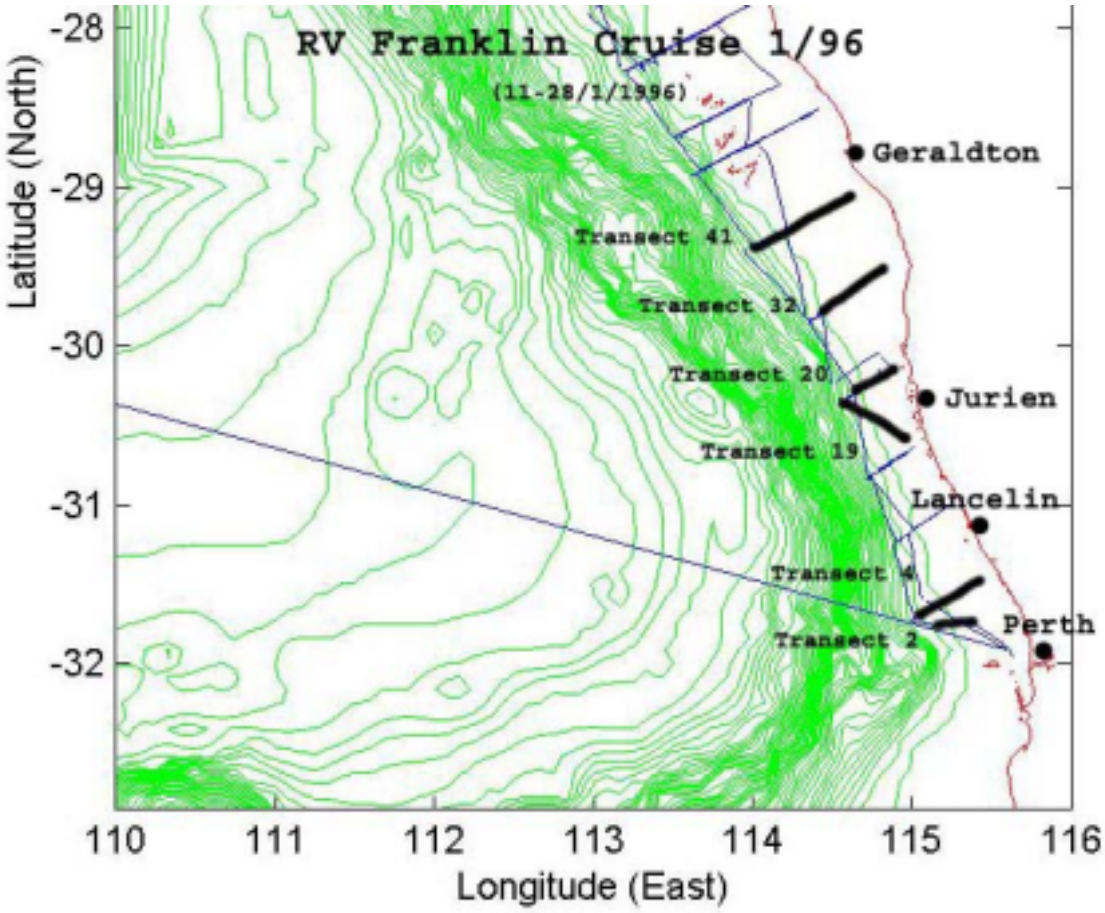

Figure B.1: Cruise track for RV Franklin 1/96 (11 - 28/12/1996)

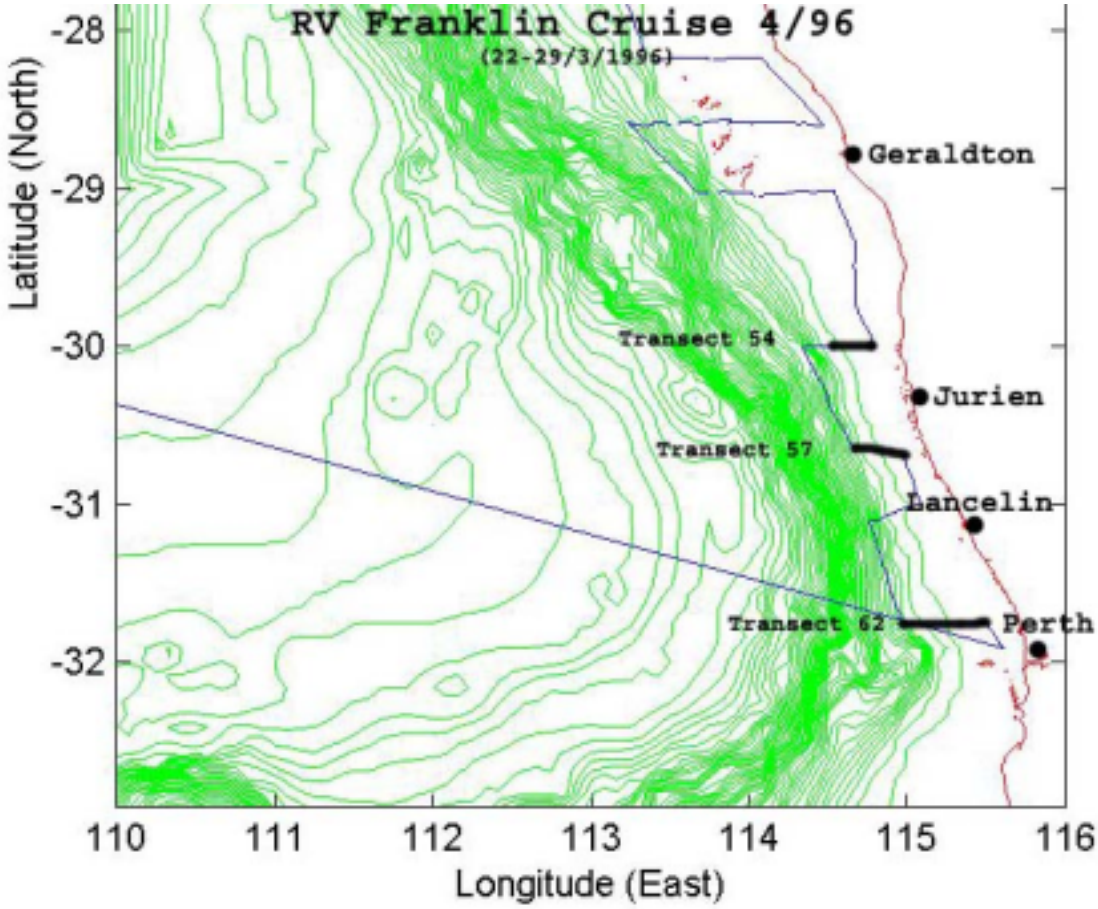

Figure B.2: Cruise track for RV Franklin 4/96 (22 - 29/3/1996)

REFERENCES

Allan, R., Chambers, D., Drosdowsky, W., Hendon, H., Latif, M., Nicholls, N., Smith, I., Stone, R. and Tourre, Y. (2001) Is there an Indian Ocean dipole, and is it independent of the El Niño - Southern Oscillation? *CLIVAR Exchanges*, **21**, September, 4 pp

Allan R.J. and Haylock, M.R. (1993) Circulation Features Associated with the Winter Rainfall Decrease in Southwestern Australia. *Journal of Climate*, **6**: 1356-1367

Allan, R., Lindesay, J. and Parker, D. (1996) *El Niño Southern Oscillation and Climate Variability.* CSIRO Publishing, PO Box 1139, Collingwood, Victoria 3066, 405 pp

Allan, R. and Hunt, B. (1999) *Climate modelling for the southern region of Western Australia.* CSIRO Division of Atmospheric Research, Aspendale, Victoria 3195.
Available: http://www.dar.csiro.au/publications/Allan_1999a.pdf Accessed 25-9-02

Anderson, D. (1999) Extremes in the Indian Ocean. *Nature*, **401**: 337-339

Andrews, J.C. (1977) Eddy structure and the West Australian Current. *Deep-Sea Research*, **24**: 1133-1148

Andrews, J.C. (1983) Ring structure in the poleward boundary current off Western Australia. *Australian Journal of Marine and Freshwater Research*, **34**: 547-561

Ansell, T.J., Reason, C.J.C., Smith, I.N. and Keay, K. (2000) Evidence for Decadal variability in Southern Australian Rainfall and relationships with regional pressure and sea surface temperature. *International Journal of Climatology*, **20**: 1113-1129

Arief, D. and Murray, S.P. (1996) Low-frequency fluctuations in the Indonesian throughflow through Lombok Strait. *Journal of Geophysical Research*, **101**: 12455-12464

Baquero-Bernal, A., Latif, M. and Legutke, S. (2002) On Dipolelike Variability of Sea Surface Temperature in the Tropical Indian Ocean. *Journal of Climate*, **15**: 1358-1368

Banks, H.T. (2000) Indonesian throughflow in a coupled climate model and the sensitivity of the heat budget and deep overturning. *Journal of Geophysical Research*, **105**: 26135-26150

Barnett, T.P., Hasselmann, K., Chelliah, M., Delworth, T., Hegerl, G., Jones, P., Rasmusson, E., Roeckner, E., Ropelewski, C., Santer, B. and Tett, S. (1999) Detection and Attribution of Recent Climate Change: A Status Report. *Bulletin of the American Meteorological Society*, **80**: 2631-2659

Barnett, T.P., Pierce, D.W. and Schnur, R. (2001) Detection of Anthropogenic Climate Change in the World's Oceans. *Science*, **292**: 270-274

Batteen, M.L. and Huang, M. (1998) Effect of salinity on density in the Leeuwin Current System. *Journal of Geophysical Research*, **103**: 24693-24721

Behera, S.K. and Yamagata, T. (2001) Subtropical SST dipole events in the southern Indian Ocean. *Geophysical Research Letters*, **28**: 327-330

Behera, S.K., Salvekar, P.S and Yamagata, T. (2000) Simulation of Interannual SST Variability in the Tropical Indian Ocean. *Journal of Climate*, **13**: 3487-3499

Benny, P.N. and Mizuno, K. (2000) Annual cycle of steric height in the Indian Ocean estimated from the thermal field. *Deep-sea Research I*, **47**: 1351-1368

Bernal, P.A. (1991) Consequences of Global Change for Oceans: A Review. *Climatic Change*, **18**: 339-359

Bi, D., Budd, W.F., Hirst, A.C. and Wu, X. (2001) Collapse and reorganisation of the Southern Ocean overturning under global warming in a coupled model. *Geophysical Research Letters*, **28**: 3927-3930

Blanke, B., Speich, S., Madec, G. and Doos, K. (2001) A Global Diagnostic of Interocean Mass Transfers. *Journal of Physical Oceanography*, **31**: 1623-1632

Broecker, W. (1991) The Great Ocean Conveyor *Oceanography*, **4**: 79-89

Bryden, H.L. (1973) New polynomials for thermal expansion, adiabatic temperature gradient and potential temperature of sea water. *Deep-Sea Research*, **20**: 401-408

Bureau of Meteorology (2002) *Southern Oscillation Index (SOI) Archives.*
Available: http://www.bom.gov.au/climate/current/soihtm1.shtml Accessed 17-10-02

Cai, W. and Gordon, H.B. (1998) Transient responses of the CSIRO climate model to two different rates of CO_2 increase. *Climate Dynamics*, **14**: 503-516

Cai, W. and Gordon, H.B. (1999) Southern High-latitude Ocean Climate Drift in a Coupled Model. *Journal of Climate*, **12**: 132-146

Carillo, C.N. (1892) Disertacion sobre las Corrientes Oceanicas y Estudios de la Corriente Peruana o de Humboldt. Microficha. *Boletn de la Sociedad geogrfica de Lima*, **2**: 52-110 (Lima, Per)

CDIAC (Carbon Dioxide Information Analysis center) (2002) *Current Greenhouse Gas Concentrations - Updated September 2002.*
Available: http://cdiac.esd.ornl.gov/pns/current_ghg.html Accessed 4-10-02

Charles, S.P., Bates, B.C., Whetton, P.H. and Hughes, J.P. (1999) Validation of downscaling models for changed climate conditions: case study of southwestern Australia. *Climate Research*, **12**: 1-14

Church, J.A., Cresswell, George R. and Godfrey, J. Stuart (1989) The Leeuwin Current. In: Neshyba, S.J., Mooers, CH.N.K., Smith, R.L. and Barber, R.T. (Eds) *Coastal and Estuarine Studies, Poleward Flows Along Eastern Ocean Boundaries.* Springer-Verlag, New York, Pp 374

Clark, P.U., Pisias, N.G., Stocker, T.F. and Weavers, A.J. (2002) The role of the thermohaline circulation in abrupt climate change. *Nature*, **415**: 863-869

Clarke, A.J. and Liu, X. (1994) Interannual Sea level in the Northern and Eastern Indian Ocean. *Journal of Physical Oceanography*, **24**: 1224-1235

Coatanoan, C., Metzl, N., Fieux, M. and Coste, B. (1999) Seasonal water mass distribution in the Indonesian throughflow entering the Indian Ocean. *Journal of Geophysical Research*, **104**: 20801-20826

Cresswell, G.R. (1996) The Leeuwin Current near Rottnest Island, Western Australia. *Marine and Freshwater Research*, **47**: 483-487

Cresswell, George R. and Golding, T.J. (1980) Observations of a south-flowing current in the south-eastern Indian Ocean. *Deep-sea Research*, **27A**: 449-466

Cresswell, G.R., Boland, J.L., Peterson, J.L. and Wells, G.S. (1989) Continental Shelf Currents near Abrolhos Islands, Western Australia. *Marine and Freshwater Research*, **40**: 113-128

Cresswell, G.R. and Peterson, J.L. (1993) The Leeuwin Current South of Western Australia. *Marine and Freshwater Research*, **44**: 285-303

Doos, Kristofer (1995) Interocean exchange of water masses. *Journal of Geophysical Research*, **100**: 13499-13514

Drosdowsky, W. (1993) Potential predictability of winter rainfall over southern and eastern Australia using Indian Ocean sea-surface temperature anomalies. *Australian Meteorological Magazine*, **42**: 1-6

Enting, I. G. (1999) *Calculating Future Atmospheric CO_2 Concentrations.* CSIRO Division of Atmospheric Research, Technical Paper **22**, 36 pp
Available: http://www.dar.csiro.au/publications/Enting_2000d.pdf Accessed 19-10-02

Frederiksen, C.S., Rowell, D.P., Balgovind, R.C. and Folland, C.K. (1999) Multidecadal Simulations of Australian Rainfall Variability: The Role of SST's. *Journal of Climate*, **12**: 357-379

Fieux, M., Molcard, R. and Ilahude, A.G. (1996) Geostrophic transport of the Pacific-Indian Oceans throughflow. *Journal of Geophysical Research*, **101**: 12421-12432

Fine, R.A. (1985) Direct evidence using tritium data for throughflow from the Pacific into the Indian Ocean. *Nature*, **315**: 478-480

Geerts, B. and Wheeler, M. (2001) *The Madden-Julian oscillation.*
Available: http://weather.uwyo.edu/~geerts/cwx/notes/chap12/mjo.html Accessed 25-9-2002

Gersbach, G.H. (2000) *Coastal upwelling off Western Australia.* Unpublished Ph.D. Thesis Available from: University of Western Australia, Department of Environmental Engineering, Crawley, Western Australia 6009

Gersbach, G.H., Pattiaratchi, C.B., Ivey, G.N. and Cresswell, G.R. (1999) Upwelling on the south-west coast of Australia source of the Capes Current? *Continental Shelf Research*, **19**: 363-400

Gentilli, J. (1952) *A Geography of Climate.* University of Western Australia, Crawley, Western Australia 6009, 107 pp

Gentilli, J. (1972a) *Australian Climate Patterns.* Thomas Nelson (Australia) Ltd, Collins Street, Melbourne, 285 pp

Gentilli, J. (1972b) Thermal anomalies in the Eastern Indian Ocean. *Nature Physical Science*, **238**: 93-95

Gentilli, J. (1991) Homologous peri-oceanic west coast climates in the Southern Hemisphere. *Journal of the Royal Society of Western Australia*, **74**: 15-33

Godfrey, J.S. (1996) The effect of the Indonesian throughflow on ocean circulation and heat exchange within the atmosphere: A review. *Journal of Geophysical Research*, **101**: 12217-12237

Godfrey, J.S. and Golding, T.J. (1981) The Sverdrup Relation in the Indian Ocean, and the Effect of Pacific-Indian Ocean Throughflow on Indian Ocean Circulation and on the East Australian Current. *Journal of Physical Oceanography*, **11**: 771-779

Godfrey, J.S. and Ridgway, K.R. (1985) The Large-Scale Environment of the Poleward-Flowing Leeuwin Current, Western Australia: Longshore Steric Height Gradients, Wind Stresses and Geostrophic Flow. *Journal of Physical Oceanography*, **15**: 481-495

Gordon, A.L. (1986) Interocean Exchange of Thermocline Water. *Journal of Geophysical Research*, **91**: 5037-5046

Gordon, A.L. and Fine, R.A. (1996) Pathways of water between the Pacific and Indian oceans in the Indonesian seas. *Nature*, **379**: 146-149

Gordon, H.B., Rotstayn, L.D., McGregor, J.L., Dix, M.R., Kowalczyk, E.A., O'Farrell, S.P., Waterman, L.J., Hirst, A.C., Watterson, I.G. and Elliot, T.I. (2002) *The CSIRO Atmospheric Research Mk 3.0 Climate Systems Model.* CSIRO - Division of Atmospheric Research, Technical Report No. **60**. Aspendale, Victoria 3195, 118 pp

Hamon, B.V. (1972) *Geopotential Topographies and Currents off Western Australia.* CSIRO Division of Fisheries and Oceanography, Technical Paper No. **32**, CSIRO Melbourne, 11 pp

Hamon, B.V. and Godfrey, J.S. (1978) The Physical basis of climate - The role of the oceans. In: Pittock, A.B., Frakes, L.A., Jenssen, D., Peterson, J.A. and Zillman, J.W. (Eds) *Climatic Change and Variability - A Southern Perspective.* Cambridge University Press, Cambridge CB2 1RP, England, 455 pp

Hirst, A.C. and Godfrey, J.S. (1993) The Role of Indonesian Through-flow in a Global Ocean GCM. *Journal of Physical Oceanography*, **23**: 1057-1086

Hisard, P. (1992) The centenary of the 1891 - El Niño report by Carranza (1892): First encounters of the 'ENSO phenomenon' by Krusenstern and by Humboldt. In: Ortlieb, L. and Machare, J. (Eds) *Paleo-ENSO records Intern. Symp.*, Extended Abstracts, ORSTOM (Lima)and CONCYTEC, Lima: 133-141

Hobbs, J. (1998) Present Climates of Australia and New Zealand. In: Hobbs, J.E., Lindesay, J.A. and Bridgman, H.A. (Eds) *Climates of the Southern Continents: Present, Past and Future.* John Wiley and Sons Ltd, West Sussex PO19 1UD, England, 297 pp

Hobbs, J., Lindesay, J. and Bridgman, H. (1998) Introduction: a Southern Hemisphere Overview. In: Hobbs, J.E., Lindesay, J.A. and Bridgman, H.A. (Eds) *Climates of the Southern Continents: Present, Past and Future.* John Wiley and Sons Ltd, West Sussex PO19 1UD, England, 297 pp

Holloway, P.E. (1995) Leeuwin Current observations on the Australian North West Shelf, May-June 1993. *Deep-Sea Research I*, **42**: 285-305

Houghton, J.T., Ding, Y., Griggs, D.J., Noguer, M., Van der Linden, P.J., Dai, X., Maskell, K. and Johnson, C.A. (2001) (Eds.) *Climate Change 2001: The Scientific Basis.* Cambridge University Press, UK, 881 pp

IOCI (2001) *Second Research Report - Towards Understanding Climate Variability in south western Australia - Research reports on the Second Research Phase of the Indian Ocean Climate Initiative.* Available from: Indian Ocean Climate Initiative Panel C/- Department of Environment, Water and Catchment Protection, Hyatt Centre, East Perth, Western Australia 6004 - October, 2001

IOCI (2002) *Climate variability and change in the south west Western Australia.* Available from: Indian Ocean Climate Initiative Panel. C/- Department of Environment, Water and Catchment Protection, Hyatt Centre, East Perth, Western Australia 6004, 34 pp

Kessler, W (2000) *Frequently (well, at least once)-asked-questions about El Niño.* Pacific Marine Environmental Laboratory/NOAA.
Available: http://www.pmel.noaa.gov/ kessler/occasionally-asked-questions.html Accessed 25-9-2002

Laughlin, G. (1997) *The User's Guide to the Australian Coast.* New Holland Publishers Pty Ltd, Frenchs Forest, NSW, Australia 2086, 213 pp

Leighton, R.M., Keay, K. and Simmonds, I. (1997) Variation in annual cyclonicity across the Australian region for the 29-year period 1965-1993 and relationships with annual Australian rainfall. In: Munro, R.K. and Leslie, L.M. (Eds.) *Climate Prediction for Agricultural and Resource Management.* Bureau of Resource Sciences, Australia 257-267

Levitus94 Annual (2002) *LEVITUS94: World Ocean Atlas 1994, an atlas of objectively analyzed fields of major ocean parameters.*
Available: http://ingrid.ldeo.columbia.edu/SOURCES/.LEVITUS94/ Accessed 25-9-2002

Levitus, S., Antonov, J.I., Wang, J., Delworth, T.L., Dixon, K.W. and Broccoli, A.J. (2001) Anthropogenic Warming of Earth's Climate System. *Science*, **292**: 267-270

Levitus, S., Boyer, T.P., Conkright, M.E., O'Brien, T., Antonov, J., Stephens, C., Stathoplos, L., Johnson, D. and Gelfeld, R. (1998) *NOAA Atlas NESDIS 18: World Ocean Database 1998, Volume 1: Introduction.* U.S. Department of Commerce, National Oceanic and Atmospheric Administration, Silver Spring, MD 20910-3282, USA, 346 pp

Linacre, E. and Hobbs, J. (1977) *The Australian Climatic Environment.* John Wiley and Sons, Milton, Queensland, Australia 4064, 354 pp

Lukas, R., Yamagata, T. and McCreary, J.P. (1996) Pacific low-latitude western boundary currents and the Indonesian throughflow. *Journal of Geophysical Research*, **101**: 12209-12216

Macdonald, A.M. (1998) The global ocean circulation: a hydrographic estimate and regional analysis. *Progress in Oceanography*, **41**: 281-382

Madden, R.A. and Julian, P.R. (1971) Detection of a 40-50 Day Oscillation in the Zonal Wind in

the Tropical Pacific. *Journal of the Atmospheric Sciences*, **28**: 702-708

Madden, R.A. and Julian, P.R. (1994) Observations of the 40-50-day Tropical Oscillation - A Review. *Monthly Weather Revue*, **122**: 814-837

Masselink, G. (1996) Sea breeze activity and its effect of coastal processes near Perth, Western Australia. *Journal of the Royal Society of Western Australia*, **79**: 199-205

Matear, R.J. and Hirst, A.C. (1999) Climate change feedback on the future oceanic CO_2 uptake. *Tellus*, **51B**: 722-733

McGuffie, K. and Henderson-Sellers, A. (1999) *A Climate Modelling Primer 2nd Edition.* John Wiley and Sons Ltd. West Sussex PO19 1UD, England, 253 pp

Meyers, G. (1996) Variation of Indonesian throughflow and the El Niño - Southern Oscillation. *Journal of Geophysical Research*, **101**: 12255-12263

Millero, F.J., Chen, C., Bradshaw, A. and Schleicher, K. (1980) A new high pressure equation of state for seawater. *Deep-Sea Research*, **27A**: 255-264

Morgan, Phil (2002) *CSIRO Seawater home page - A Library of MATLAB Computational Routines for the Properties of Seawater.*
Available: http://www.marine.csiro.au/∼morgan/seawater/ Accessed 8-10-02

Nicholls, N. (1989) Sea Surface Temperatures and Australian Winter Rainfall. *Journal of Climate*, **2**: 965-973

Nicholls, N., Chambers, L., Haylock, M., Frederiksen, C., Jones, D. and Drosdowsky, W. (1999) *Climate variability and predictability for south-west Western Australia.* Bureau of Meteorology Research Centre, Melbourne. Phase 1 report to the Indian Ocean Climate Initiative.
Available: http://www.ioci.commerce.wa.gov.au/ Accessed 6-3-02

Pacanowski, R.C. and Griffies, S.M. (2000) *MOM 3.0 Manual - Draft: March 23, 2000.* NOAA/Geophysical Fluid Dynamics Laboratory (GFDL), Princeton, USA 08542, 680 pp
Available: ftp://ftp.gfdl.gov/pub/GFDL_MOM3/manual_3.1.ps.Z Accessed 19-10-02

Pattiaratchi, C., Imberger, J., Zaker, N. and Svenson, T. (1995) *Perth Coastal Waters Study Physical Measurements.* Available from: The Centre for Water Research, University of Western Australia, Crawley, Western Australia 6009

Pawlowicz, R. (2002) *M_Map - A mapping package for Matlab.*
Available: http://www2.ocgy.ubc.ca/∼rich/map.html Accessed 8-10-02

Pearce, A. (1983) *A Bibliography of Physical Oceanography in Southwest Australian Waters.* CSIRO Marine Laboratories, Report **157**, Pp 36

Pearce, A.F. (1991) Eastern boundary currents of the southern hemisphere. *Journal of the Royal Society of Western Australia*, **74**: 35-45

Pearce, A.F. (1997) The Leeuwin Current and the Houtman Abrolhos Islands. In: Wells, F.E. (Ed.) *The Marine Flora and Fauna of the Houtman Abrolhos Islands, Western Australia.* Proceedings of the 7th International Marine Biology Workshop, Western Australian Museum. **1**: 11-46

Pearce, A. and Pattiaratchi, C. (1999) The Capes Current: a summer counter-current flowing past Cape Leeuwin and Cape Naturaliste, Western Australia. *Continental Shelf Research*, **19**: 401-420

Pernetta, J. (1995) *Philip's: Atlas of the Oceans.* Octopus Publishing Group Ltd, Docklands, London, E14 4JP, England, 208 pp

Peterson, R.G. and White, W.B. (1998) Slow oceanic teleconnections linking the Antarctic Circumpolar Wave with the tropical El Niño-Southern Oscillation. *Journal of Geophysical Research*, **103**: 24573-24583

Phillips, B.F., Pearce, A.F. and Litchfield, R.T. (1991) The Leeuwin Current and larval recruitment to the rock (spiny) lobster fishery off Western Australia. *Journal of the Royal Society of Western Australia*, **74**: 93-100

Pond, S. and Pickard, G.L. (1983) *Introductory Dynamical Oceanography - 2nd Edition.* Butterworth-Heinemann, Linacre House, Oxford OX2 8DP, England, 327 pp

Qui, B., Mao, M. and Kashino, Y. (1999) Intraseasonal Variability in the Indo-Pacific Throughflow and the Regions Surrounding the Indonesian Seas. *Journal of Physical Oceanography*, **29**: 1599-1618

Rao, S.A., Behera, S.K., Masumoto, Y. and Yamagata, T. (2002) Interannual subsurface variability in the tropical Indian Ocean with a special emphasis on the Indian Ocean Dipole. *Deep-Sea Research II*, **49**: 1549-1572

Rasmusson, E.M. and Carpenter, T.H. (1982) Variations in Tropical Sea Surface Temperature and Surface Wind Fields Associated with the Southern Oscillation/El Ni no. *Monthly Weather Review*, **110**: 354-384

Rochford, D.J. (1969) *Seasonal Interchange of High and Low Salinity Surface Waters off South-west Australia.* CSIRO Division of Fisheries and Oceanography, Technical Paper No. **29**, CSIRO Melbourne, 8 pp

Saji, N.H., Goswami, B.N., Vinayachandran, P.N. and Yamagata, T. (1999) A dipole mode in the tropical Indian Ocean. *Nature*, **401**: 360-363

Schiller, A., Godfrey, J.S., McIntosh, P.C., Meyers, G. and Wijffels, S.E. (1998) Seasonal Near-Surface Dynamics and Thermodynamics of the Indian Ocean and Indonesian Throughflow in a Global Ocean General Circulation Model. *Journal of Physical Oceanography*, **28**: 2288-2312

Schneider, N. (1998) The Indonesian Throughflow and the Global Climate System. *Journal of Climate*, **11**: 676-689

Schott, F., Fieux, M., Kindle, J., Swallow, J. and Zantopp, R. (1988) The Boundary Currents East and North of Madagascar 2. Direct Measurements and Model Comparisons. *Journal of Geophysical Research*, **93**: 4693-4974

Schott, F.A. and McCreary, J.P. Jr (2001) The monsoon circulation of the Indian Ocean. *Progress in Oceanography*, **51**: 1-123

Seidov, D. and Haupt, B.J. (1997) Global ocean thermohaline conveyor at present and in the late

Quaternary. *Geophysical Research Letters*, **24**: 2817-2820

Shenoi, S.S.C., Saji, P.K. and Almeida, A.M. (1999) Near-surface circulation and kinetic energy in the tropical Indian Ocean derived from Lagrangian drifters. *Journal of Marine Research*, **57**: 885-907

Simmonds, I. (1990) A modelling study of winter circulation and precipitation anomalies associated with Australian region ocean temperatures. *Australian Meteorological Magazine*, **38**: 151-161

Simmonds, I. and Keay, K. (2000a) Mean southern Hemisphere Extratropical Cyclone Behaviour in the 40-Year NCEP-NCAR Reanalysis. *Journal of Climate*, **13**: 873-885

Simmonds, I. and Keay, K. (2000b) Variability of Southern Hemisphere extratropical cyclone behaviour, 1958-1997. *Journal of Climate*, **13**: 550-561

Simmonds, I. and Rocha, A. (1991) The Association of Australian Winter Climate with Ocean Temperatures to the West. *Journal of Climate*, **4**: 1147-1161

Simmonds, I., Rocha, A. and Walland, D. (1992) Consequences of winter tropical pressure anomalies in the Australian region. *International Journal of Climatology*, **12**: 419-434

Sloyan, B.M. and Rintoul, S.R. (2001) The Southern Ocean Limb of the Global Deep Overturning Circulation. *Journal of Physical Oceanography*, **31**: 143-173

Smith, I. (1994) Indian Ocean Sea-surface Temperatures Patterns and Australian winter rainfall. *International Journal of Climatology*, **14**: 287-305

Smith, I.N., McIntosh, P., Ansell, T.J., Reason, C.J.C. and McInnes, K. (2000) Southwest Western Australian winter rainfall and its association with Indian Ocean climate variability. *International Journal of Climatology*, **20**: 1913-1930

Smith, R.L. (1989) Poleward Flows along Eastern Ocean Boundaries: An Introduction and Historical Review. In: Neshyba, S.J., Mooers, CH.N.K., Smith, R.L. and Barber, R.T. (Eds) *Coastal and Estuarine Studies Poleward Flows Along Eastern Ocean Boundaries.* Springer-Verlag, New York, 374 pp

Smith, R.L., Huyer, A., Godfrey, J.S. and Church, J.A. (1991) The Leeuwin Current off Western Australia, 1986-1987. *Journal of Physical Oceanography*, **21**: 323-345

Streton, N.A. (1981) Southern Hemisphere Sea Surface Temperature Variability and Apparent Associations with Australian Rainfall. *Journal of Geophysical Research*, **86**: 485-497

Suppiah, R., Collins, D. and Della-Marta, P. (2001) *Observed changes in Australian climate.* Climate Impact Group CSIRO Dept. of Atmospheric Research, Aspendale, Victoria, Australia 3195. Available: http://www.dar.csiro.au/publications/suppiah_2001a.pdf Accessed 25-9-02

Taylor, J.G. and Pearce, A.F. (1999) Ningaloo Reef currents: implications for coral spawn dispersal, zooplankton and whale shark abundance. *Journal of the Royal Society of Western Australia*, **82**: 57-65

Telcik, N. and Pattiaratchi, C. (2001) *The influence of northwest cloudbands on eastern Australian rainfall.* Unpublished report, Available from: The Centre for Water Research, University of

Western Australia, Nedlands, Australia, 63 pp

Thompson, R.O.R.Y. (1984) Observations of the Leeuwin Current off Western Australia. *Journal of Physical Oceanography*, **14**: 623-628

Thompson, R.O.R.Y. (1987) Continental-shelf-scale model of the Leeuwin Current. *Journal of Marine Research*, **45**: 813-827

Thompson, R.O.R.Y. and Veronis, G. (1983) Poleward Boundary Current off Western Australia. *Marine and Freshwater Research*, **34**: 173-185

Tomczak, Matthias (2000) *Utilities: Potential Temperature.*
Available: http://gaea.es.flinders.edu.au/ mattom/Utilities/pottemp.html Accessed 22-10-02

Tomczak, M. and Godfrey, J.S. (1994) *Regional Oceanography: an introduction.* Pergamon, Elsevier Science Ltd, Oxford OX3 0BW, England, 422 pp

Torrence, C. and Webster, P.J. (1999) Interdecadal Changes in the ENSO-Monsoon System. *Journal of Climate*, **12**: 2679-2690

Tourre, Y.M. and White, W.B. (1997) Evolution of the ENSO Signal over the Indo-Pacific Domain. *Journal of Physical Oceanography*, **27**: 683-696

Webster, P.J., Moore, A.M., Loschnigg, J.P. and Leben, R.R. (1999) Coupled ocean-atmosphere dynamics in the Indian Ocean during 1997-98. *Nature*, **401**: 356-360

Webster, P.J. and Palmer, T.N. (1997) The past and the future of El Niño. *Nature*, **390**: 562-564

Wigley, T.M.L. and Raper, S.C.B. (2002) Reasons for Larger Warming Projections in the IPCC Third Assessment Report. *Journal of Climate*, **15**: 2945-2952

White, W.B. (2000a) Influence of the Antarctic Circumpolar Wave on Australian Precipitation from 1958 to 1997. *Journal of Climate*, **13**: 2125-2141

White, W.B. (2000b) Coupled Rossby Waves in the Indian Ocean on Interannual Timescales. *Journal of Physical Oceanography*, **30**: 2972-2988

White, W.B. (2001) Evidence for Coupled Rossby Waves in the Annual Cycle of the Indo-Pacific Ocean. *Journal of Physical Oceanography*, **31**: 2944-2957

White, W.B. and Peterson, R.G. (1996) An Antarctic circumpolar wave is surface pressure, wind, temperature and sea-ice extent. *Nature*, **380**: 699-702

Wright, W.J. (1997) Tropical-Extratropical Cloudbands and Australian Rainfall: I. Climatology. *International Journal of Climatology*, **17**: 807-829

Xie, S., Annamalai, H., Schott, F.A. and McCreary, J.P. Jr (2002) Structure and Mechanisms of South Indian Ocean Climate Variability. *Journal of Climate*, **15**: 864-878

Yamagata, T., Behera, S.K., Rao, S.A., Guan, Z., Ashok, K. and Saji, H.N. (2002) The Indian Ocean Dipole: a Physical Entity. *CLIVAR Exchanges*, **24** June, 6 pp